

<b>REPORT DOCUMENTATION PAGE</b>			<i>Form Approved</i> <b>OMB No. 0704-0188</b>	
Public reporting burden for this collection of information is estimated to average 1 hour per response, including the time for reviewing instructions, searching existing data sources, gathering and maintaining the data needed, and completing and reviewing the collection of information. Send comments regarding this burden estimate or any other aspect of this collection of information, including suggestions for reducing this burden, to Washington Headquarters Services, Directorate for Information Operations and Reports, 1215 Jefferson Davis Highway, Suite 1204, Arlington, VA 22202-4302, and to the Office of Management and Budget, Paperwork Reduction Project (0704-0188), Washington, DC 20503.				
<b>1. AGENCY USE ONLY (Leave blank)</b>		<b>2. REPORT DATE</b> 22.May.03	<b>3. REPORT TYPE AND DATES COVERED</b> THESIS	
<b>4. TITLE AND SUBTITLE</b> A DIGITAL PARTICLE IMAGE VELOCIMETRY INVESTIGATION OF DELTA WING VORTEX FLOW AND VORTEX BREAKDOWN			<b>5. FUNDING NUMBERS</b>	
<b>6. AUTHOR(S)</b> 2D LT WIMER JEREMY D				
<b>7. PERFORMING ORGANIZATION NAME(S) AND ADDRESS(ES)</b> UNIVERSITY OF WASHINGTON			<b>8. PERFORMING ORGANIZATION REPORT NUMBER</b>  CI02-963	
<b>9. SPONSORING/MONITORING AGENCY NAME(S) AND ADDRESS(ES)</b> THE DEPARTMENT OF THE AIR FORCE AFIT/CIA, BLDG 125 2950 P STREET WPAFB OH 45433			<b>10. SPONSORING/MONITORING AGENCY REPORT NUMBER</b>	
<b>11. SUPPLEMENTARY NOTES</b>				
<b>12a. DISTRIBUTION AVAILABILITY STATEMENT</b> Unlimited distribution In Accordance With AFI 35-205/AFIT Sup 1			<b>12b. DISTRIBUTION CODE</b>	
<b>13. ABSTRACT (Maximum 200 words)</b>				
20030604 072				
<b>14. SUBJECT TERMS</b>			<b>15. NUMBER OF PAGES</b> 114	
			<b>16. PRICE CODE</b>	
<b>17. SECURITY CLASSIFICATION OF REPORT</b>	<b>18. SECURITY CLASSIFICATION OF THIS PAGE</b>	<b>19. SECURITY CLASSIFICATION OF ABSTRACT</b>	<b>20. LIMITATION OF ABSTRACT</b>	

University of Washington  
Graduate School

This is to certify that I have examined this copy of a master's thesis by

Jeremy D. Wimer

and have found that it is complete and satisfactory in all respects,  
and that any and all revisions required by the final  
examining committee have been made.

Committee Members:



Mitsuru Kurosaka



Dana Dabiri

Date: 3/10/03

## Master's Thesis

In presenting this thesis in partial fulfillment of the requirements for a Master's degree at the University of Washington, I agree that the Library shall make its copies freely available for inspection. I further agree that extensive copying of this thesis is allowable only for scholarly purposes, consistent with "fair use" as prescribed in the U.S. Copyright Law. Any other reproduction for any purposes or by any means shall not be allowed without my written permission.

Signature Jenny Wimer

Date 3/10/03

The views expressed in this article are those of the author and do not reflect the official policy or position of the United States Air Force, Department of Defense, or the U.S. Government



A Digital Particle Image Velocimetry Investigation  
of Delta Wing Vortex Flow and Vortex Breakdown

by

Jeremy David Wimer

A thesis submitted in partial fulfillment of the  
requirements for the degree of

Master of Science in Aeronautics and Astronautics

University of Washington

2003

Program Authorized to Offer Degree:

Department of Aeronautics and Astronautics

**DISTRIBUTION STATEMENT A**  
Approved for Public Release  
Distribution Unlimited

## TABLE OF CONTENTS

LIST OF FIGURES .....	iv
LIST OF TABLES .....	vii
1 Introduction.....	1
1.1 Fundamentals of Vortex Flows.....	1
1.2 Delta Wing Flow.....	4
1.2.1 Aspects of the Leading Edge Vortex .....	4
1.2.2 Vortex Breakdown over Delta Wings.....	5
1.3 Motivation and Method of Study.....	7
1.3.1 The Self-Induction Theory of Vortex Breakdown.....	7
1.3.2 Questions Under Consideration .....	8
1.3.3 Method of Study .....	9
2 Experimental Setup.....	10
2.1 Water Tunnel and Delta Wing Description .....	10
2.2 DPIV System Description.....	11
2.2.1 DPIV Theory.....	11
2.2.2 Laser and Optics .....	14
2.2.3 Digital Camera.....	14
2.2.4 Seeding Particles.....	15
2.2.5 Computer and Software .....	16
2.3 Specific DPIV Experimental Setup .....	16
2.3.1 Previous and Current PIV Measurement Planes.....	17
2.3.2 Detailed Physical Description of Experiments .....	18
2.3.3 Detailed Processing Parameter Description.....	25
2.3.4 Vector Post-processing and Circulation Calculation .....	27
3 Experimental Results.....	30
3.1 Vortex Core Plane Results.....	30
3.2 Cross-stream Plane Results.....	41
3.3 Cross-core Plane Results.....	44

3.3.1	Velocity and Vorticity Fields.....	46
3.3.2	Azimuthal Velocity Determination.....	52
3.3.3	Azimuthal Velocity Plots.....	53
3.3.4	Circulation Measurements in the Cross-core Plane .....	58
3.4	Dye Visualization Experimental Results .....	62
4	Numerical simulation results .....	66
4.1	Analysis of Simulation Used by Cain.....	66
4.1.1	Analysis of Simulation Input Parameters .....	66
4.1.2	Problems Arriving at a Steady Breakdown Location .....	69
4.2	From Transient to Steady State Breakdown .....	73
4.2.1	Convective Velocity Gradient.....	73
4.2.2	Filament Turn-off Case.....	79
4.3	Further Variations of the Vortex Filament Method .....	83
4.3.1	Core Interaction with Outer Region.....	83
4.3.2	Dual Apex Vortex Interaction.....	85
5	Discussion of DPIV and Simulation Results .....	91
5.1	A New Model of Delta Wing Leading Edge Vortices.....	91
5.1.1	Traditional Views.....	91
5.1.2	Deviations From and Additions to Traditional View .....	92
5.1.3	Suggestions for Modeling the LEV .....	98
5.2	Discussion of Simulation Results .....	99
5.2.1	Results from Simulation .....	99
5.2.2	Modified Self-Induction Theory.....	100
5.3	Vortex Breakdown Suppression and Control .....	101
5.3.1	Review of Some Breakdown Control Methods .....	101
5.3.2	Recommendation for Control in Light of Current Work .....	104
6	Conclusions and Recommendations .....	105
6.1	Conclusions.....	105
6.1.1	Vorticity Feeding into the Core .....	105

6.1.2	Vortex Breakdown Control.....	106
6.1.3	Vortex Filament Simulation Parameters.....	106
6.1.4	Simulation and Delta Wing Flow Comparison.....	106
6.2	Recommendations for Future Work.....	107
LIST OF REFERENCES.....		108
Appendix A – University of Washington Water Tunnel .....		111
A.1	Water Tunnel Description.....	111
A.2	Turbulence Level Determination .....	112

## LIST OF FIGURES

Figure 1-1: Ideal or Rankine vortex velocity and vorticity profiles ( <i>ref. 1</i> ) .....	2
Figure 1-2: Real vortex velocity and vorticity profiles ( <i>ref. 1</i> ).....	3
Figure 1-3: Schematic of shear layer roll-up on a delta wing ( <i>ref. 3</i> ).....	5
Figure 1-4: Smoke visualization of vortex breakdown on the F/A-18 at a 20, 25, and 30° angle of attack ( <i>ref. 7</i> ) .....	6
Figure 1-5: Example of delta wing vortex breakdown in a water tunnel.....	7
Figure 1-6: The self-induction theory of vortex breakdown from <i>ref. 2</i> .....	8
Figure 2-1: Drawing of large and small delta wings.....	10
Figure 2-2: Conceptual acquisition of image pairs for correlation ( <i>ref.9</i> ).....	12
Figure 2-3: Flow of statistical analysis of an image pair ( <i>ref. 9</i> ).....	13
Figure 2-4: PIV measurement planes used by Shih and Ding ( <i>ref. 15</i> ) .....	17
Figure 2-5: PIV measurement planes used in this study.....	18
Figure 2-6: Overview of experimental setup for capturing all three planes .....	20
Figure 2-7: Diagram of cylindrical lenses to control light sheet thickness.....	21
Figure 2-8: Grids showing distortion free images .....	22
Figure 2-9: Sample picture of laser firing and particle illumination .....	23
Figure 2-10: Sample raw images from each of the capture planes .....	24
Figure 2-11: Calculation of tangent and normal velocities to a line.....	28
Figure 2-12: Circulation calculation around a closed circular path.....	29
Figure 3-1: Axial velocity profile for various angles of attack ( <i>ref. 16</i> ).....	31
Figure 3-2: Velocity field for a 65° sweep delta wing at various angles of attack, $U_{\infty}=10\text{cm/s}$ , $c = 30\text{cm}$ , vortex core plane .....	32
Figure 3-3: Axial velocity in vortex core vs. angle of attack.....	33
Figure 3-4: Vortex core PIV results from Shih and Ding ( <i>ref. 15</i> ).....	34
Figure 3-5: Dye and DPIV vector field superposition, 65° sweep wing, 30° angle of attack, $U_{\infty} = 8.5\text{cm/s}$ , vortex core plane.....	36
Figure 3-6: Instantaneous velocity vectors and vorticity field for 65° sweep delta wing at a 30° angle of attack, $c = 30\text{cm}$ , $U_{\infty} = 8.5 \text{ cm/s}$ , vortex core plane.....	37

Figure 3-7: Two second average (30 image pairs) of vectors and vorticity field for 65° sweep wing at a 30° angle of attack, $c = 30\text{cm}$ , $U_\infty = 8.5\text{ cm/s}$ , vortex core plane...	39
Figure 3-8: Two second average (30 image pairs) of vectors and vorticity field for 65° sweep wing at a 30° angle of attack, $c = 30\text{cm}$ , $U_\infty = 21\text{ cm/s}$ , vortex core plane....	40
Figure 3-9: Close-up of vortex breakdown for 65° sweep wing at a 30° angle of attack, $U_\infty = 21\text{ cm/s}$ , vortex core plane .....	41
Figure 3-10: Sample axial vorticity results from Shih and Ding's study ( <i>ref. 15</i> ).....	42
Figure 3-11: Sample axial vorticity contours from Mitchell's study ( <i>ref. 19</i> ) .....	43
Figure 3-12: Composite velocity field for 30° angle of attack, cross-stream plane.....	44
Figure 3-13: Velocity vector field for 20° angle of attack, cross-core plane.....	47
Figure 3-14: Axial vorticity contours for 20° angle of attack, cross-core plane.....	49
Figure 3-15: Velocity field for 25° angle of attack, cross-core plane .....	51
Figure 3-16: Example of line used for azimuthal velocity calculation .....	52
Figure 3-17: Azimuthal velocity profile for 45cm chord wing.....	54
Figure 3-18: Azimuthal velocity plots for 30cm chord wing .....	57
Figure 3-19: LEV maximum circulation vs. chord location for various angles of attack	60
Figure 3-20: Circulation inside the LEV core.....	62
Figure 3-21: Dye visualization of 65° sweep delta wing at 15° angle of attack .....	63
Figure 3-22: Dye visualization of 65° sweep delta wing at 30° angle of attack .....	64
Figure 3-23: Dye visualization of breakdown in pipe flow ( <i>ref. 23</i> ) .....	65
Figure 4-1: Real and simulation input azimuthal velocity profile comparison .....	67
Figure 4-2: Circulation of vortex tube from the $z = 0$ plane vs. time .....	68
Figure 4-3: Streaklines resulting from experimental values being used as input parameters, $C = 20$ , $U_\infty = 8.5$ .....	69
Figure 4-4: Extended time evolution of vortex filaments from Cain.....	70
Figure 4-5: Assigned convective axial velocity profile for simulation in Figure 4-6.....	74
Figure 4-6: Simulation results with convective velocity gradient .....	74
Figure 4-7: Induced velocity profile for velocity gradient run .....	78

Figure 4-8: Simulation results from turn-off case.....	81
Figure 4-9: Filaments at $r = .12$ (red) and $r = .84$ (blue) .....	84
Figure 4-10: Setup of dual apex vortex interaction simulation.....	86
Figure 4-11: Results from dual apex vortex simulation.....	87
Figure 5-1: Feeding of circulation into the vortex core and outer region.....	93
Figure 5-2: Sketch of vortex sheet and secondary vortex cancellation .....	94
Figure 5-3: Numerical simulation of unsteady vortex structure and secondary vortex entrainment from <i>ref.28</i> . .....	95
Figure 5-4: Sketch of the development of the core and eventual vorticity cancellation by secondary vortex .....	96
Figure 5-5: Self-induction theory of vortex breakdown. Original (left) vs. Modified (right) .....	101
Figure A-1: Water Tunnel Layout .....	111
Figure A-2: Best fit line to determine $E_o$ .....	113
Figure A-3: Turbulence intensity measurements of UW water tunnel .....	114

## LIST OF TABLES

Table 3-1: Radius of maximum circulation ( $r_{\max}$ ) vs.  $x/c$  for all angle of attacks tested . 60



University of Washington

Abstract

A Digital Particle Image Velocimetry Investigation  
of Delta Wing Vortex Flow and Vortex Breakdown

by Jeremy D. Wimer

Chairperson of the Supervisory Committee

Professor Mitsuru Kurosaka  
Department of Aeronautics and Astronautics

The vortical flow over the suction side of a  $65^\circ$  sweep delta wing at high angles of attack is investigated in the University of Washington water tunnel using digital particle image velocimetry (DPIV). The method is first validated and then used to qualitatively and quantitatively describe the development of the leading edge vortex (LEV) both upstream and downstream of vortex breakdown. The circulation and azimuthal velocity profile in the vortex are measured and reveal that the maximum circulation of the LEV increases nearly linearly in the downstream direction up to the point of vortex breakdown. Circulation and velocity measurements in the solid-body rotational part of the LEV core, however, reveal that once the core is formed near the apex of the wing, the circulation there remains constant until just prior to breakdown, and no further vorticity is added to the core from the shear layer. The secondary vortex is found to be the key player in separating the primary vortex core from the shear layer. This model of the flowfield contradicts the generally accepted conical nature of delta wing flow. Current vortex breakdown suppression methods are analyzed in light of this new model. A numerical simulation based on the vortex filament method is also used to further the self-induction theory of vortex breakdown.

## **ACKNOWLEDGEMENTS**

I wish to express my deep gratitude to my advisor, Professor Mitsusu Kurosaka, for his guidance and inspiration in the development of this thesis. I would also like to thank Spot Srigrarom and C.B. Cain for their help in getting me up to speed on the topic of vortex breakdown, and their continued help along the way. I have also to thank Dennis Peterson, Robert Gordon, and Greg Lipski for their invaluable technical help and for fixing everything in the lab that I managed to break. I am deeply indebted to the Gordon C. Oates Memorial Endowed Fellowship for its financial support of my studies and this thesis. I would also like to thank the U.S. Air Force for allowing me to come to the University of Washington and giving me the opportunity to soon apply what I have learned here as a pilot. I am also very grateful for my loving wife who put up with me and helped me put everything in the right perspective. Most of all, I am thankful to God for giving me the skills and knowledge to pursue my dreams.

## **DISCLAIMER**

The views expressed in this thesis are those of the author and do not reflect the official policy or position of the United States Air Force, Department of Defense, or the US Government.

## 1 Introduction

Swirling fluid flow often called a vortex is both common and important in nature as well as man-made machines. Some common examples of a vortex include the airflow in a tornado or hurricane, or the swirling water pattern that develops as a bathtub is drained. It is the vortex's prevalence and potential benefit from its motion that make it the subject of much study and intrigue. The current study focuses on a specific type of vortex flow: the aerodynamic flow in the leading edge vortex (LEV) over a delta wing.

### 1.1 Fundamentals of Vortex Flows

In order to study vortex flows, it is first necessary to define some basic properties of a vortex and how they relate to the fluid dynamic equations of motion. The cylindrical coordinate system lends itself well to the study of vortices because the primary motion in a vortex is in the direction of one of the principal axes. The three principal axes point in the  $\hat{r}$ ,  $\hat{\theta}$ , and  $\hat{z}$  direction. The fluid velocity vector,  $\vec{u}$ , has components  $u_r$ ,  $u_\theta$ , and  $u_z$ , or the radial, azimuthal, and axial velocities respectively. An important property of rotating flow is its vorticity,  $\vec{\omega}$ . The vorticity is a measure of the fluid element's rotation about its own axis and differs slightly from the angular velocity of the fluid. The vorticity field is defined as the curl of the velocity field and has units of 1/time. Eqns. (1-1) through (1-4) define vorticity and its components in cylindrical coordinates.

$$\vec{\omega} \equiv \text{curl}(\vec{u}) \equiv \nabla \times \vec{u} \quad (1-1)$$

$$\omega_r = \frac{1}{r} \frac{\partial u_z}{\partial \theta} - \frac{\partial u_\theta}{\partial z} \quad (1-2)$$

$$\omega_\theta = \frac{\partial u_\theta}{\partial z} - \frac{\partial u_z}{\partial r} \quad (1-3)$$

$$\omega_z = \frac{1}{r} \frac{\partial(r u_\theta)}{\partial r} - \frac{1}{r} \frac{\partial u_r}{\partial \theta} \quad (1-4)$$

Since vorticity is simply the curl of the velocity, if the entire vorticity field is known, the velocity field everywhere can be found to within a constant of integration. If a fluid flow

has vorticity, it is said to be rotational. An irrotational flow is defined as having no vorticity. A typical vortex contains both regions of rotational flow and regions of irrotational flow. It is helpful to examine the azimuthal velocity profile of a vortex and define some common terms that arise. The profile for a Rankine vortex is shown in Figure 1-1. This is also called an ideal vortex as it has a core region ( $0 < r < r_c$ ) where the fluid rotates like a solid-body. The velocity in that region is  $u_\theta = \Omega r$  where  $\Omega$  is the traditional measure of angular velocity. At radii larger than  $r_c$ , the velocity varies inversely with the radius. This is referred to as the irrotational region. The transition from the rotational region to the irrotational one also takes place at the point of maximum azimuthal velocity. The vorticity profile is such that there is a finite amount of vorticity in the solid-body rotational core, and zero vorticity outside of the core. The vorticity in the core can be shown to be equal to  $2\Omega$  by Eqn. (1-4).

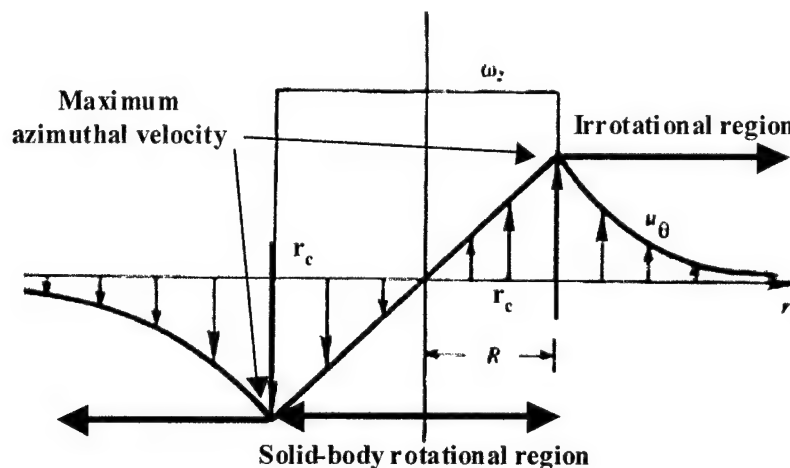


Figure 1-1: Ideal or Rankine vortex velocity and vorticity profiles (*ref. 1*)

Although it rarely occurs in natural flows, the Rankine vortex provides a good model for examining real vortices. A real vortex has a velocity and vorticity profile similar to that in Figure 1-2. There is still a radius,  $r_c$ , where the maximum azimuthal velocity occurs, however, the velocity profile inside the core is not quite like that of a solid-body, and the profile outside the core is not quite irrotational either. While the Rankine vortex model is not exactly like a real vortex, it is convenient to use the same terminology when speaking of a core region and outer irrotational region.

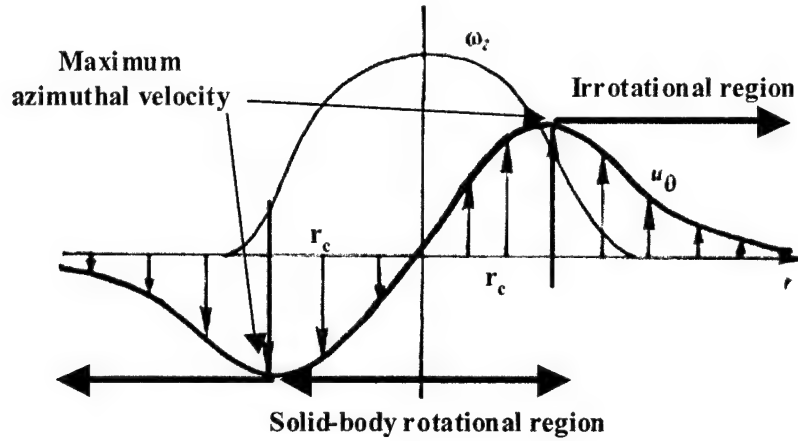


Figure 1-2: Real vortex velocity and vorticity profiles (*ref. 1*)

Another useful property of a vortex is its circulation,  $\Gamma$ , which is a measure of the strength of the vortex. It is defined as the line integral of velocity around a closed curve (Eqn. (1-5)). It can be related to the vorticity flux through a surface  $A$  using Stokes' theorem in Eqn. (1-6).

$$\Gamma = \oint_C \vec{u} \cdot d\vec{l} \quad (1-5)$$

$$\Gamma = \int_A \text{curl}(\vec{u}) \cdot d\vec{A} = \int_A \vec{\omega} \cdot d\vec{A} \quad (1-6)$$

With these definitions it becomes clear that the circulation taken about a circle of radius  $r$  in the solid-body rotational region of the Rankine vortex is

$$\Gamma = \int_0^{2\pi} u_\theta r d\theta = 2\pi r u_\theta = 2\pi r^2 \Omega \quad \text{while the circulation taken about a circle with radius}$$

larger than  $r_c$  will still be  $2\pi r_c^2 \Omega$  because no circulation is added to the vortex in the irrotational region. The same does not quite hold true for real vortices because the azimuthal velocity does not fall off exactly as  $1/r$ .

As was mentioned before, if the vorticity is known, the velocity field can also be determined. The equation governing this relationship is the Biot-Savart law. It relates the vorticity at point  $(x', y', z')$  to the velocity at a different point,  $(x, y, z)$ . The Biot-Savart law for incompressible flow is developed from the momentum and continuity equations in detail in *ref. 2* and is simply stated here in Eqn. (1-7).

$$\vec{u}(x, y, z) = \frac{1}{4\pi} \iiint \frac{(\omega(x', y', z') \times \vec{R})}{\|\vec{R}\|^3} dV' \quad (1-7)$$

Here  $\vec{R}$  is the position vector from  $(x', y', z')$  to  $(x, y, z)$ . This relationship is useful in numerical simulations of vortex flow as it describes the velocity that is induced at every point in a flow from the vorticity that exists at every point around it.

## 1.2 Delta Wing Flow

Vortex flows are prevalent on the suction side of a delta wing operating at a high angle of attack. The delta wing shape is important in the field of aeronautics as it is found on many past and present fighter aircraft as well as some designs for unmanned aerial vehicles (UAVs). The benefits of the delta wing shape are numerous. High leading edge sweep angles have the benefit of reducing the Mach number of the flow relative to the wing leading edge serving to lessen or delay the supersonic effects such as wave drag (*ref. 3*). Also, in the high angle of attack flight envelope, the vortices formed by the separated flow over these wings will still contain high axial and azimuthal velocities resulting in a low pressure region and generation of lift where a traditional unswept wing would stall. As a result, the lift curve for a delta wing is lower than that of an unswept airfoil in the low angle of attack region, yet it continues to increase well into the high angle of attack region beyond the point where an unswept wing would stall.

### 1.2.1 Aspects of the Leading Edge Vortex

The LEV flow over the suction surface of a sharp edged delta wing operating at a high angle of attack is inherently complex, unsteady, and three-dimensional. Studies dating back to the 1950s and too numerous to list have been accomplished to shed light on the flow pattern over a delta wing in general. It is safe to say that no single equation or model yet exists which can accurately predict the flow over a given delta wing, leading one to believe that the only thing simple about a delta wing is its shape. The basic pattern of the flow, however, is well known. The LEV forms when the flow over the sharp leading edge separates from the wing surface and forms a free shear layer. This shear

layer rolls up into a vortex structure and more fluid is fed into the vortex over the length of the leading edge. A traditional conceptual representation of this flow is found in *ref. 3* and shown in Figure 1-3. The shear layer forms a vortex sheet that feeds into the primary vortex which in turn induces a secondary vortex outboard of the primary one.

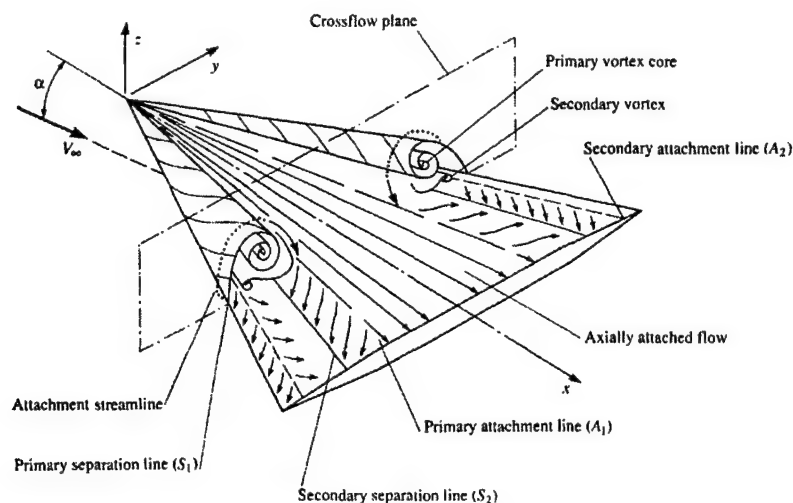


Figure 1-3: Schematic of shear layer roll-up on a delta wing (*ref. 3*)

High axial velocities of 2-3 times the freestream value are typically found near the apex of the wing, which then decrease in the downstream direction. This is indicative of an adverse axial pressure gradient, much like that of a conventional two-dimensional airfoil operating at a high angle of attack.

### 1.2.2 Vortex Breakdown over Delta Wings

As the angle of attack of a delta wing is increased beyond a certain threshold, which is highly dependent on wing sweep, the LEV becomes unstable for the length of the wing and vortex breakdown will exist at a certain chord location. The phenomenon of vortex breakdown is another widely studied yet elusive topic. Many researchers still readily admit that a comprehensive theory to predict vortex breakdown and an exact understanding of the observed flow does not exist (*refs. 4, 5, and 6*). The point of breakdown has generally been defined as a stagnation point along the vortex axis followed by a region of reversed flow. Two types of breakdown are generally

considered: the nearly axisymmetric bubble type and the asymmetrical spiral type. Breakdown has also been commonly found and studied in swirling pipe flows.

The study of vortex breakdown is of great importance because of its detrimental effects on the lift produced by a delta wing and the possibility of interactions between the extremely unsteady breakdown wake and other control surfaces of the aircraft such as the vertical tails. One aircraft where this has been found to be a profound problem is the F/A-18. A high G turn or pitch up maneuver in which the aircraft operates at a sustained high angle of attack has been found to produce vortex breakdown of the LEV emanating from the highly swept leading edge extension. The unsteady oscillations in the flow have been found to impinge on the twin vertical tails and cause problems with high-cycle fatigue and ultimately lead to failure. Figure 1-4 shows smoke introduced into the LEV of an F/A-18 operating at a 20, 25, and 30° angle of attack respectively. As angle of attack is increased, breakdown moves towards the leading edge due to the increased strength of the LEV. It is obvious from this figure that the vertical tail lies directly in the path of the breakdown wake.



Figure 1-4: Smoke visualization of vortex breakdown on the F/A-18 at a 20, 25, and 30° angle of attack (*ref. 7*)

The same phenomenon of vortex breakdown can be investigated in slow water tunnel flows. Erickson (*ref. 8*) has investigated the correlation between high speed vortex flow in air and water tunnel vortex flows. His findings indicated a good qualitative correlation between the two due to the similarities in flow separation points and behavior, and little variance in the structure of breakdown with Reynolds number. This being the case, a water tunnel provides an excellent tool to investigate the LEVs and vortex breakdown in general. Figure 1-5 shows an example of breakdown on a delta wing



illustrated by food coloring dye in a water tunnel. Both the bubble (top) and spiral (bottom) forms of breakdown are evident in the figure.

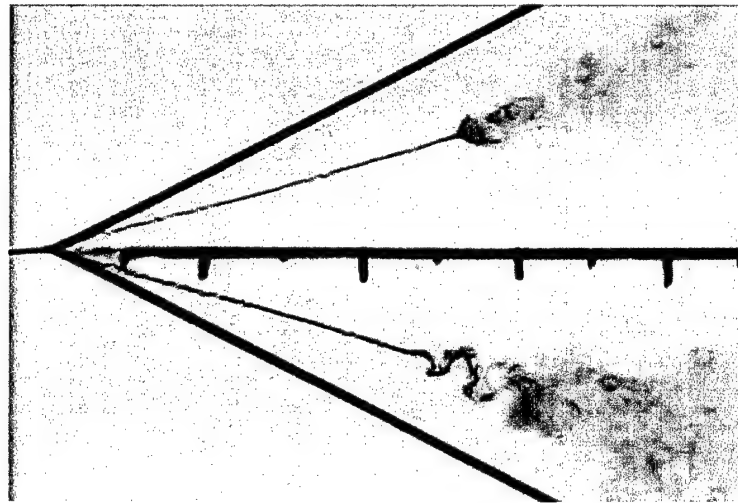


Figure 1-5: Example of delta wing vortex breakdown in a water tunnel

The ability to control the LEV and the breakdown location associated with it is a topic of great importance. The focus of current research is to delay breakdown until further aft portions of the wing, or suppress it altogether. The ability to control breakdown could lead to methods of controlling and maneuvering aircraft without the use of conventional control surfaces.

### ***1.3 Motivation and Method of Study***

#### ***1.3.1 The Self-Induction Theory of Vortex Breakdown***

One of the goals of this study is the furtherance or modification of the self-induction theory of vortex breakdown presented in a numerical simulation done by Cain. The details of Cain's simulation using the vortex filament method are contained in *ref. 2*, and it is highly recommended that the reader be somewhat familiar with it before proceeding with the simulation results portion of this study (section 4). Cain showed that through simple Biot-Savart law self-induction, a vortex tube can undergo breakdown if a pre-existing axial vorticity gradient is in place. This vorticity gradient is a key component of breakdown. It was found that the this gradient alone could induce vortex filament pile-up, radial expansion of the filaments, an azimuthal vorticity sign switch,

and a turning point with a region of reversed flow. All of these components are readily observable in breakdown experiments in pipes as well as over delta wings.

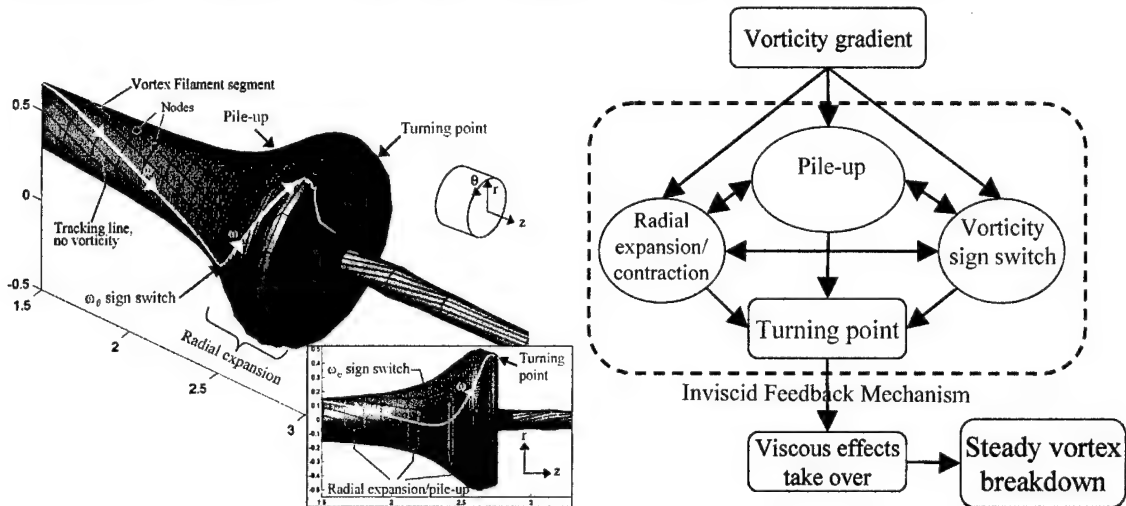


Figure 1-6: The self-induction theory of vortex breakdown from ref. 2

Cain's simulation shows the transient formation of breakdown, meaning it does not reach a steady state or stable solution. This is unsatisfactory in that breakdown does reach a stable position if upstream conditions are held constant. A major thrust of this part of the current study was then to modify the simulation in order to reach some constant and sustainable position, and ultimately expand the self-induction theory from the transient formation of breakdown to the steady state position.

### 1.3.2 Questions Under Consideration

Several gaps remain in the understanding of delta wing flows and vortex breakdown. The purpose of this study is then to fill in some of these gaps by using both an experimental and numerical approach. The questions under consideration in this study are as follows:

1. How is vorticity fed into the solid-body core of the LEV by the shear layer as the vortex travels downstream?
2. How can vortex breakdown be controlled?
3. Are the parameters used in the current vortex filament method similar to a realistic flow situation where vortex breakdown occurs?

4. How relative is this simulation to real LEV flow, and how should the vortex be modeled?

The answers to these questions will lead to a greater understanding of vortex flow over delta wings in general, and provide insight into the methods of modeling these flows in the future.

### *1.3.3 Method of Study*

In seeking answers to the above questions, the method of digital particle image velocimetry will be employed in order to experimentally obtain full field velocity and vorticity measurements of two-dimensional slices of the delta wing flow. The results of this will be compared with the traditional view of a conical vortex flow field, and show where this view may be flawed. A numerical simulation will also be used in an attempt to achieve a steady state breakdown solution, and infer more about the formative mechanisms of vortex breakdown.

## 2 Experimental Setup

### 2.1 Water Tunnel and Delta Wing Description

A horizontal recirculating water tunnel with a 3.0m x 0.7m x 0.7m glass test section located at the University of Washington Fluid Dynamics Laboratory was used for the experiments in this thesis. The tunnel is capable of speeds from 0 to 50cm/s with a freestream turbulence level of less than 1% for speeds above 5cm/s. A full description with freestream turbulence data is included in Appendix A.

Two clear plexiglass delta wings were the main objects used in this study. Each had a leading edge sweep of  $65^\circ$  and a  $30^\circ$  edge bevel angle. The larger wing had a centerline chord length of 45cm and thickness of 0.9cm while the smaller wing had a 30cm chord and was 0.5cm thick. Drawings of the two wings are shown in Figure 2-1.

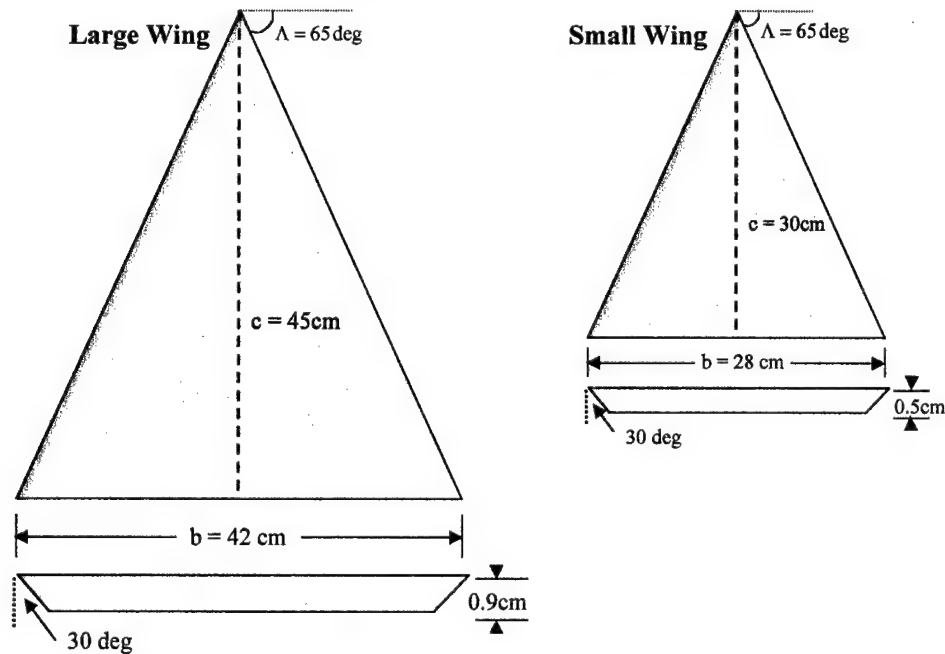


Figure 2-1: Drawing of large and small delta wings

Dye visualization was accomplished with a gravity feed system through small diameter surgical tubing and metal injection tips. The gravity feed system was found to produce much steadier streaklines than the existing electric pump setup. Steady streaklines were best seen when the dye flow velocity was matched with the local water

flow velocity. This was accomplished by simply raising or lowering the dye reservoir to change the pressure head at the dye injection tip.

## 2.2 *DPIV System Description*

The Digital Particle Image Velocimetry (DPIV) system used in this study was installed in the UW Fluid Dynamics Laboratory in June of 2002. A brief overview of PIV theory is presented followed by a detailed description of the experimental setup.

### 2.2.1 *DPIV Theory*

The book *Particle Image Velocimetry-A Practical Guide* by Raffel et al. provides an excellent overview of the PIV method and considerations for setting up any PIV experiment, and most of the background given here is directly from that source (*ref. 9*). The basic premise behind PIV is that small particles located in the flow, which move with the local fluid velocity, can be captured at two successive times. The two images can then be evaluated by observation or statistical methods to obtain a displacement or shift of the particles in the image pair. Knowing the time lapse between the two images then allows for calculation of a velocity vector. Major advantages of the PIV method over other flow measurement techniques include it being a whole field and non-intrusive method. That is, information about a large area of the flow field can be obtained instantaneously, and unlike a hotwire or pitot probe, the observation method used does not disrupt the flow in any way other than the small particles which are located in the flow itself. Applications of the PIV technique are broad and range from microscopic cellular movement to slow water tunnel flows to high-speed compressible flow fields and shock waves. Considerable variation of the experimental setup is required in each of these cases, but the principle is the same.

Any PIV experiment will contain several key components. One is a light source which is generally a controllable laser necessary to illuminate a plane of the seeded flow. The laser output is sent through an arrangement of optics to form a light sheet at the desired plane of interest. The imaging camera is synchronized with the laser pulses so that successive images can be acquired. These are both usually controlled with a central

computer which can also be used for statistical processing of the images to produce the velocity and vorticity fields.

Modern hardware and computational power has allowed the acquisition, storage, and analysis of the particle images to be digitized allowing for rapid data reduction and results. A common way to acquire the images is through single exposure / double frame PIV which was used in this study. The common statistical method used to measure the particle shift in the two images is a cross-correlation. The two digital images referred to as an image pair each have a grey level intensity which is a function of the position,  $I(x,y)$ . Figure 2-2 shows an image pair and an interrogation window which is a small subset of each image.

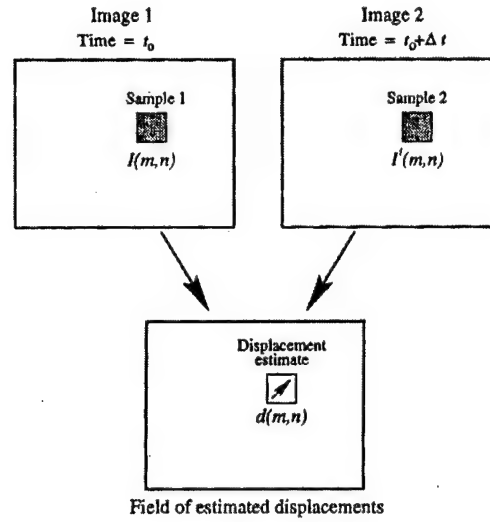


Figure 2-2: Conceptual acquisition of image pairs for correlation (*ref.9*)

This window is chosen to be small enough so that the effects of velocity gradients and accelerations inside the window can be minimized since it is impossible to obtain a curved path or acceleration data from one interrogation window. The two windows are then correlated to yield a displacement field  $d(m,n)$ . The discrete cross-correlation function is defined as

$$R_{II'}(x,y) = \sum_{i=-K}^K \sum_{j=-L}^L I(i,j) I'(i+x, j+y). \quad (2-1)$$

Essentially this means that when sample  $I$  is shifted around inside of a larger subset,  $I'$ , the sample shift  $(x,y)$  where the samples' particles align the best with each other will have

the highest cross-correlation value. This shift value is then the particle displacement between the two images. This method is very intuitive, however there is a quadratic increase in the required number of multiplications with sample size, requiring excessive computational time. This calls for a more efficient way of computing the correlation function. This is accomplished through the use of fast Fourier transforms (FFT), which can be rapidly processed on a computer by widely available routines. Taking advantage of the correlation theorem relating correlation in the real domain to multiplication in the frequency domain, the cross-correlation of two functions becomes equivalent to complex conjugate multiplication of their Fourier transforms, or

$$R_{II} \Leftrightarrow \hat{I} \cdot \hat{I}^* \quad (2-2)$$

where the  $\hat{\phantom{x}}$  denotes the Fourier transform and the  $*$  is the complex conjugate. With this the correlation between the samples can be found by calculating the FFT of two equally sized interrogation windows. This greatly speeds up the process, reducing the number of computations from  $O[N^2]$  to  $O[N \log_2 N]$ . The inverse Fourier transform will then reveal the particle shift in the real domain. This process is summarized in Figure 2-3.

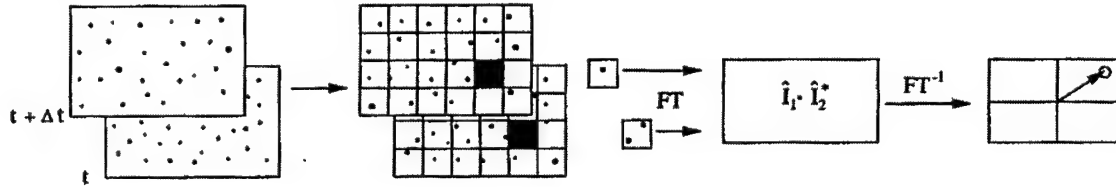


Figure 2-3: Flow of statistical analysis of an image pair (*ref. 9*)

While the peak of the correlation function will occur at one pixel location, the particle displacement can be determined to fractions of a pixel by considering the heights of the peaks surrounding the highest peak. This is called sub-pixel accuracy which improves upon the accuracy of the displacement measurement, and is described in chapter 5 of Raffel (*ref. 9*).

After the displacement field for the entire image has been computed, the velocity field in the pixel domain is then calculated by simply dividing by  $\Delta t$  for the two images. Then, further processing of the data can be done including outlier removal, smoothing,

converting to the real domain from the pixel domain, and the calculation of the vorticity field or streamlines from the velocity field.

DPIV has proven to be an accurate and convenient way to obtain full-field instantaneous fluid velocity measurements. For this reason it is well suited to measure the instantaneous velocities in the non-steady flow over delta wings, and in the vortex breakdown region in particular. A further description of the specific DPIV hardware used in this study follows.

### 2.2.2 *Laser and Optics*

A dual-headed Solo PIV (model: Solo 120) Neodym-yttrium-aluminum-garnet (Nd:YAG) laser manufactured by New Wave Research was used to illuminate the plane of interest. The laser operated at a wavelength of 532nm using 115V, 10amp power input for a maximum energy output of 120mJ. The laser was secured to a breadboard and table behind the tunnel test section. A dual-headed laser was needed because the required  $\Delta t$  between pulses was smaller than the shortest pulse rate for one laser head. The outputs from the two lasers were combined into one beam using beam-combining optics provided by New Wave. The laser beam immediately passed through a concave cylindrical spreading lens (CVI model RCC-25-15-10.2-C-532) and then a convex cylindrical lens (CVI model RCX-40.0-30.0-50.9-C-532) spaced so that the width of the laser beam could be controlled in the plane of interest. A series of Nd:YAG coated mirrors (CVI model Y2-2037-45-S) directed the beam underneath the test section and then up and through a final cylindrical lens (CVI model RCC-40-30-30.5-C-532) which spread it out into the plane of interest inside the test section. Specific dimensions for optimizing the setup are included below.

### 2.2.3 *Digital Camera*

A charge-coupled device (CCD) camera manufactured by Uniq and with progressive scanning was used. The camera could capture a 1024x1024 pixel area, and record those images to a hard disk in real time. A C-mount was used to couple the camera with an Olympus 85mm manual focusing lens with an adjustable aperture so that



the brightness of the picture could be controlled. The gain of the camera signal could also be controlled to adjust the brightness of the image, with care not to clip the signal at the brightest points of the image.

#### 2.2.4 Seeding Particles

In order to obtain the most accurate results, the particles used to seed the flow should be neutrally buoyant so as to truly follow the local flow. From past experience, the seeding particles that work best with the described setup are Sphericiel® hollow glass spheres manufactured by Potters Industries Inc. (designation: 110P8). The particles have a mean particle size of 9-13 microns and a density of about 1.1 g/cc which closely matches that of water. Silver coated glass spheres are also available and commonly used with some DPIV systems. These tend to reflect more light for brighter images, but are also slightly denser than water. Since the region of interest here involves highly rotational flows, matching the particle and water density is of utmost importance. The non-coated spheres reflected a more than sufficient amount of light for a good signal-to-noise ratio when the laser was operated at full output.

Assuming a spherical and neutrally buoyant particle that is operating in the Stokes flow regime, Merzkirch (*ref. 10*) gives the equation of motion as

$$\frac{du_p}{dt} = \frac{18\mu}{\rho_p d_p^2} (u_f - u_p) = K(u_f - u_p) \quad (2-3)$$

where  $u_p$  is the particle speed,  $u_f$  is the local fluid speed,  $\rho_p$  is the particle density,  $d_p$  is the particle diameter, and  $\mu$  is the fluid viscosity. The solution to this equation for a constant  $u_f$  is

$$u_p = u_f [1 - e^{-K(t-t_0)}] + u_{p_0} e^{-K(t-t_0)} \quad (2-4)$$

For a particle released into a flow at  $t = 0$  with zero initial velocity, the particle speed is

$$u_p = u_f (1 - e^{-Kt}) \quad (2-5)$$

For the Sphericiel® particles used in this study,  $K \approx 1.65 \cdot 10^5$  /sec and the response time of the particle (the time to reach 63% of the fluid speed) is approximately  $6\mu$ sec.

Although Eqn. (2-3) can only be used for small Reynolds number, it has been shown that even when the fluid and particle velocity difference exceeds a Reynolds number of 1, the particle's approach speed to the fluid velocity will be even faster than predicted by Eqn. (2-5) (*ref 11*). Thus, for the particles chosen in this study, the particle speed and motion can be assumed to closely match that of the fluid.

Roughly four tablespoons of seeding particles were enough to initially seed the entire tunnel. Re-seeding was done before each experiment with about one tablespoon of particles to make up for the particles that had settled after the tunnel was stagnant for more than one day. Past researchers in this same tunnel found it necessary to use hydrogen bubble seeding to get a sufficient amount of light reflection for image acquisition due to the less powerful Argon-ion laser used in their setup (Edmunds, *ref.12*, Srigrarom, *ref.13*). This made the particles positively buoyant which raises questions on their ability to accurately follow the flow. The Nd:YAG laser used in this study was much more powerful and allowed the use of nearly neutrally buoyant particles which is considered to be a major advantage over the past research.

#### 2.2.5 *Computer and Software*

A Bitflow Road Runner (2.50) frame grabber was used in conjunction with the digital camera. PixelFlow™ 2.1 software developed by General Pixels was used as the operating software to setup and run the experiments, as well as process the raw images, gather statistical averages, and plot the results. The PixelFlow™ *Installation and User's Guide* provides a detailed system description and parameters (*ref. 14*).

### 2.3 *Specific DPIV Experimental Setup*

When one dissects a flow with a laser sheet, a two-dimensional planar view of that flow is produced. This section will describe some of the past flow plane views observed by other researchers, and give a detailed description of the current flow planes, along with details of the parameters and method used in this study to capture each flow plane.

### 2.3.1 Previous and Current PIV Measurement Planes

A study of delta wing vortex flows using PIV was accomplished by Shih and Ding (*ref. 15*). Their study involved two different flow planes; the vortex core plane and the cross-stream plane. The vortex core plane was aligned with the center of the LEV core and allowed for the measurement of axial velocity and azimuthal vorticity along the axis of the leading edge vortex. The cross-stream plane was aligned completely normal to the freestream velocity and used to measure the azimuthal or theta velocity,  $u_\theta$ , along with the axial component of vorticity,  $\omega_z$ .

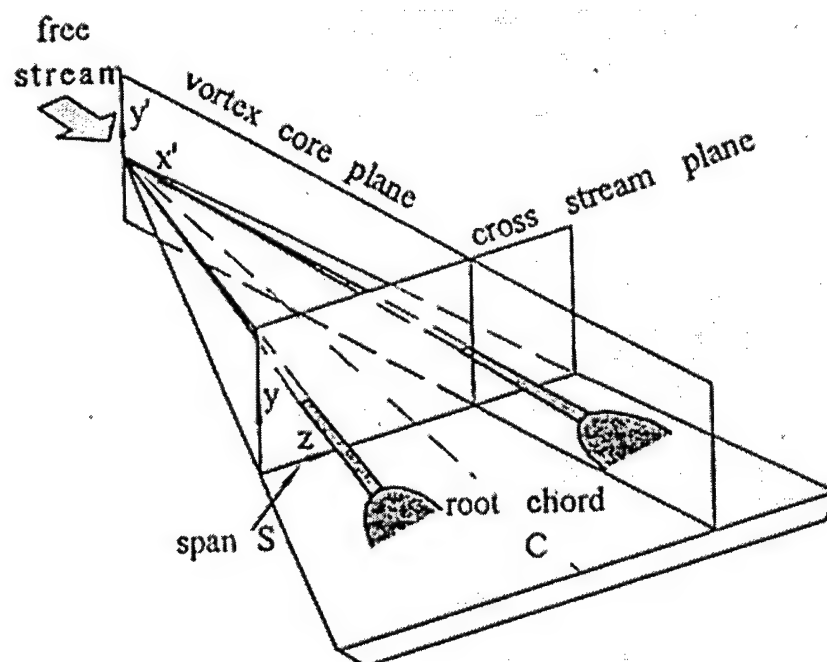


Figure 2-4: PIV measurement planes used by Shih and Ding (*ref. 15*)

The vortex core plane and the cross-stream plane were also used in the present study, with one difference being that in the cross-stream measurements, the plane was angled such that it was perpendicular to the vortex core instead of being totally normal to the freestream flow. The present study is mainly aimed at measuring  $u_\theta$  in the vortex core, and the measure of the circulation in the primary vortex. To achieve this as accurately as possible, a third plane was used which was set up exactly normal to the apex vortex core itself. This will be called the cross-core plane, and allows for the most

accurate measurement of velocities that are truly the azimuthal components of the vortex. Figure 2-5 shows the three planes used for the present study.

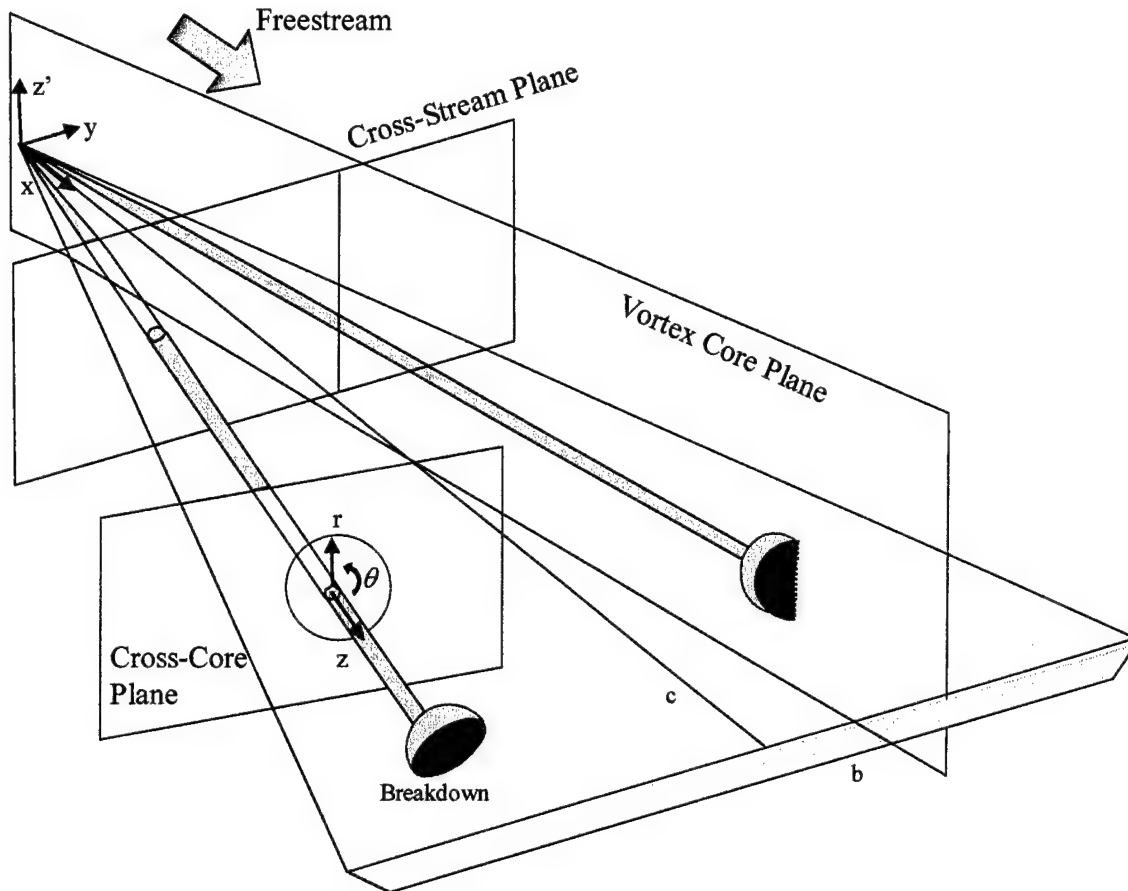


Figure 2-5: PIV measurement planes used in this study

### 2.3.2 Detailed Physical Description of Experiments

The specific arrangement used to capture fluid velocities in the above three planes will be discussed here. In order to obtain data for the plane of interest, illumination of that plane is critical. Arrangement of the optics to properly do this proved to be one of the most time consuming and difficult tasks of this experiment. The three different measurement planes each required a significant variation in optics arrangement. Each was chosen so that the distortion of the field of view was minimized, and so that the scattering of laser light by the plexiglass wing did not interfere with the region of interest. Figure 2-6 shows the orientation of the light sheet in relation to the delta wing, water

tunnel, and camera view. All three drawings are from the view of a person standing in front of the main tunnel test section. Placing the delta wing upside-down in the test section allowed for the optics to be easily arranged on the ground and for the sheet to cut the plane of interest before passing through the plexiglass wing surface which would scatter the light and distort the image.

The mirror used with the camera in the cross-stream and cross-core planes was a circular, 20cm diameter, flat front-surface coated and polished mirror which minimized distortions and allowed for the best camera focusing on the particles. A common rear-surface coated mirror was initially used, but it was found that focusing the camera lens on the plane of interest was impossible due to distortions of the light as it traveled through the glass to the reflective surface. Previous studies (*ref. 16*) have shown that objects in the near wake of a delta wing increase the adverse pressure gradient, and cause breakdown of that vortex to occur farther upstream. With this in mind, the mirror was placed about two wing chord lengths downstream of the wing. As observed with dye, the breakdown location for the vortex with the mirror behind it was the same as that of the vortex without the mirror in its wake. It was concluded that two chord lengths allowed enough spacing between the wing and the mirror such that it had little effect on the actual flow field.

For the cross-stream and cross-core plane, the camera was positioned so as to get the best view of the illumination plane, and be as normal to the plane as possible so that the entire region could be brought into focus. In setting up the cross-core plane experiment, dye was first injected at the leading edge into the core of the LEV, and the mirror and camera were adjusted so that the dye in the core appeared in the camera view as a single circular point. Using this technique, it was assured that the camera view was directly down the core of the vortex.

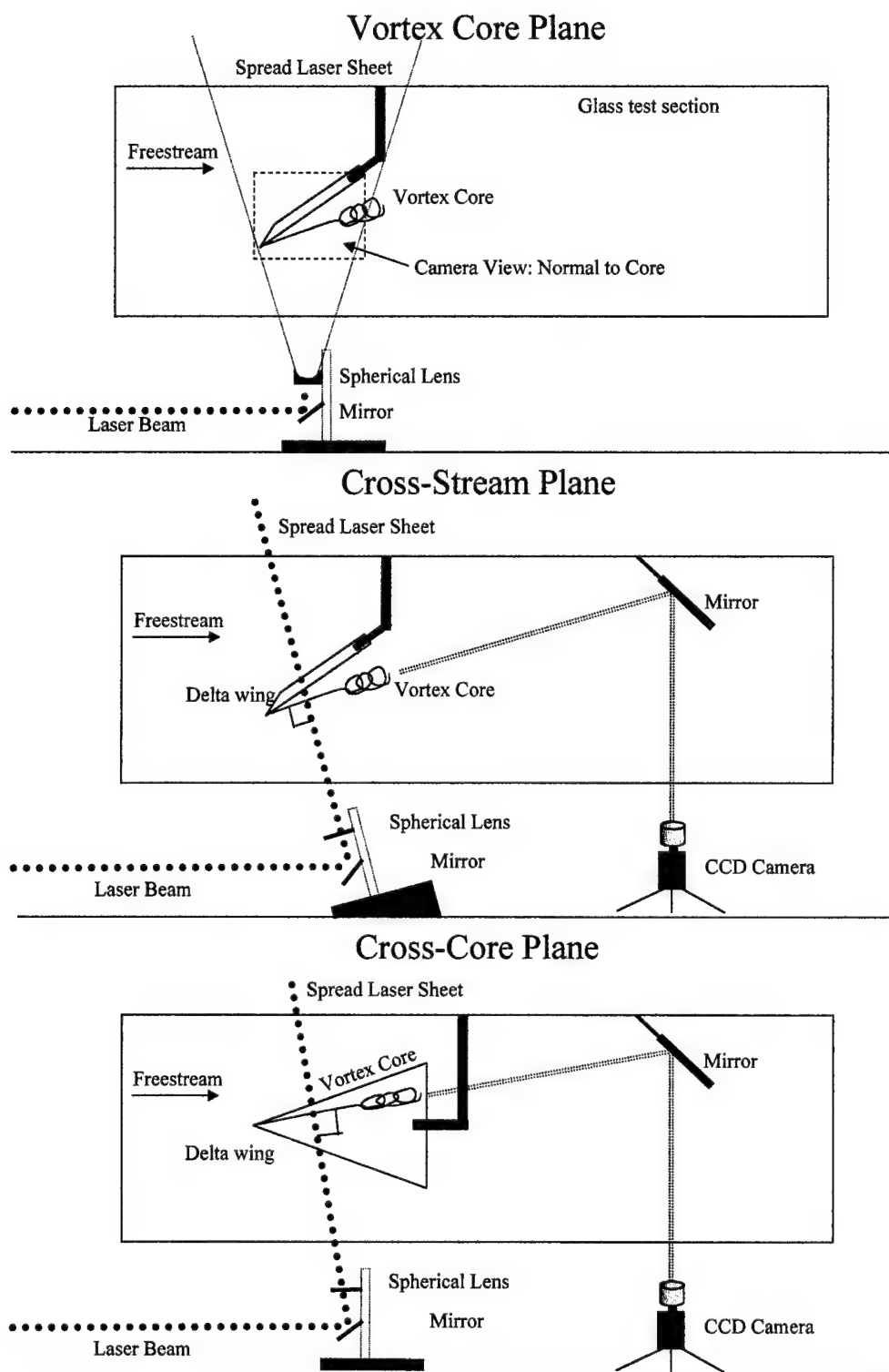


Figure 2-6: Overview of experimental setup for capturing all three planes

When viewing the vortex core plane, dye was also injected at the tip of the delta wing so that it entered the core of the vortex. The concentrated dye reflects laser light very well, so the laser sheet was then aligned so that it illuminated the entire length of the vortex core up to, and including, the breakdown location. The camera was then aligned perpendicular to the laser light sheet plane.

The distance between the camera and the plane of interest illuminated by the laser sheet averaged 1.2m for all planes of study. This allowed for a viewing area of about 12cm x 12cm which was large enough to capture all the significant flow features. This distance was adjusted slightly based on the individual requirements of each plane. The camera aperture was generally set in the full open position to allow for a maximum of reflected particle light to enter the device. The gain of the camera was set so that the brightest particle image signal was not clipped. The laser was generally operated at low power for the purpose of aligning the sheet, but then the high power setting was used when collecting data allowing for the brightest images.

The thickness of the laser sheet was controlled in order to minimize the error due to out of plane movement by the particles, which leads to a high number of outliers once the images are processed. The distance between the two cylindrical lenses described in section 2.2.2 was set to achieve the desired thickness of the sheet in the area of interest. For all three planes, a sheet thickness of about 2mm was found to produce images with the least number of out of plane losses. This was larger than the minimum thickness possible, so in effect the sheet was defocused slightly to produce the best results. Figure 2-7 shows the arrangement of the optics. A spacing of about 8cm between the two cylindrical lenses allowed the sheet to focus in the region of interest, approximately 4.75m from the second lens.

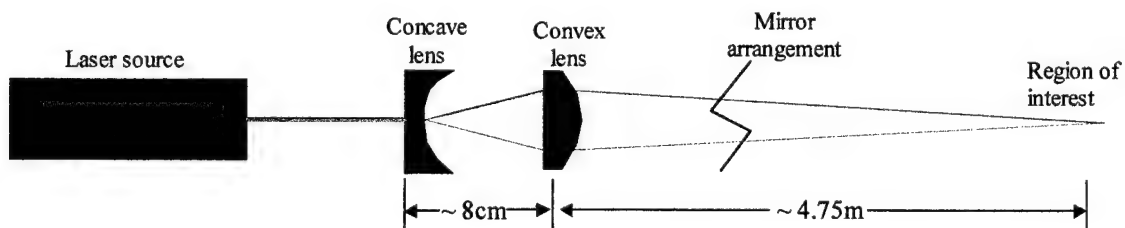


Figure 2-7: Diagram of cylindrical lenses to control light sheet thickness

Since the images seen by the camera are used to produce real velocity vectors, it is important that the images are not distorted in any way so that the vectors accurately reflect what the real fluid velocity vectors of the flow are. When viewing a grid of orthogonal lines placed in the region of interest, the camera image after it has passed through the water, the reflective mirror, and the glass sides of the water tunnel, should be the same orthogonal set of lines. To ensure distortion free camera views, a grid was placed exactly where the laser light sheet was in each of the three planes discussed above. The sample camera view of the grids is shown in Figure 2-8. These images reveal that there is no distortions or skewing of the image, and the entire region can be brought into focus.

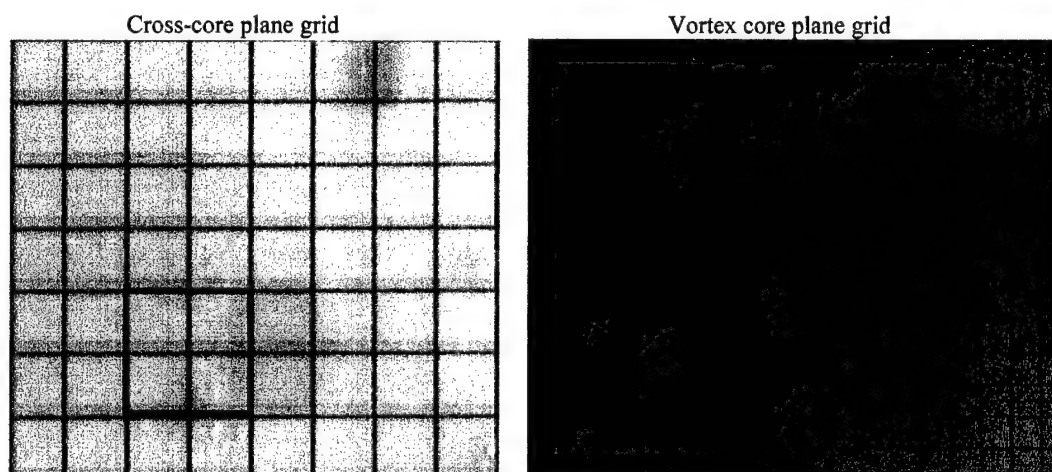


Figure 2-8: Grids showing distortion free images

These grids were also used when calibrating the DPIV system so that the pixel domain could be converted to the real domain. The grids had known spacing, and the software allowed for measurement of this spacing in pixels so that the conversion factor of cm/pixel could be determined. The software's final step was to convert the domain, and then rotate the image if required so that the data could be presented in a traditional view.

Figure 2-9 captures a sample firing of one of the lasers and illumination of the particles. Red dye is included just to show the relative position of the LEV and breakdown. In general, dye was not used, and the dye probe was pulled out of the tunnel when collecting actual data for processing. The particles in the picture are not entirely in



focus as this was taken with a conventional color digital camera which focused on the wing itself instead of the illumination plane.

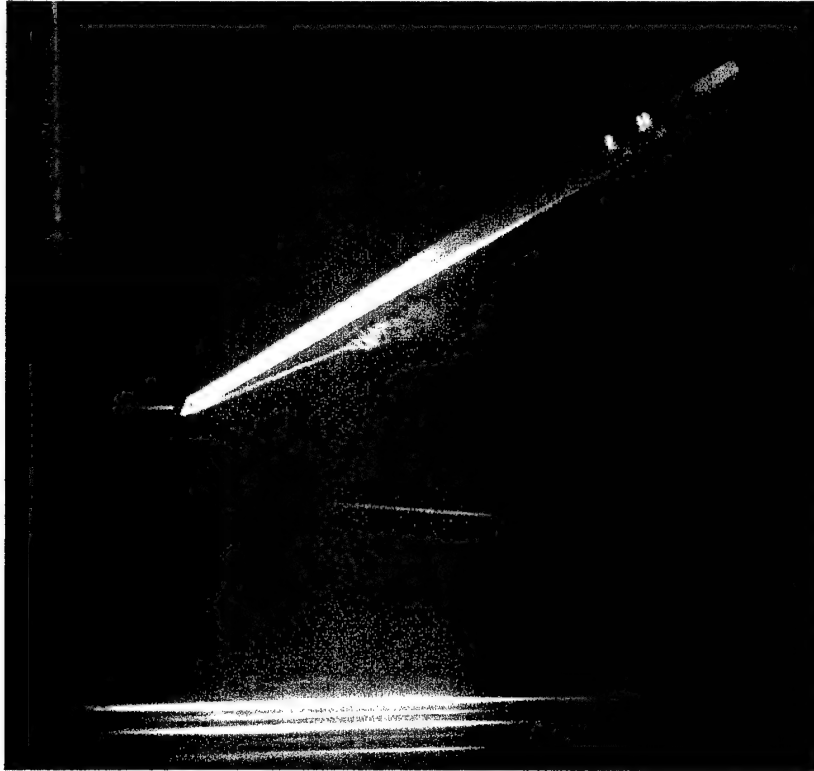
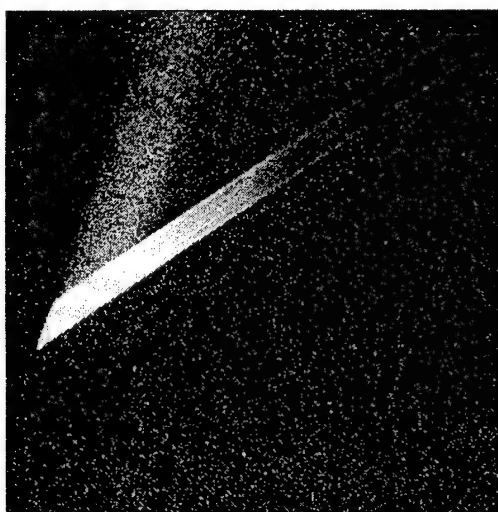
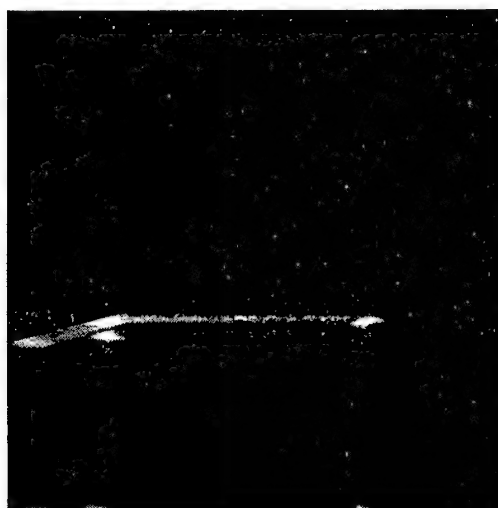


Figure 2-9: Sample picture of laser firing and particle illumination

The actual CCD camera used for acquiring the raw images was synchronized with the laser pulses, and was therefore able to focus entirely on the particles in the plane of interest. A sample raw image acquired by each of the three planes described above is shown in Figure 2-10.



Vortex core plane



Cross-stream plane



Cross-core plane

Figure 2-10: Sample raw images from each of the capture planes

As can be seen in Figure 2-10, laser light passing through plexiglass placed at any angle causes a scattering of the light. This scattering showed up in the images, and could at times be enough to interfere with the region of interest. This is why it was important to place the wing upside-down in the tunnel and shine the light up from the bottom so that any scattering that took place happened outside of the region of interest. The DPIV method is unable to distinguish between small impurities inside the plexiglass wing and the actual fluid particles. This makes it necessary in post-processing of the data to distinguish between actual fluid velocity vectors, and erroneous vectors which are sometimes placed inside where the wing should be. Fortunately, these vectors are small in magnitude and can easily be distinguished from the fluid flow vectors. However, slight misalignment of the two laser heads can lead to perceived particle shifts in the images. Every effort was made to align the laser heads as close as possible, and minimize this effect. Also seen in the cross-stream and cross-core plane are the mirror-like reflections of particles in the wing surface itself. Interestingly, that portion of the image looked like an exact mirror image of the actual vortex after processing. All of these vectors were edited out after processing, and all vectors shown in the results section are actual fluid velocity vectors.

### *2.3.3 Detailed Processing Parameter Description*

Many parameters of each experiment can be chosen and modified through the PixelFlow<sup>TM</sup> software. The most commonly used parameters are described in this section.

The manual suggests choosing the interrogation window size such that at least seven full particles are present in the image pair for correlation. After observing the particle density in the flow and based on the distances from which the camera viewed the region of interest, a window size of 32x32 pixels was chosen for all experiments. This allowed for good correlations and a high degree of certainty in the velocity vector resulting from the correlation. A step size of 16 pixels between interrogation windows was taken which led to a 50% overlap of the interrogation windows. Overall, this choice

had the least number of outliers, and a resolution of vectors which could accurately illustrate the flow field.

A critical parameter in any PIV experiment is the choice of the pulse separation time. Too short of a pulse separation will make it difficult for the correlation to detect any particle shift, and too long of a separation will cause a bad correlation between the two images of the pair because of the shift of particles outside of the interrogation window. The manual calls for a particle shift to be no larger than one-third of the window size. The pulse separation was varied based on the freestream velocity of the tunnel so that an average image shift was between one and two full pixels, meeting this criterion. For example, in the cross-core plane when a freestream speed of 10cm/s was used, the pulse separation was 2 microseconds. Slower freestream speeds meant that the pulse separation time could be increased. For all experiments, pulse separations between 1 and 4 microseconds were used.

In the processing of the images, the software allows for a variety of steps so that an accurate vector field is captured. The following sequence was used on all image pairs captured, unless otherwise noted. First, a cross-correlation as described above was done on the image pair to get a raw vector field in the pixel domain. Next, outliers were identified and replaced using a threshold value of 3 pixels. Then, a second cross-correlation with window shifting was run based on this first correlation. This method has been shown to reduce the uncertainty of DPIV cross-correlations to within 1% and aid in noise reduction. (*ref. 17*). After this step, outliers were again replaced, and a smoothing routine was run to remove high-frequency jitter that is inherent in DPIV processing. The manual claims this smoothing can be done without the loss of information in the field. The pixel domain was then converted to the actual physical domain using a conversion factor specific to each experimental run. The image could also be rotated in this step for presentation purposes, as was necessary for the cross-core plane data. The vorticity of the field was then calculated based on the velocity vectors. An integration approach using the eight surrounding vectors is used to calculate circulation, which is then divided by the area to arrive at a mean scalar vorticity value at each point. The whole process

was relatively quick, as a sequence of 30 image pairs could be processed in about one minute.

#### 2.3.4 Vector Post-processing and Circulation Calculation

The PixelFlow<sup>TM</sup> software includes a plotting package that was used to plot all velocity and vorticity fields. However, for obtaining plots of axial and azimuthal velocity, as well as circulation of the vortex, it was convenient to export the data into an ASCII format with  $x, y$  location and  $u, v$  components of each vector. This data could then be read into Matlab and processed with specific code to generate the required plots. The method used to calculate the velocity components and circulation is really quite standard and straightforward, but it is presented here for clarity and reference.

When the velocity vector field is known, much insight can be gained from calculating the velocity components tangent and normal to a line drawn in the field. To do this, a customized program is used where the starting and ending points of the line are chosen:  $(x_1, y_1)$  and  $(x_2, y_2)$ . The number of vectors in the field,  $n$ , is known, so the number of rows and columns is  $\sqrt{n}$  since the vector field is square. The length of the chosen line is calculated, and then the number of discrete points,  $N$ , where the tangent and normal velocities to the line are found is calculated as

$$N = \frac{\sqrt{n} \cdot L}{X} \quad (2-6)$$

where  $X$  is the real size of one dimension of the velocity field. The distance between one point and the next,  $dl$ , is then set equal to  $L/N$ . The unit vector in the direction of the line at the point of interest  $(x_p, y_p)$  is then calculated knowing the slope of the chosen line,  $m$ , as:

$$u_{unit} = \sqrt{\frac{1}{m^2 + 1}} \quad (2-7)$$

$$v_{unit} = \sqrt{\frac{1}{\frac{1}{m^2} + 1}} \quad (2-8)$$

The program then chooses the velocity vector with its origin closest to the point of interest. This vector is at  $(x_i, y_i)$  with velocity components  $(u_i, v_i)$ . The tangent and normal components are then the dot product and cross product of this vector with the unit directional vector respectively. This is done for all points on the chosen line, and the velocities are plotted. A diagram is included in Figure 2-11 for clarity.

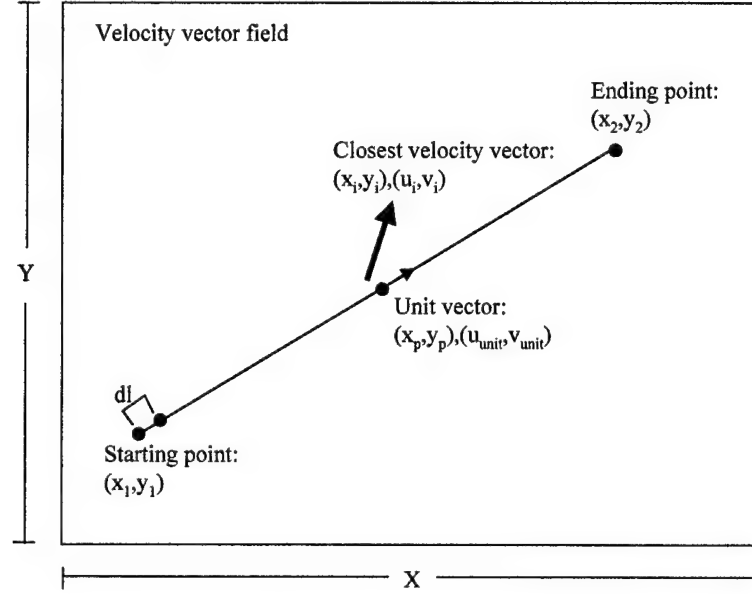


Figure 2-11: Calculation of tangent and normal velocities to a line

Much insight can also be gained by knowing the circulation of a vortex. The circulation around a closed path was defined in the introduction as:

$$\Gamma = \oint_C \vec{u} \cdot d\vec{l} \quad (2-9)$$

This study will use the standard convention of traveling in the counter-clockwise direction for evaluating this integral. For calculating the circulation of the LEV, a similar method to the above was used. A circular path of radius  $R$  and center point  $(x_o, y_o)$  was chosen with its center at the center of the vortex core. This center point was chosen by observation of the velocity field. The number of discrete points on the circle where the dot product was calculated was chosen similar to above, and then the distance,  $dl$ , was found as  $dl = R \cdot d\theta$ . The vector,  $d\vec{l}$ , was then calculated as

$d\vec{l} = -dl \cdot \sin \theta \hat{i} + dl \cdot \cos \theta \hat{j}$ . The dot product,  $\vec{u}_i \cdot d\vec{l}_i$ , was then evaluated at each chosen

point as  $\theta$  was varied from 0 to  $2\pi$ . The integral in Eqn. (2-9) was then discretized such that

$$\Gamma = \sum_{i=1}^N \Gamma_i = \sum_{i=1}^N \vec{u}_i \cdot d\vec{l}_i \quad (2-10)$$

A diagram is included in Figure 2-12 for clarity.

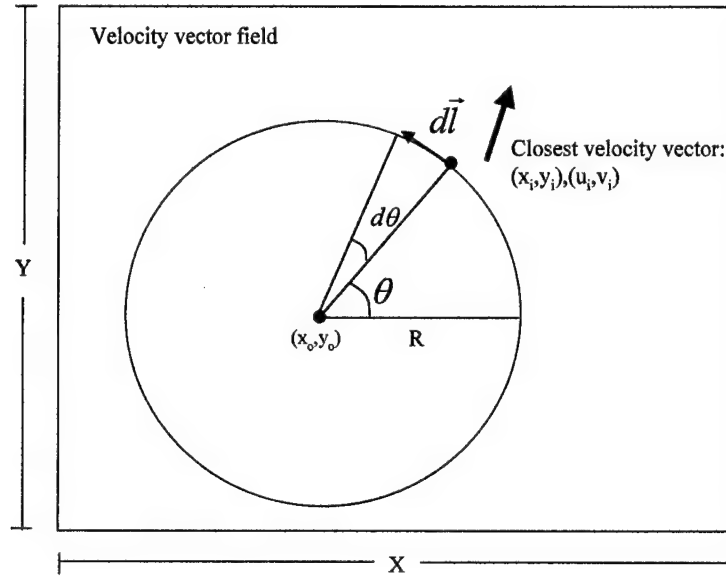


Figure 2-12: Circulation calculation around a closed circular path

The circulation was found to vary greatly with the radius at which the closed path was formed. That being the case,  $R$  was made an input parameter and the circulation as a function of  $R$  could be plotted. The maximum circulation occurring inside the vortex core could then be inferred from plots of circulation vs. radius of integration.

### 3 Experimental Results

Vortex core plane and cross-stream plane results of the DPIV investigation will first be presented and compared with other similar studies that have been accomplished in the past. This will serve to validate the current DPIV method and setup, as these are the first formal results to come from this particular PIV system. It will also be used to validate the current results from the cross-core plane, as this plane has not been studied in the past. Then, the cross-core plane data will be used to look deeper into the nature of the LEV, and will seek to qualitatively and quantitatively define parts of the vortex. Dye visualization is also presented to support the DPIV results. This analysis will seek to provide further insight into the contributing factors of vortex breakdown in general, and above delta wings in particular.

#### 3.1 Vortex Core Plane Results

The vortex core plane, as defined in the experimental setup section, has been studied in the past using similar PIV techniques by Shih and Ding (*ref. 15*) and Towfighi and Rockwell (*ref. 18*). When looking at the vortex core plane of a delta wing at high angles of attack, it is expected to find an axial velocity gradient along the vortex axis. The velocity increases from the wing's apex to a maximum of a 2-3 times the freestream velocity depending on the angle of attack. After this, there is a general slowing of the flow due to an adverse pressure gradient, and if vortex breakdown occurs, a stagnation point develops which is usually used to define the point of breakdown. Prior to vortex breakdown, it is expected that the axial velocity will have a jet like profile, and after breakdown, a wake like profile will be seen (*ref. 13*). These aspects of delta wing flow have long been known. Werle' (*ref. 16*) used intermittent dye emissions to measure the axial velocities in the LEV of a  $75^\circ$  sweep delta wing at various angles of attack. He found that axial velocity rapidly decreased to zero at the vortex breakdown stagnation point. A plot of the axial velocity normalized with freestream velocity is shown next where  $i$  stands for wing incidence or angle of attack.



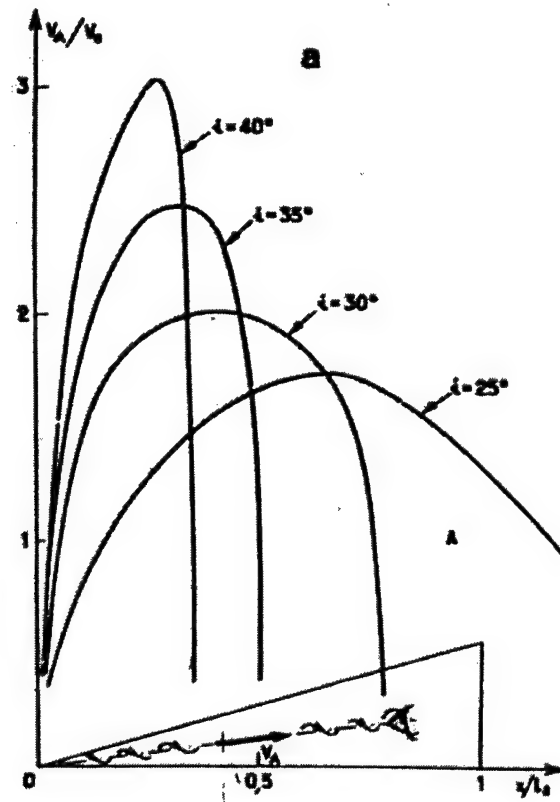


Figure 3-1: Axial velocity profile for various angles of attack (*ref. 16*)

This result was reproduced in the present study using DPIV on a  $65^\circ$  sweep delta wing at angles of attack from  $10^\circ$  to  $40^\circ$  and a chord length of 30 cm. Time averaged vectors are shown in Figure 3-2, and the related axial velocity profile as measured along the centerline of the vortex core is shown in Figure 3-3. The color of each vector represents its magnitude as given in the color bar.

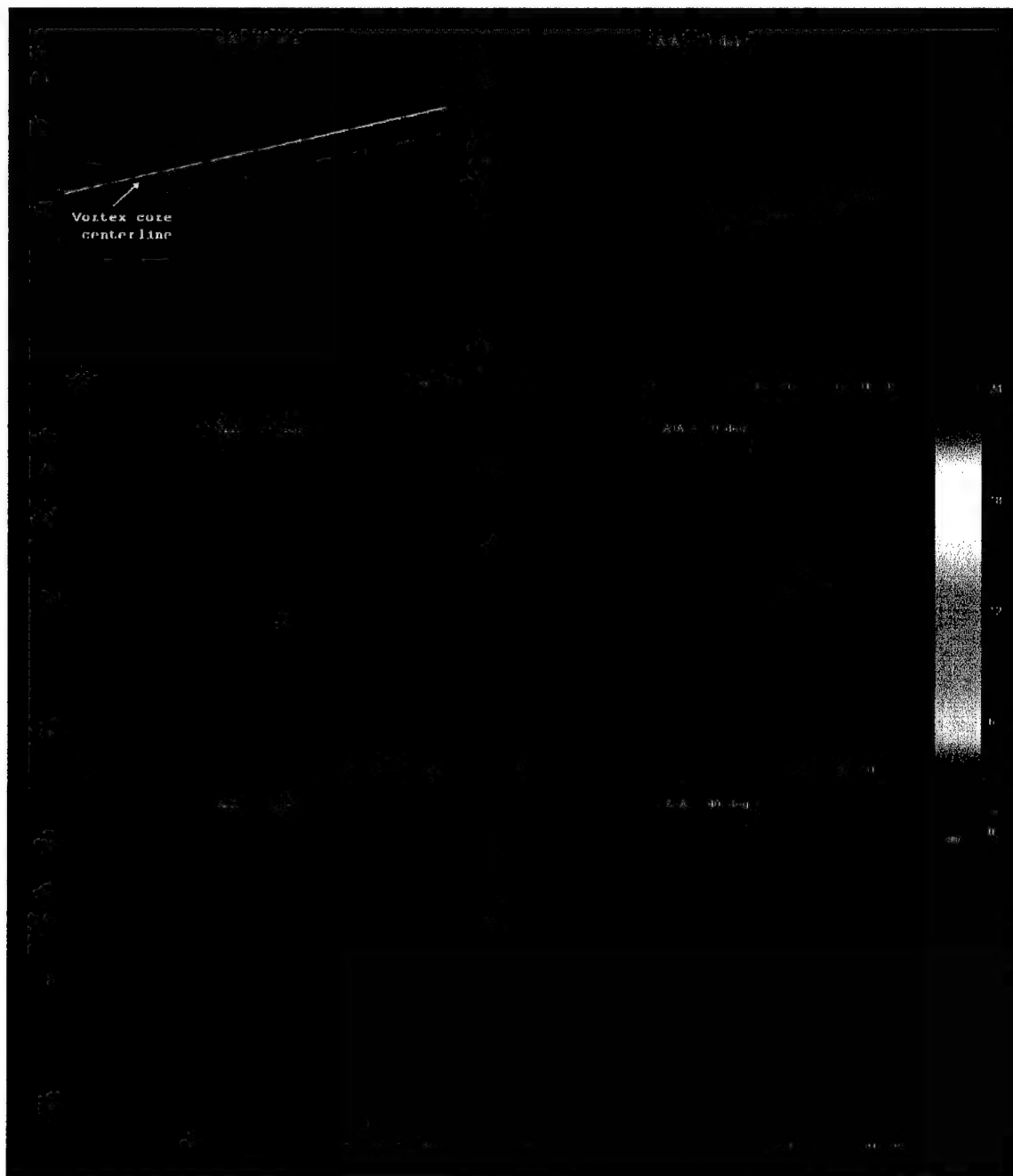


Figure 3-2: Velocity field for a 65° sweep delta wing at various angles of attack,  $U_{\infty}=10\text{cm/s}$ ,  $c=30\text{cm}$ , vortex core plane

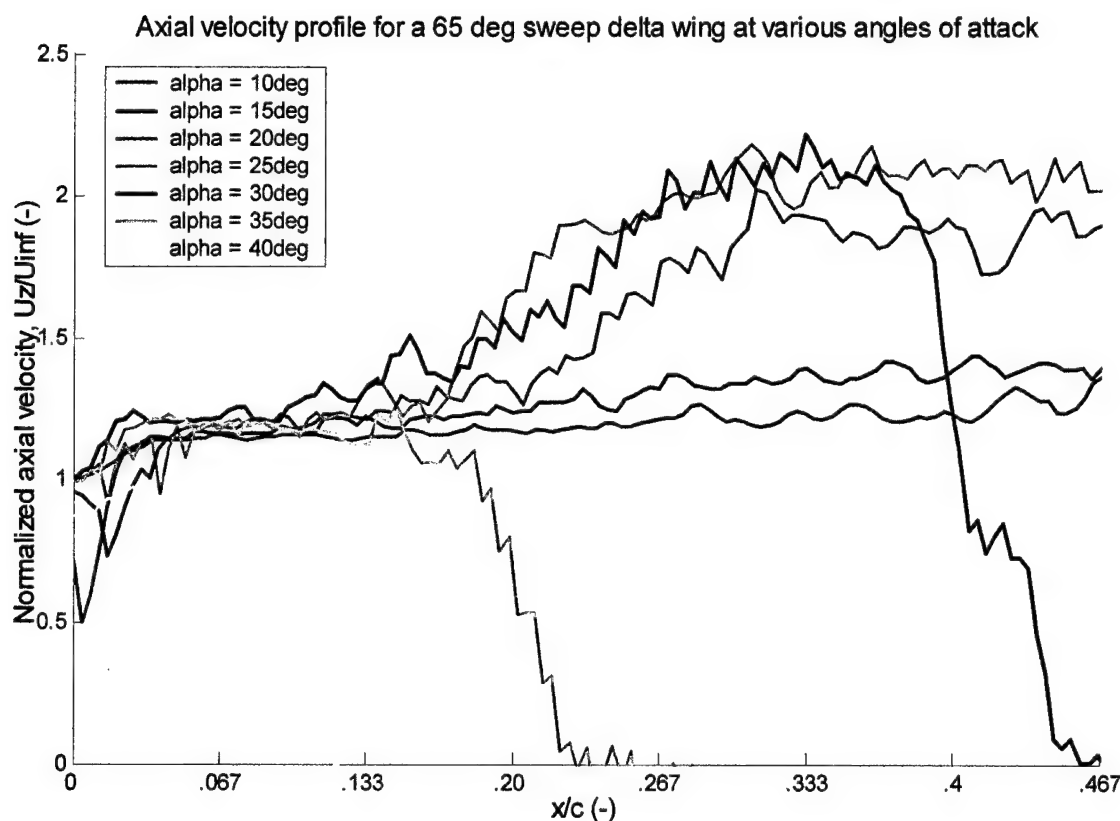


Figure 3-3: Axial velocity in vortex core vs. angle of attack

The jaggedness of the axial velocity plot is due to the discretization effects in how the velocities were calculated along the vortex axis, since a finite number of vectors exist and they are not exactly located along the centerline. A smaller window step size than that of the rest of the data presented in this study was used in the processing of these images in an attempt to smooth out this effect. As a result, the individual velocity vectors are not easily seen, but the general effect of angle of attack on axial velocity is the emphasis here. The axial velocity increases along the axis, tends to level off, and then falls to zero at the point of vortex breakdown as seen in the 30, 35, and 40° angle of attack case. The 20 and 25° case also lead to vortex breakdown, but it occurred outside of the camera view area which is only to about mid-chord, and thus not seen here. It should also be noted that even in cases where breakdown does not occur over the wing, there is a maximum axial velocity point, and then a general slowing of the flow due to the axial adverse pressure gradient caused by the high angle of attack. This is seen in both Werle's study and the present one. The delta wing is no different from a conventional

two-dimensional airfoil at moderately high angles of attack in this aspect. Plots of the pressure coefficient on the surface of the wing can be used to see this effect.

Shih and Ding used a PIV technique similar to this study and looked at flow over a delta wing with a leading edge sweep of  $75^\circ$  at a  $35^\circ$  angle of attack in a water towing tank. Their results showed a high axial velocity in the vortex core prior to breakdown, dropping rapidly to stagnation in the area of breakdown. They also found mainly steady flow prior to breakdown, along with unsteady and recirculating flow in the wake of breakdown. A sample of their results is shown in Figure 3-4. The non-dimensional times included show the non-steadiness of breakdown.

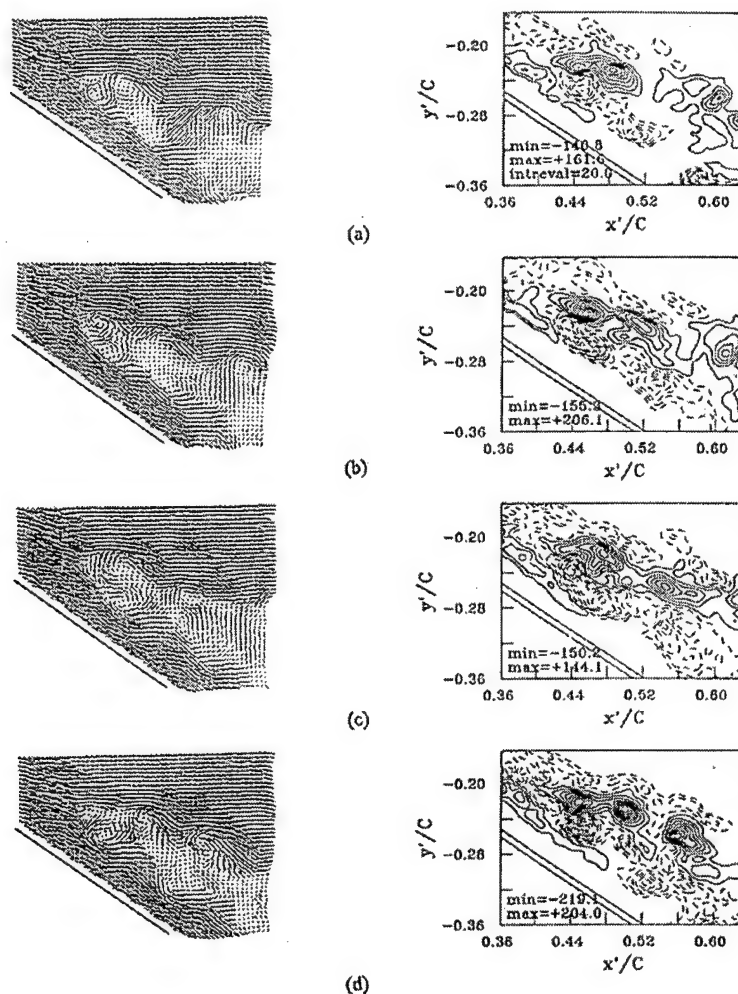


Figure 9 Instantaneous velocity and corresponding vorticity fields along the vortex core plane. AOA= $35^\circ$ . (a)  $t^*=0.0$ , (b)  $t^*=0.05$ , (c)  $t^*=0.11$ , (d)  $t^*=0.16$ .

Figure 3-4: Vortex core PIV results from Shih and Ding (ref. 15)

The data captured from the vortex core plane using the current method of DPIV shows much the same results. To further describe the aspects of the delta wing that the vortex core plane is capturing, dye was injected during the laser firing and image acquisition process. Figure 3-5 shows the dye and particles, which are illuminated by the laser, the velocity vectors that result from processing, and the superposition of the two images to correlate what is seen in dye visualization and DPIV. It can be seen that the radial expansion of the dye in the center of the core is just slightly upstream of the point where the axial velocity stagnates, and a region of reversed flow exists. Also, a boundary layer effect is evident in the small region surrounding the wing surface itself. This is probably more of an artifact of the cross-correlation technique used to process the images, as it is unable to distinguish fluid particles from the wing surface. Since the surface is stationary, a true particle shift will not be detected from one image to the next if the surface is part of the image window that is processed. This being the case, it is important to filter out these effects, and only rely on the results that spring from areas sufficiently far away from the wing surface. From experience, it was observed that only about one extra row of vectors outside the surface was affected by it, so these regions are blocked out in subsequent velocity and vorticity fields. The region of interest which is the core of the vortex and the breakdown region remain unaffected.

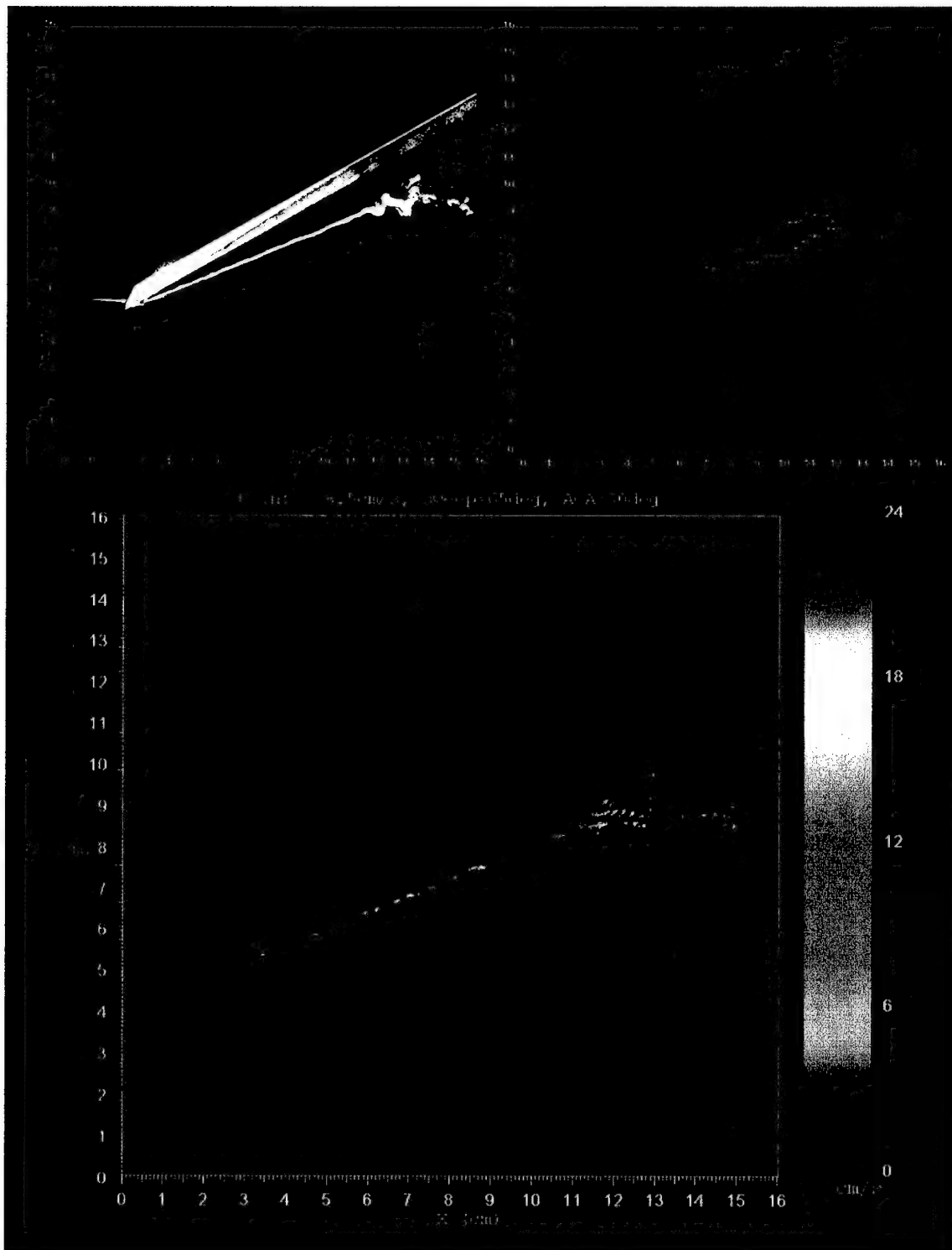


Figure 3-5: Dye and DPIV vector field superposition, 65° sweep wing, 30° angle of attack,  $U_{\infty} = 8.5 \text{ cm/s}$ , vortex core plane

Shih and Ding's study along with previous PIV research in this water tunnel (*ref.* 13) also find that the vorticity contours show an azimuthal vorticity sign switch slightly upstream of vortex breakdown. This aspect is characteristic of the breakdown location, and a well recognizable phenomenon. It also supports the idea of a transition from jet-like to wake-like flow during vortex breakdown. This aspect was obvious in the current study also. Figure 3-6 shows typical instantaneous velocity vectors and azimuthal vorticity contours from the vortex core plane of the  $c = 30\text{cm}$  delta wing. The region of highly non-steady reversed flow around the breakdown location is also seen.



Figure 3-6: Instantaneous velocity vectors and vorticity field for  $65^\circ$  sweep delta wing at a  $30^\circ$  angle of attack,  $c = 30\text{cm}$ ,  $U_\infty = 8.5\text{ cm/s}$ , vortex core plane

The non-steadiness of the flow inside the LEV is well documented. The vortex breakdown position has been found to oscillate and jump axially, even when upstream conditions are maintained constant. In this study it was observed using dye that the oscillations usually happened on fairly large time scales. That is, the breakdown position remains constant for a period of time before migrating up or downstream. This being the case, it is useful to average out the non-steadiness in the flow to obtain a picture that reveals the bulk flow properties of the vortex with breakdown in a relatively constant position, but averages out the small fluctuating velocities. This was accomplished by taking pictures of the flow over a two second interval. At a camera frame rate of 30 Hz, this meant that 60 images, or 30 pairs were obtained, processed, and then averaged to produce the mean velocity and vorticity fields. An example of the averaging effects is shown in Figure 3-7 for comparison with the instantaneous image in Figure 3-6. One aspect that is missing in the averaged images is the actual reversal of flow in the breakdown region. This is because the actual recirculating regions moved around rapidly, and so the net effect is just very small average velocities in the wake of breakdown.



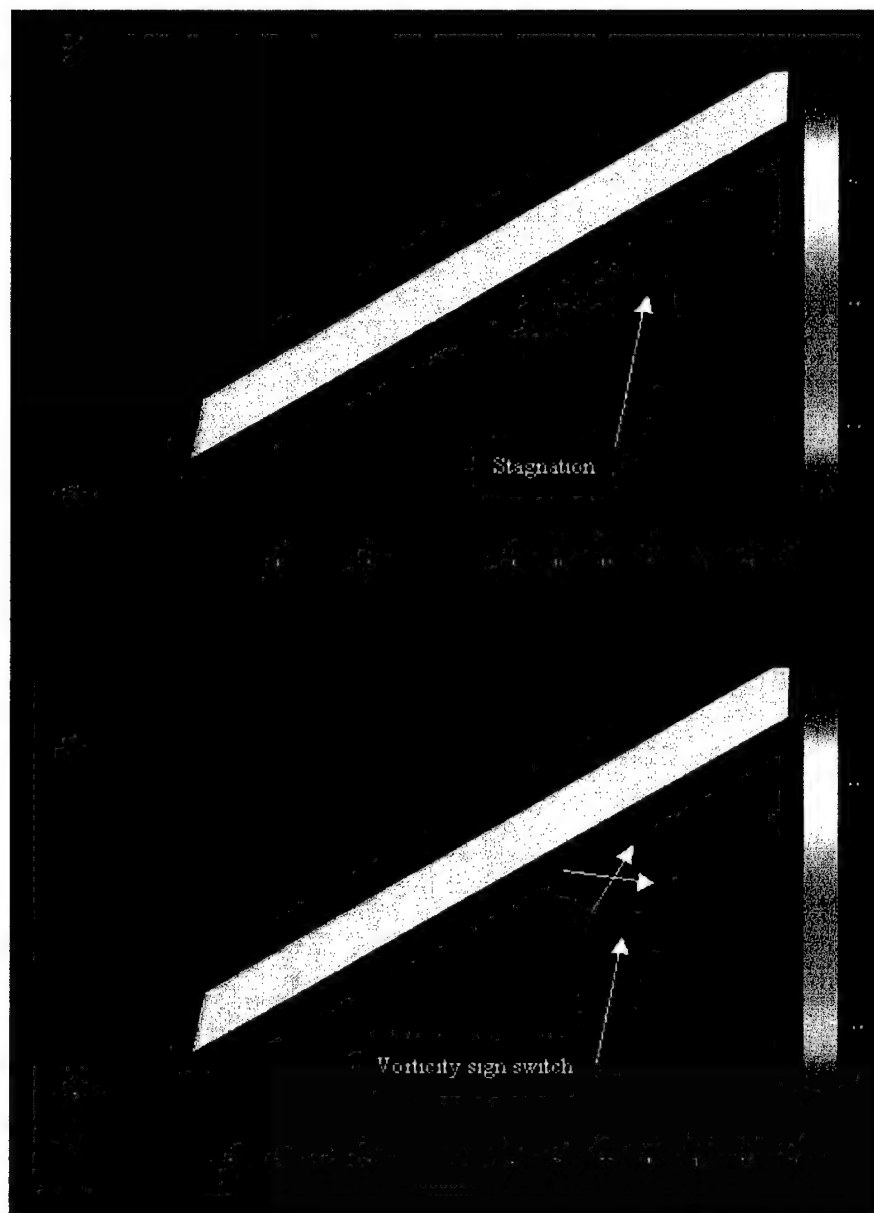


Figure 3-7: Two second average (30 image pairs) of vectors and vorticity field for 65° sweep wing at a 30° angle of attack,  $c = 30\text{cm}$ ,  $U_\infty = 8.5\text{ cm/s}$ , vortex core plane

The freestream velocity was increased to briefly study the effects of Reynolds number on the flow qualities around the wing. The wing used in Figure 3-7 had a Reynolds number based on chord of about  $\frac{U_\infty c}{\nu} = 2.3 \times 10^4$ . Increasing the velocity to 21 cm/s gave a Reynolds number of about  $5.75 \times 10^4$ . The two second average of the velocity field is shown next in Figure 3-8.

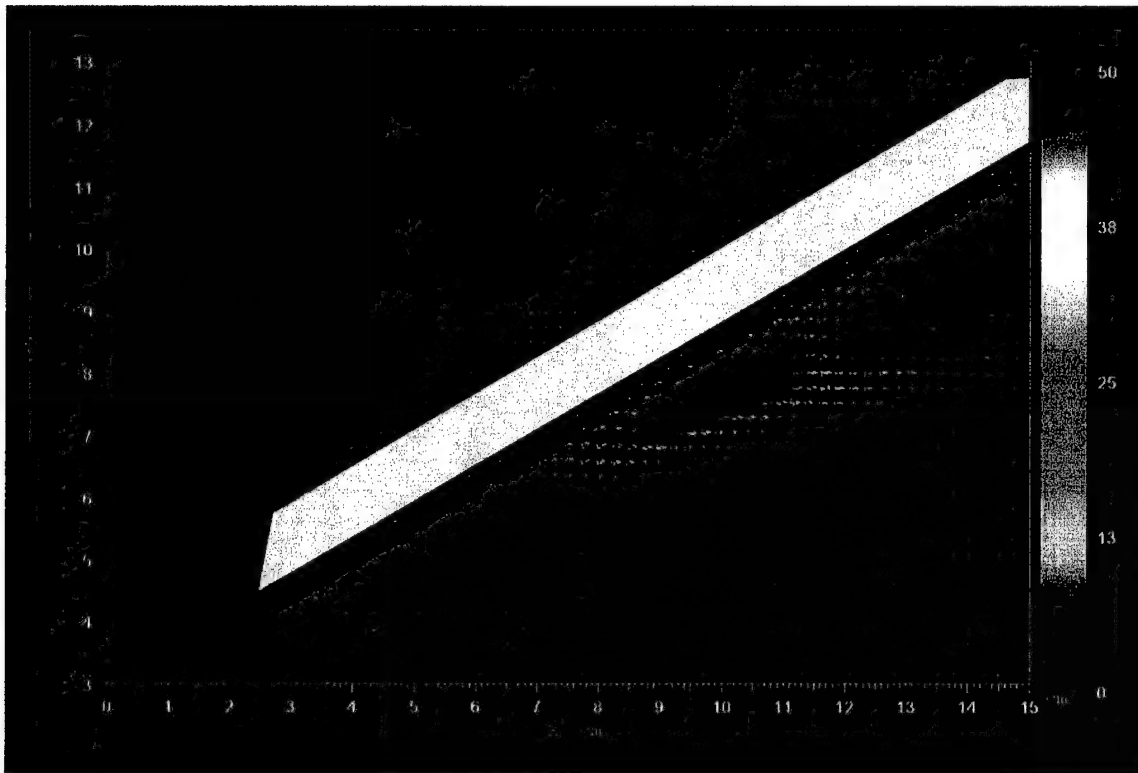


Figure 3-8: Two second average (30 image pairs) of vectors and vorticity field for 65° sweep wing at a 30° angle of attack,  $c = 30\text{cm}$ ,  $U_\infty = 21\text{ cm/s}$ , vortex core plane

The velocity fields at the two different Reynolds numbers are nearly indistinguishable; the only difference being the magnitude of the velocity vectors. This would suggest that the flow field will be qualitatively the same, regardless of what freestream speed is chosen from the speeds that are capable in this water tunnel. Erickson (*ref. 8*) provides information in his study on vortex flow correlations in a water tunnel and real world applications that suggests the flow over a delta wing is relatively invariant with Reynolds number.

Focusing on the vortex breakdown region will reveal aspects of breakdown that are evident in experiments, and predicted by the self-induction theory. As has been documented before by Cain and Srigrarom (*refs. 2,13*), the breakdown region contains a pile-up or slowing of the flow before breakdown, radial expansion of the flow, an azimuthal vorticity sign switch, and a turning point all leading to a stagnation and recirculation region. This can be seen in the DPIV results in Figure 3-9.

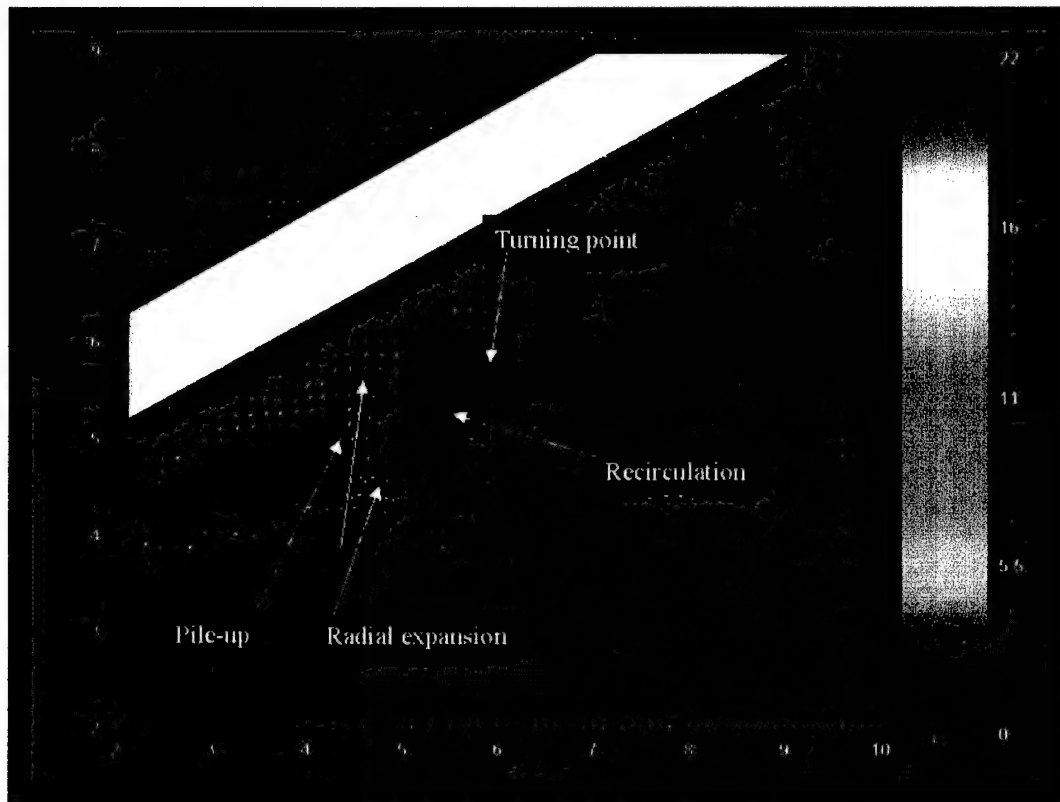


Figure 3-9: Close-up of vortex breakdown for 65° sweep wing at a 30° angle of attack,  $U_{\infty} = 21$  cm/s, vortex core plane

The vortex core view gives helpful insight into the nature of LEVs and the character of the flow both before and after vortex breakdown. However, to get a better view of the swirling component of the flow, including its formation and strength, the vortex needs to be viewed from behind the wing in a plane that is normal to the core itself. Other researchers have looked for this by using the cross-stream plane, which is presented next.

### 3.2 Cross-stream Plane Results

The cross-stream plane has been previously viewed by Shih and Ding using PIV, and by Mitchell et al. (*ref. 19*) using Laser Doppler Velocimetry. Each pointed out the cross-stream axial vorticity contours that are present at different chord locations with varying angle of attack. Sample results from Shih and Ding's experiment are shown in Figure 3-10, and Mitchell's results are in Figure 3-11.

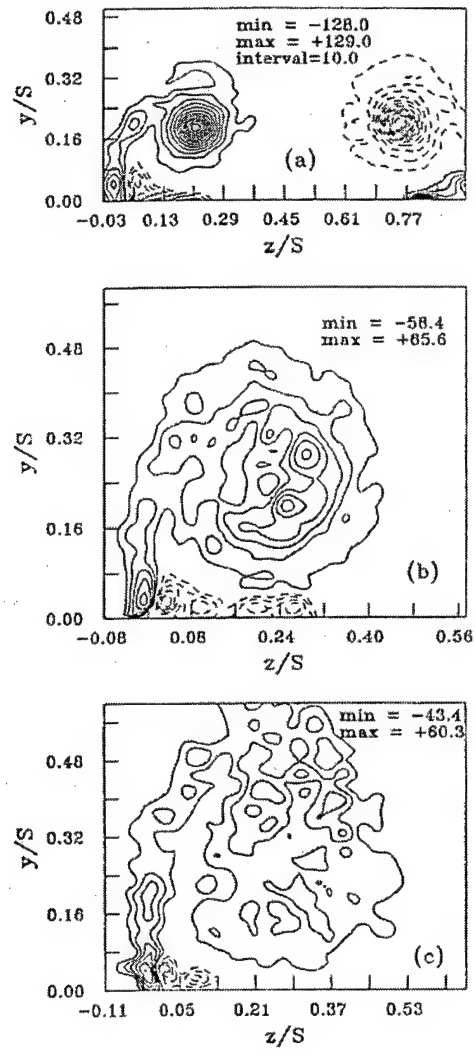


Figure 4 Time-averaged cross-stream vorticity fields at 75% chord. (a) AOA=27.5°, (b) AOA=31°, (c) AOA=35°.

Figure 3-10: Sample axial vorticity results from Shih and Ding's study (*ref. 15*)

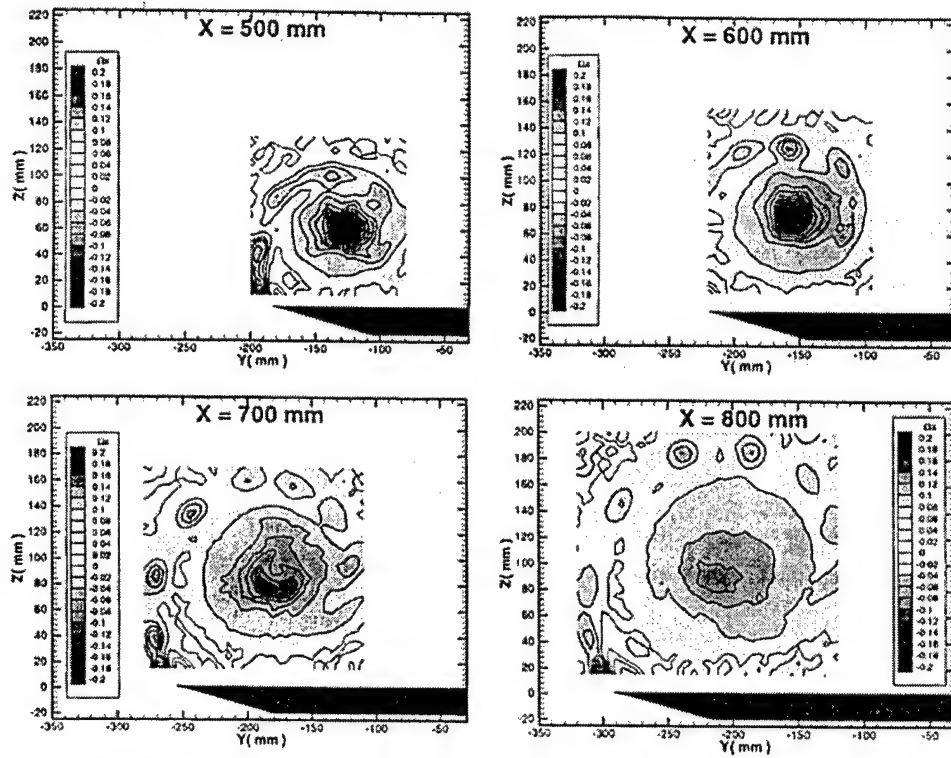


Fig. 9: 3-D LDV results showing the axial vorticity ( $\Omega_x$ ) at  $\alpha = 27^\circ$  and  $U_\infty = 24$  m/s (a)  $X = 500$  mm (b)  $X = 600$  mm (c)  $X = 700$  mm (d)  $X = 800$  mm.

Figure 3-11: Sample axial vorticity contours from Mitchell's study (*ref. 19*)

As can be seen, Shih et al. looked at one axial location and raised the angle of attack to get pictures before and after breakdown, whereas Mitchell used a constant angle of attack and varied the axial location of interest to see the same basic effect. Both studies concluded that there was a tight concentration and high value of vorticity inside the vortex core before breakdown, and that the vorticity was much more dispersed and random in the post-breakdown field.

In the present study, the cross-stream plane was briefly investigated to reproduce the general results found in the past, while most of the effort was put into the cross-core plane presented in the next section. A composite picture of velocity vectors was assembled using cross-stream plane data at four different axial locations. In the first two stations, both sides of the delta wing were visible in the camera's field of view. However, in the last two, only the right side LEV was visible, so the left hand side images presented in Figure 3-12 are simply mirror images of the right for completeness. The view is of the suction side of the 30cm chord length delta wing at an angle of attack of  $30^\circ$ , and a

freestream velocity of 8.5 cm/s. Vorticity contours are also easily produced, and matched the results found in the past, however, their presentation will be saved until the next section.

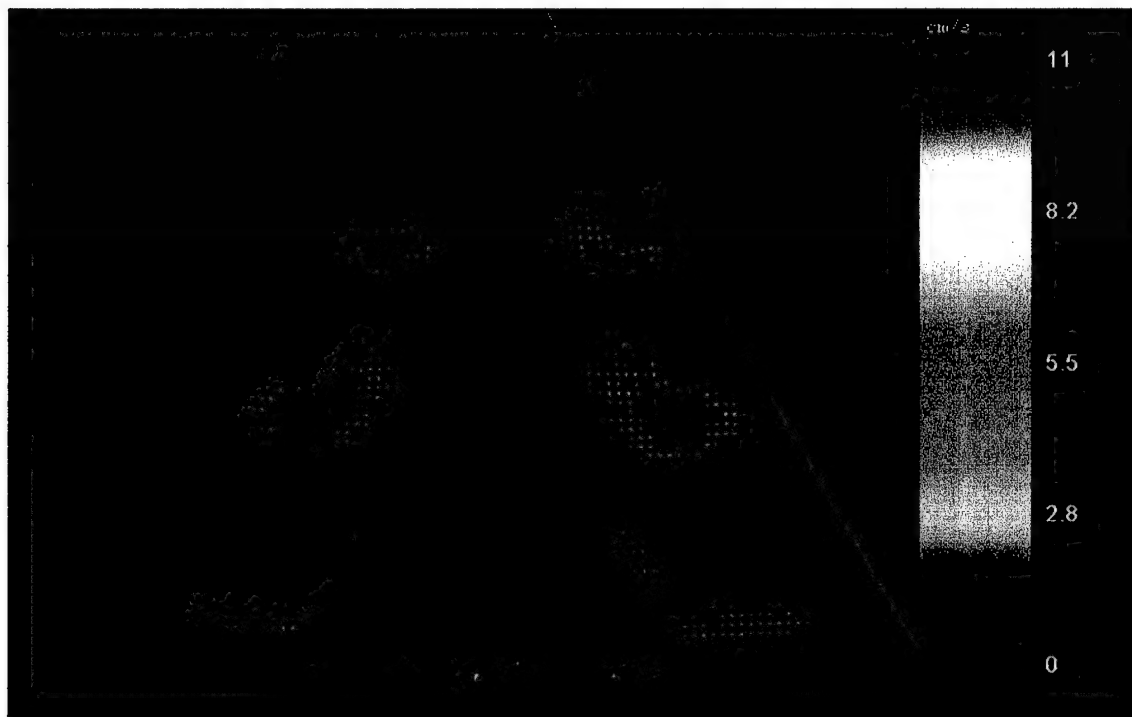


Figure 3-12: Composite velocity field for 30° angle of attack, cross-stream plane

While the cross-stream plane proves useful for looking at both LEVs, the view is not truly normal to the axis of either vortex. One of the questions that this study seeks to answer is how much vorticity and circulation is fed into the LEV, and especially into its core as one travels down the chord of the wing. The best way to do this is to look straight down the axis of the vortex, in an orientation that is normal to the vortex itself and not necessarily the wing or the freestream velocity. This view plane is termed the cross-core plane, as it dissects the core of the vortex itself. The actual vorticity and circulation of the vortex is then represented as accurately as possible using this plane.

### 3.3 *Cross-core Plane Results*

The analysis of the leading edge vortex has been purposely postponed until the present cross-core plane results section because it is believed to be the most accurate plane in which to measure circulation, vorticity, and the azimuthal velocities of the

vortex. As the delta wing sweep angle increases and approaches  $90^\circ$ , the cross-core and cross-stream plane become nearly the same plane. However, for more modest sweep angles, like the delta wing of this study at  $65^\circ$ , there is a measurable difference in the angle of the two planes. When looking in the cross-stream plane, the laser sheet dissects the core of the vortex obliquely and at some mean location, and the view for the inboard part of the vortex is farther upstream, while the outboard part of the vortex is seen at a location farther downstream than the mean location. This could cause confusion when drawing conclusions about the nature of the vortices. For this reason, the cross-core plane is used to analyze the vortex, and specifically the solid-body rotational core of the vortex.

As mentioned in the introduction, an ideal or Rankine vortex will have a core of fluid that behaves like a rotating solid-body, i.e. the azimuthal velocity ( $u_\theta$ ) increases linearly with the distance from the center. At some radius,  $r_c$ , the velocity will fall off, or vary inversely with the radius, eventually falling to zero. Real vortices, and in general the LEVs of a delta wing, also behave in much the same way. The azimuthal velocity increases up to a certain radius, reaches a maximum value, and then falls off as radius is further increased. For this study, the part of the vortex in which the azimuthal or theta velocity is increasing will be referred to as the core of the vortex. This is the part of the vortex where most of the vorticity is contained. The region outside of this core, where velocity tends to decrease with increasing radius, will simply be called the outer region.

As mentioned, two different size delta wings were used in this study, which was done mainly for ease of experimental setup. The wing for each different view was chosen based on the required camera view area, and the size of the LEV at the chord location of interest. In general, the larger wing worked out better for measurements at high angles of attack because vortex breakdown happened near the apex for these angles, and the larger wing area allowed for a bigger area which the camera was able to see in more detail. For the smaller angles of attack, the wings could be used interchangeably. Since it has been shown that changes in Reynolds number have a very small effect in this region of interest, no adjustment is necessary for each wing. For clarity, data is generally presented with the chord location normalized by the entire chord length.

### 3.3.1 *Velocity and Vorticity Fields*

The velocity vectors and vorticity contours will first be presented for the small wing at a  $20^\circ$  angle of attack and a freestream velocity of 10 cm/s. At this angle of attack, the core of the vortex was seen to breakdown between 58% and 67% chord. This data was taken over a two second interval, and then averaged. This again made it possible to see the bulk flow properties, and to ignore small scale fluctuations and non-steadiness. The velocity field is seen in Figure 3-13. In the first frame, the core of the LEV is beginning to form. The shear layer seen on the left of the image is feeding into the vortex. As one travels in the x-direction down the wing chord, the overall size of the vortex is seen to grow as this shear layer continues to feed fluid into the vortex. Presumably the size and strength of the vortex grows, which will be analyzed later. Upon reaching the location of vortex breakdown, between 58 and 67% chord, the velocities in the core of the vortex are seen to diminish, while the outer regions of the vortex remain relatively unchanged immediately. Traveling farther downstream, the breakdown region is seen to grow and encapsulate a greater portion of the vortex. Although not shown here, the instantaneous velocity fields reveal the non-steadiness of the post breakdown region.



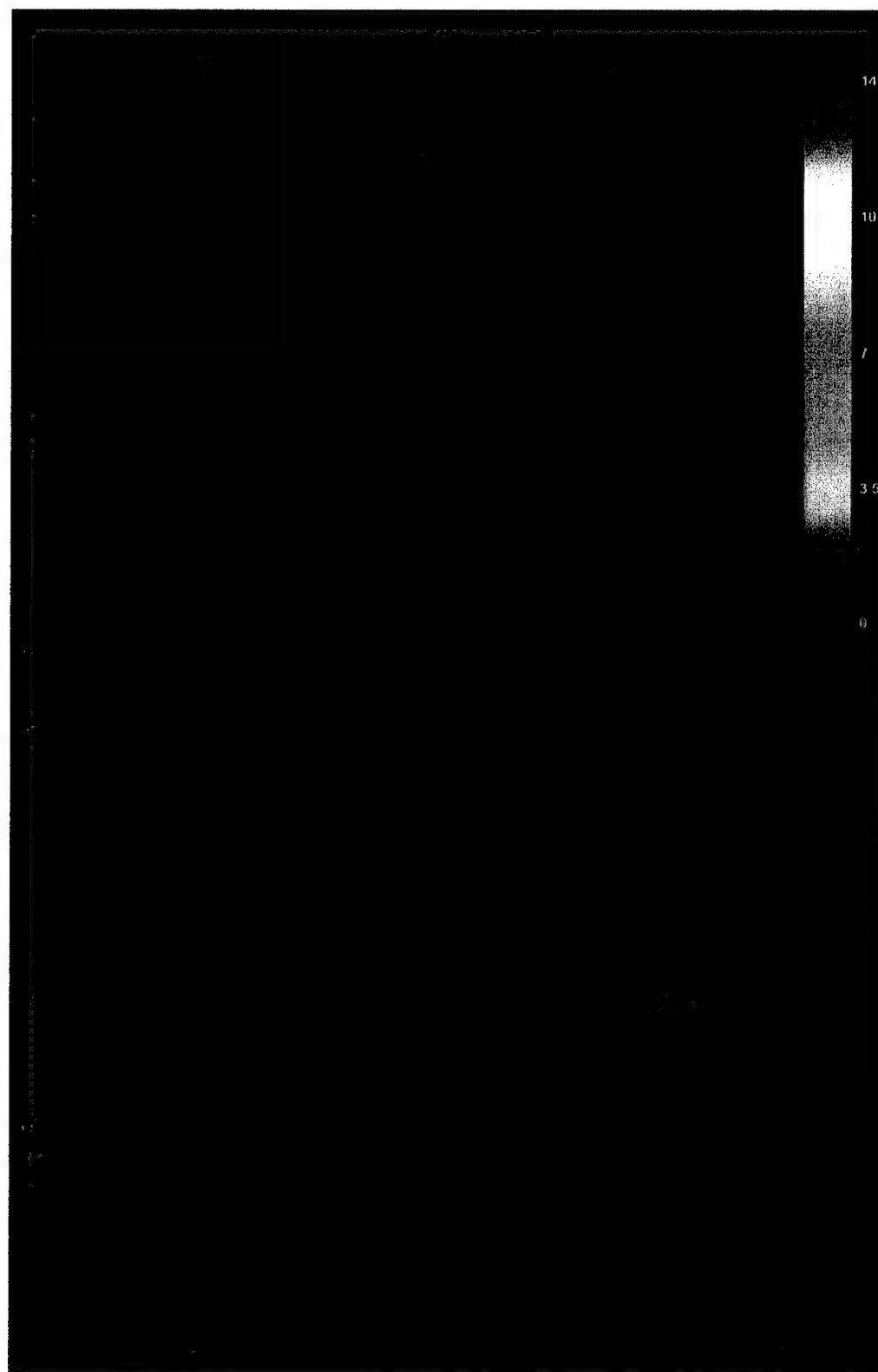


Figure 3-13: Velocity vector field for 20° angle of attack, cross-core plane

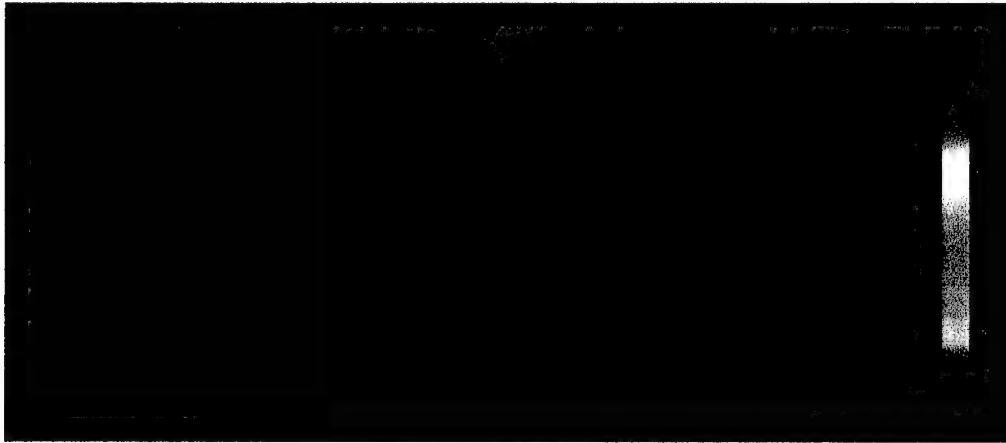


Figure 3-13(cont.): Post breakdown region, cross-core plane

The time averaged vorticity contours are shown next in Figure 3-14. They are only shown up to 67% chord since in the wake of breakdown, there is no longer a concentration of vorticity in the core. Since the core vorticity is then much more spread out, the non-steadiness causes the average value to be near zero.

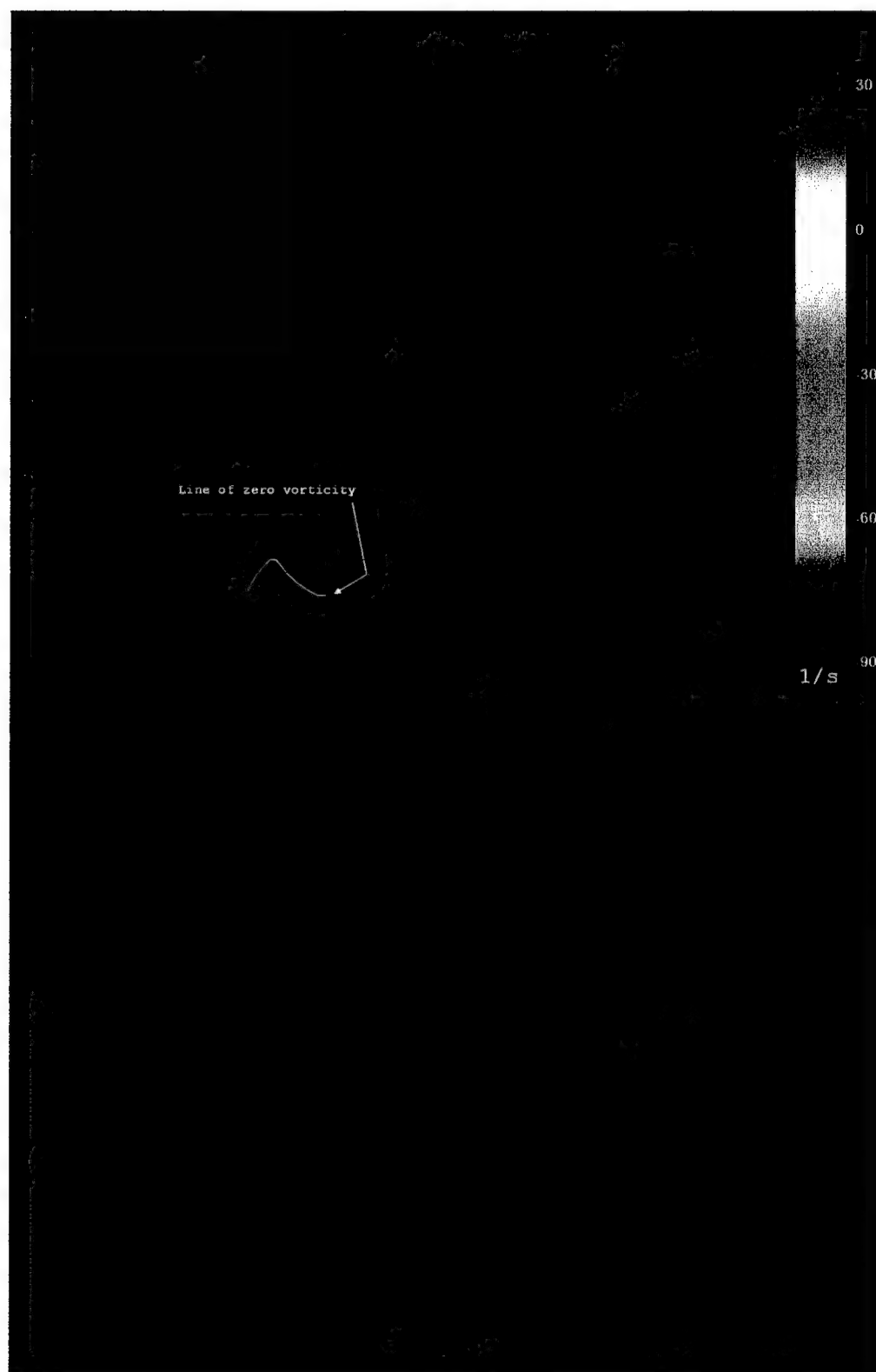


Figure 3-14: Axial vorticity contours for 20° angle of attack, cross-core plane

The vorticity contours confirm what is intuitive for a vortex with a solid-body rotational core. There is a maximum (or minimum here due to the sign convention) value of vorticity in the core of the vortex, which decreases as one travels radially outward. This concentrated vorticity is seen to be destroyed in the wake of breakdown as there is no longer a peak of vorticity in the core. The shear layer, which is initially connected to the vortex core, also has vorticity of the same sign and comparable magnitude to the vortex itself. In between the vortex core and the shear layer, a region of oppositely signed vorticity begins to develop and grow as one travels in the x-direction. This is the secondary vortex which forms either by the eruption of the boundary layer over the suction surface, or by the fluid reattaching itself, then separating again from the surface. There is, of course, a line of zero vorticity as the contours change from negative vorticity in the primary vortex to positive vorticity in the secondary vortex. The secondary vortex is weaker than the primary one as the color bar indicates the maximum value of vorticity there is about one-third that of the primary vortex for this case. Theoretically, the secondary vortex would also produce a third and smaller yet tertiary vortex, and so on, however, this investigation was not focused on this area, and thus not able to see the formation of one. As the secondary vortex grows, it is seen to come between the axial vorticity in the shear layer and that in the core of the primary vortex. Between 16% and 25% chord, the secondary vortex is seen to begin to sever the contour of vorticity between the shear layer and the vortex core. Going downstream, the secondary vortex grows and is completely between this shear layer and the solid-body core of the primary vortex. By about 33% chord, the shear layer seems to only be feeding into the outer region of the vortex. This characteristic will be commented on further in the discussion section.

An investigation of the larger chord wing at a  $25^\circ$  angle of attack and 10cm/s freestream speed showed much the same behavior, with breakdown occurring slightly more upstream at about 50% chord. The maximum azimuthal velocities obtained were also greater, indicating a stronger vortex than the previous case. A full view of this wing, along with small slices of the breakdown region, is shown in Figure 3-15.

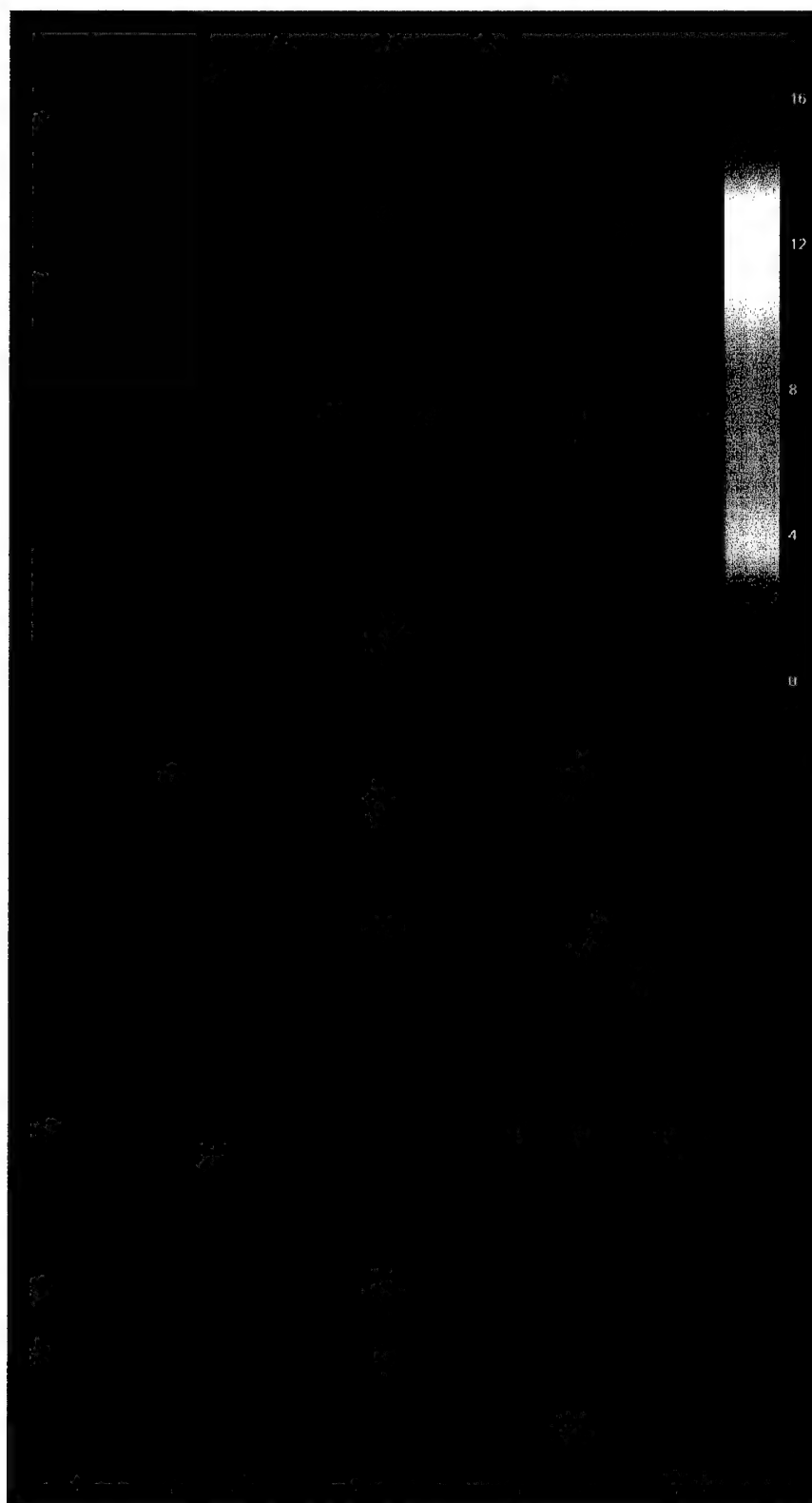


Figure 3-15: Velocity field for 25° angle of attack, cross-core plane

Figure 3-15 makes it possible to see the rapid transition from a small and tight vortex core with high velocities before breakdown, to a growing “dead” region where the average azimuthal velocities in the core have fallen to nearly zero. The whole process is seen to happen in less than 10% of the chord.

The attention of this study will now focus on the azimuthal velocities and the measurement of circulation of the LEV, and specifically the circulation of the core of the vortex. This will provide valuable insight into the nature of the vortex, and the reasons for its breakdown.

### 3.3.2 Azimuthal Velocity Determination

The cross-core plane was chosen for further investigation of the azimuthal velocity and circulation in the vortex due to its accurate representation of the LEV. Section 2.3.4 describes the method used to calculate the velocities normal and tangential to a line after the DPIV process has produced a velocity field. For this case, a horizontal line segment was drawn which passes through the center of the LEV core, and the velocity component normal to this line was taken to be the azimuthal velocity of the vortex at a given radius. Figure 3-16 shows an example vortex and the line used to calculate the said velocities.

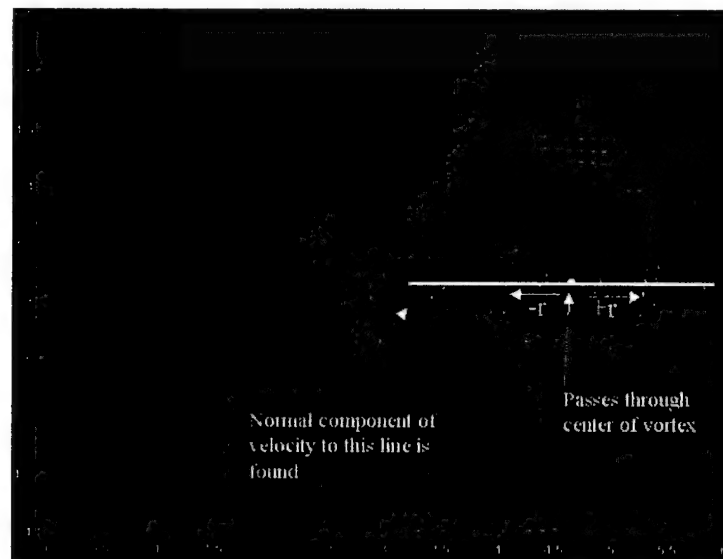


Figure 3-16: Example of line used for azimuthal velocity calculation

It should be noticed that the far left of the line passes through the shear layer which feeds into the vortex. When one moves from the shear layer on the left to the right along the line, there will initially be high normal velocity components that fall off as the line passes through the secondary vortex region. Then, the normal component will increase to its maximum before falling to zero and switching signs as it passes through the core of the vortex. This line was drawn and calculations were done at each wing chord station presented in Figure 3-13 and Figure 3-15 as well as for a 15 and 30° angle of attack. The origin of the vortex (radius = 0) was centered at the vortex core. The results of these calculations are presented in the next section.

### 3.3.3 *Azimuthal Velocity Plots*

The next four plots will show the velocity profile for the larger 45cm chord length wing at 15, 20, 25 and 30° angles of attack and a freestream speed of 10cm/s. When looking at these plots, it is advised to keep in mind that the left hand side (negative radius) includes data from the shear layer which rolls up to form the vortex. The right hand side of the plot (positive radius) gives a better picture of the actual velocity profile of the vortex itself, up to the point where it interacts with its twin from the other side of the wing. All profiles were shifted slightly to line up with each other so that their point of zero velocity was at the vortex core (radius = 0). Figure 3-17 shows these plots, which again are data for a two second average of the velocity fields.

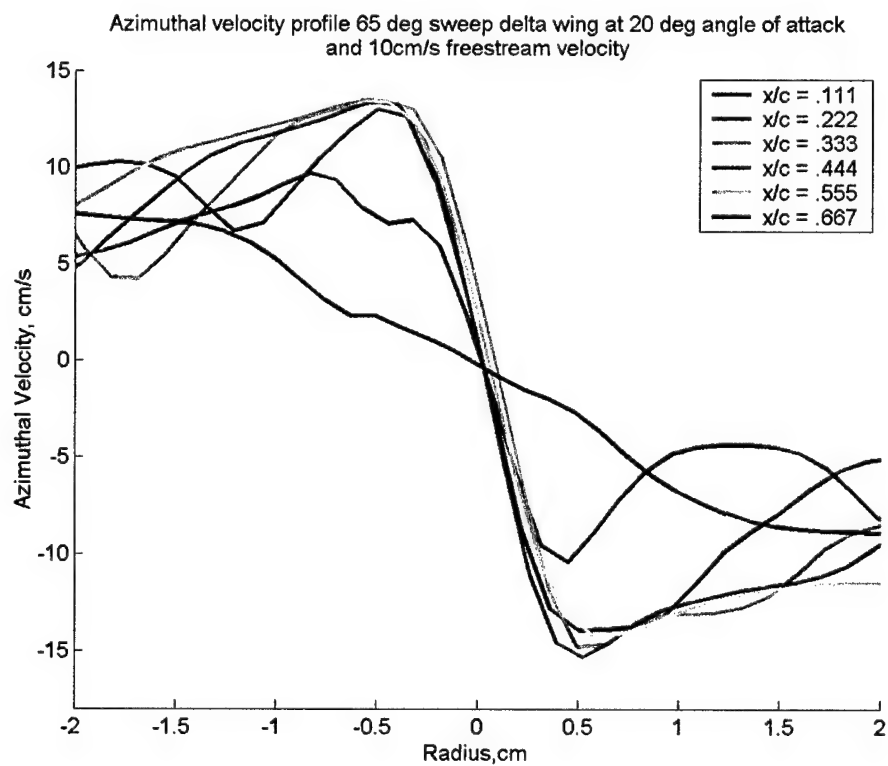
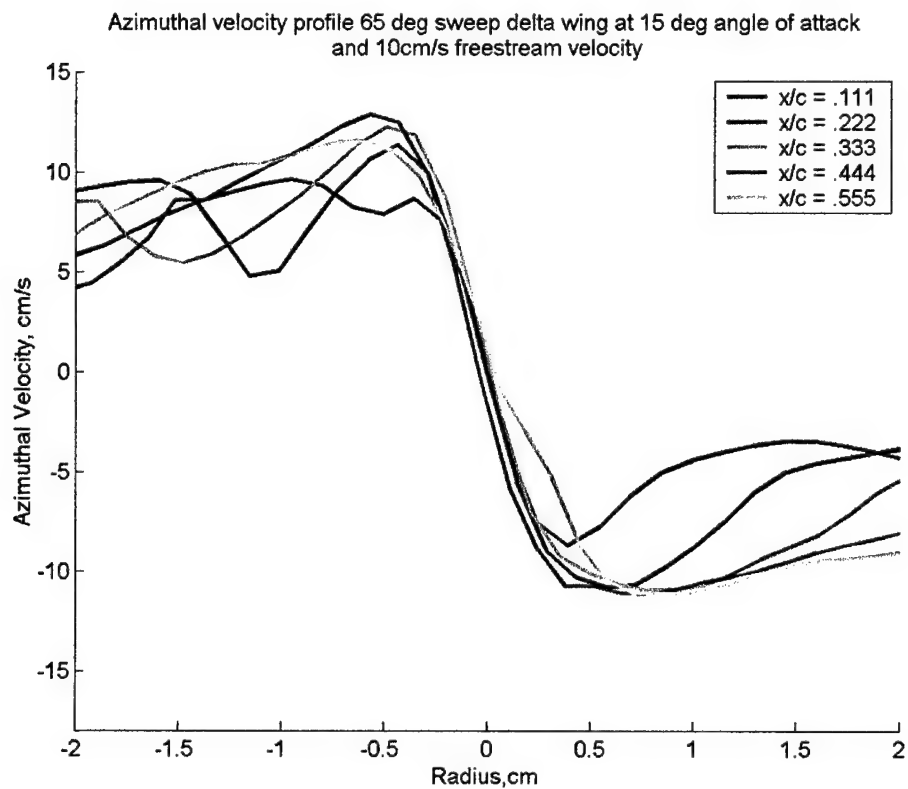


Figure 3-17: Azimuthal velocity profile for 45cm chord wing



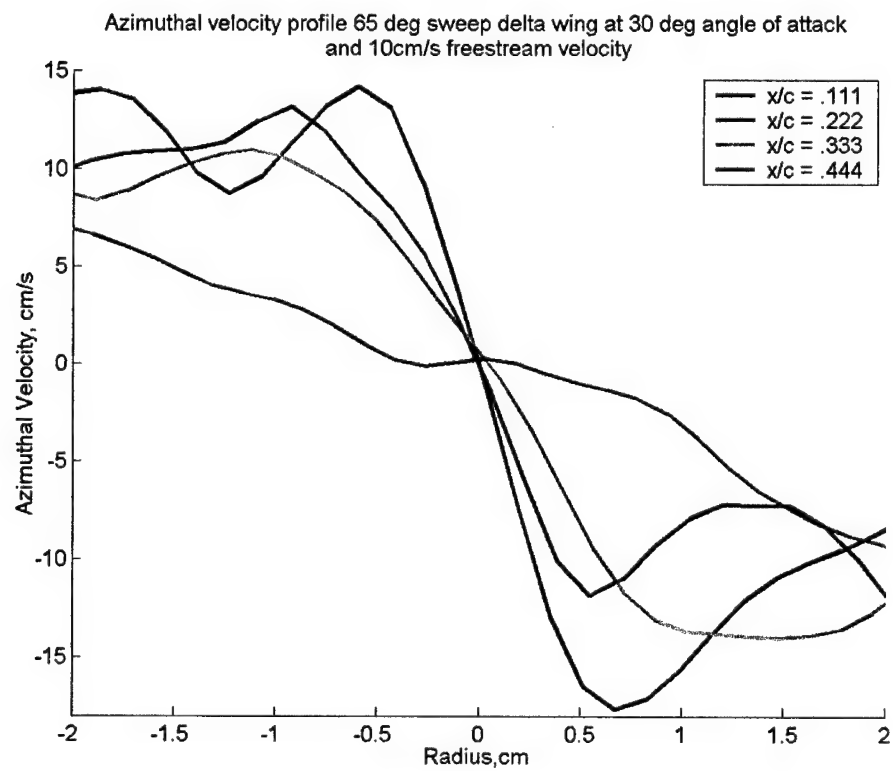
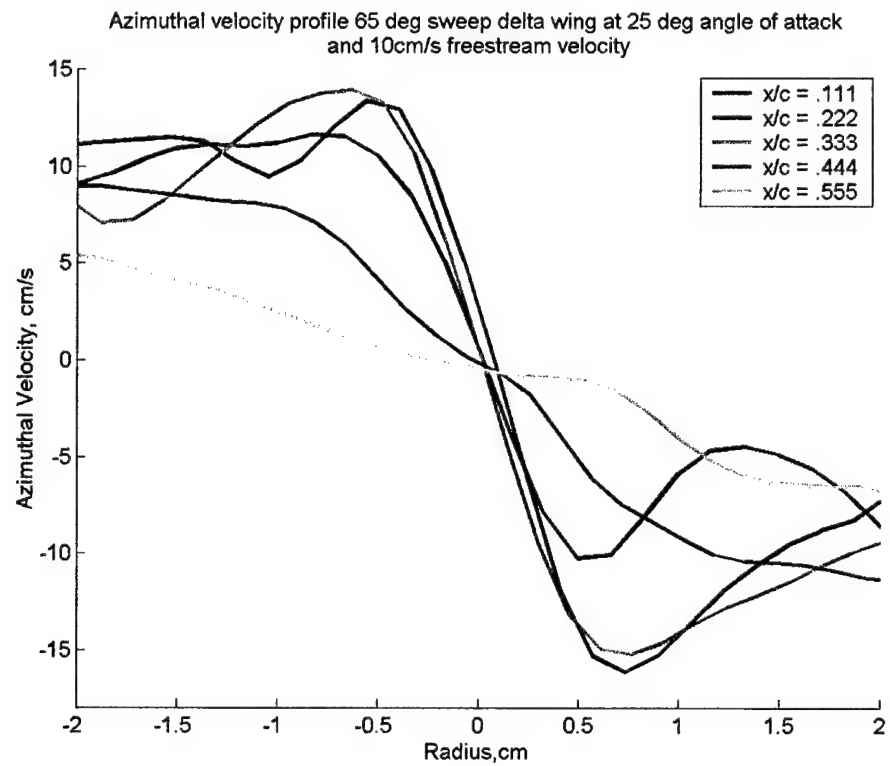


Figure 3-17 (cont.)

The solid red line in each plot, corresponding to the measurement location at about 11% chord, shows that the vortex core is not fully developed. That is, the maximum azimuthal velocity has not yet been reached at this chord location for all the angles of attack. At stations aft of this, the velocity profiles, up to the point of maximum azimuthal velocity, are nearly identical for the given angle of attack. The maximum velocity reached is between 10 and 15cm/s, just over the freestream velocity of 10cm/s. This region has been previously defined as the core of the vortex. These figures show that once fully developed, the core of the vortex remains unchanged, up to the chord location where vortex breakdown starts to occur. It can be seen that at a  $15^\circ$  angle of attack, there is no breakdown over the wing surface. The velocity profile shows a constant core, with the velocity outside of that region falling rapidly for upstream chord locations, and dropping off less rapidly for each successive chord location. This shows that the size of the outer region of the vortex is growing, as the shear layer feeds into it. This feeding, however, does not make it to the core itself. The core region for each angle of attack has about the same slope, size, and maximum velocity point for each chord location. For the  $20^\circ$  angle of attack, vortex breakdown is observed to occur between the 55% and 67% chord station. Evidence of breakdown can be seen in the velocity profile plots as the slope in the core of the vortex is much lower, and the core seems to be much more spread out. This confirms what is seen in the velocity vector fields of the post-breakdown region in Figure 3-13 and Figure 3-15. There, a dead region occurred in the core of the vortex where there was no longer a distinct solid-body rotational core.

To further illustrate this transition at breakdown, the data from the 30cm chord wing at a  $20^\circ$  angle of attack is shown in Figure 3-18. A few more chord locations were chosen for data points making the transition at breakdown easier to see. The result corresponds well with data from the larger wing. The velocity vector field for this smaller wing was shown in Figure 3-13.

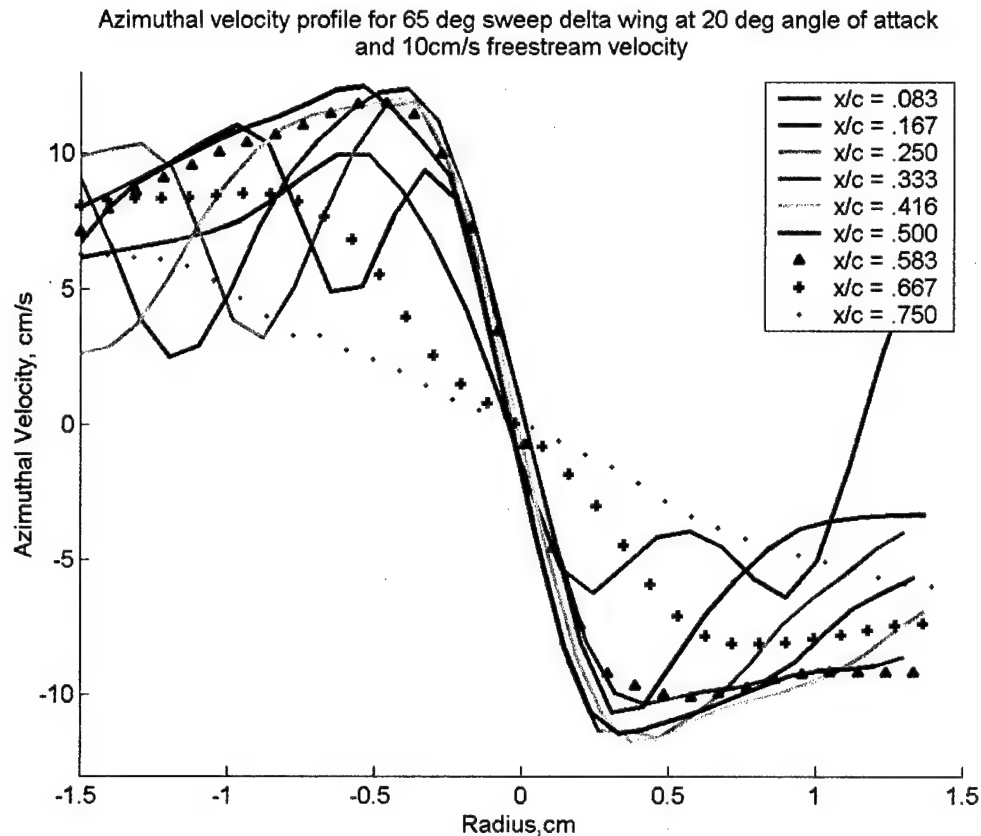


Figure 3-18: Azimuthal velocity plots for 30cm chord wing

The velocity profiles for this wing show that by about 16.7% chord, the core of the vortex is fully developed, but the outer region's velocity falls off rapidly with radius. Going downstream, the effect of the shear layer feeding into the outer region is evident as the velocity there increases, while the velocity profile of the core up to the maximum velocity point remains unchanged. This is true up to the point of breakdown which starts at about 58% chord. The core is now seen to have lower swirling velocities, and encompass a larger region. The outer region appears to remain initially unaffected as the velocity there is the same as upstream. Farther in the wake of breakdown, at about 75% chord, the outer region's swirling is also seen to drop off as the effects of breakdown spread to this region. It should also be noted that the 30cm chord wing had a core diameter of about 0.75cm, while the 45cm chord wing's core size scaled up to about 1.2cm in diameter. Faster and slower freestream velocities were also run, but the effect

was just an increase in the magnitude of the maximum azimuthal velocity. No relevant changes in the structure of the velocity profile were observed.

The azimuthal velocity profiles provide valuable insight into the core and outer region of the vortex. Next, the circulation around a circle centered at the core of the vortex will be calculated to quantify how much circulation is being fed into the vortex, and what part of the vortex it is going into.

### 3.3.4 Circulation Measurements in the Cross-core Plane

The circulation of the LEV was numerically determined using the method described in section 2.3.4. The LEVs are roughly circular in shape, so a circle was chosen as the path over which to calculate the circulation. The circulation of any real vortex will change depending on the radius of this circle. This study is concerned primarily with two measurements of circulation in the vortex: the circulation of the core of the vortex, and the maximum value of circulation achieved inside the entire vortex. This maximum value gives insight into the overall strength of the vortex. Since the azimuthal velocity of the LEVs outer region does not fall off as  $1/r$ , there will be some addition to the total circulation of the vortex from this region. The radius at which the maximum circulation of the vortex occurred was simply determined by trial and error. The circulation of the vortex was plotted versus the circle radius, and the maximum value was chosen from the graph as the one data point for that particular chord location. In general, since the azimuthal velocity falls off slower than  $1/r$ , the maximum circulation occurred at the maximum radius of the vortex. This radius ( $r_{\max}$ ) is the same as the distance from the center of the vortex core to the wing surface, since velocity vectors occurring artificially below the wing surface were ignored.

A few past studies have measured the circulation of the LEVs such as Visser and Nelson (*ref. 20*) and Moreira and Johari (*ref. 21*). The total strength of the circulation of the vortex has also been proposed as a reason for vortex breakdown (*ref. 22*), meaning there exists a certain threshold value of circulation, above which the vortex breaks down. The results below suggest otherwise.

Moreira and Johari have made the observation that total circulation increases approximately linearly with chord location prior to the vortex breakdown location (*ref.* 21). They used an ultrasound method to investigate different delta wing sweeps at angles of attack similar to the present study.

For this study, the LEV circulation was in general found to increase linearly with freestream speed. It is common practice for the circulation to be normalized by the freestream speed and the wing root chord length to make it a non-dimensional number for comparison, which was done in the following figures. Figure 3-19 shows the composite data for the maximum circulation of the LEV at different chord locations and for four different angles of attack. It should be noted that the absolute value of circulation is shown, since by convention the circulation of the vortex shown in the velocity vector fields above would be negative. The circulation is indeed seen to increase linearly with the wing chord up to the location of vortex breakdown. After that, a non-linear trend can be seen as the circulation tends to level off. The observed breakdown location is noted on each curve. It should again be noted that for an angle of attack of  $15^\circ$ , breakdown did not occur over the wing surface, so its position is not shown here.

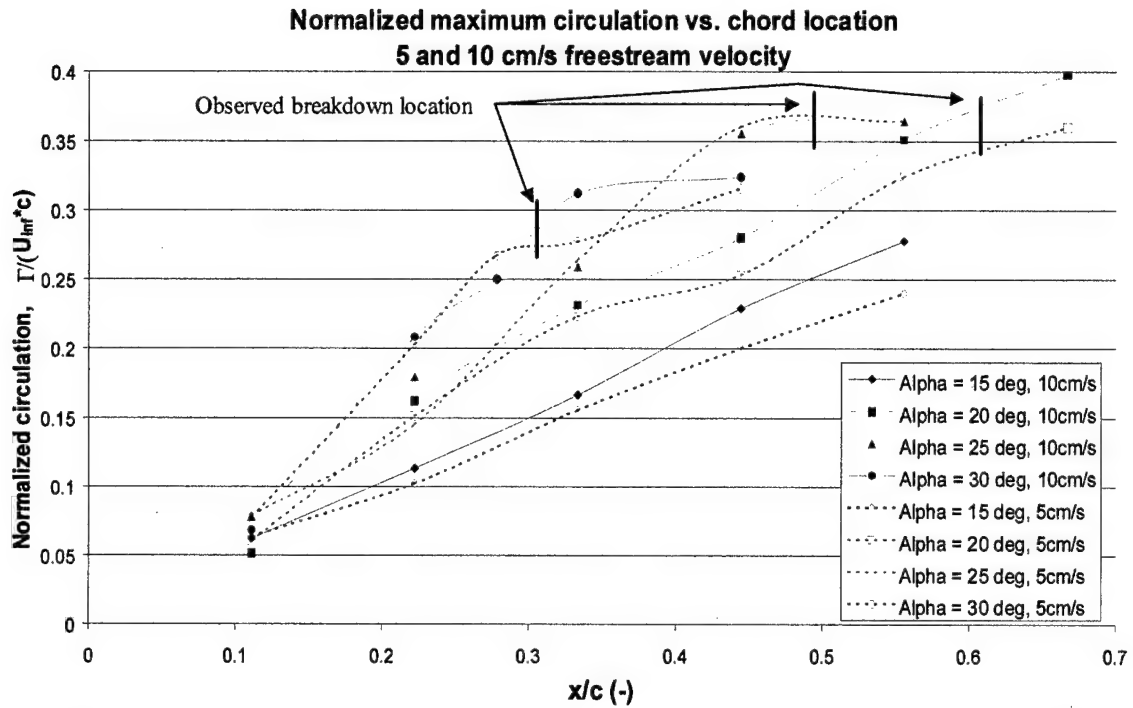


Figure 3-19: LEV maximum circulation vs. chord location for various angles of attack

The radius corresponding to the maximum circulation value for each angle of attack and each chord location is shown next in Table 3-1 for reference.

Table 3-1: Radius of maximum circulation ( $r_{\max}$ ) vs.  $x/c$  for all angle of attacks tested

$r_{\max}$ vs. $x/c$	$\alpha = 15^\circ$	$\alpha = 20^\circ$	$\alpha = 25^\circ$	$\alpha = 30^\circ$
$x/c = .111$	0.6 (cm)	0.6	0.7	0.6
$x/c = .222$	0.9	1.0	1.0	1.1
$x/c = .333$	1.3	1.4	1.5	1.7
$x/c = .444$	1.6	1.8	2.2	2.2
$x/c = .555$	2.0	2.4	2.7	
$x/c = .666$		3.2		

It becomes clear now that circulation does increase approximately linearly with chord location, and that a higher angle of attack leads to a faster rate of increase of this circulation. By observation of the curves for the 20 and 25° angles of attack in Figure 3-19 it is seen that vortex breakdown happens at nearly the same value of normalized

circulation. This would lend support to the idea of some limiting value of circulation, above which the vortex breaks down. However, an increase to a  $30^\circ$  angle of attack shows that breakdown happens at a station where the normalized circulation is considerably lower than the previous two. This suggests that there is no real limiting value of total circulation in the vortex which causes vortex breakdown. Another argument against a limiting value of circulation is that the maximum circulation values plotted above occur at a radius which is near the outside edge of the vortex, relatively far away from the vortex core. From the velocity vector fields, it was seen that breakdown first happens in the core, and that its effects eventually spread to the outer region. Since the core is the region where breakdown first occurs, the circulation and strength of this region should be of primary concern. This will be discussed further in the discussion section.

Previously it was shown that the azimuthal velocity profile for the core of the vortex from the point where it is fully developed to just prior to breakdown is nearly constant. The measurement of the circulation about the core will support this claim. From the velocity plots, it can be seen that the core for this particular wing has about a 0.6cm radius. Figure 3-20 shows the circulation calculated about a circle of this radius for all the chord locations. As expected, the circulation rises from the wing tip to just aft of the first station (11% chord). After that it remains constant until just prior to vortex breakdown, where there is a rapid decrease in core circulation. This result makes intuitive sense since it was seen from the azimuthal velocity profile plots before that in the immediate post-breakdown region, there is a dead zone in the core where the azimuthal velocities, and hence the circulation in the core, is much less than upstream of breakdown.

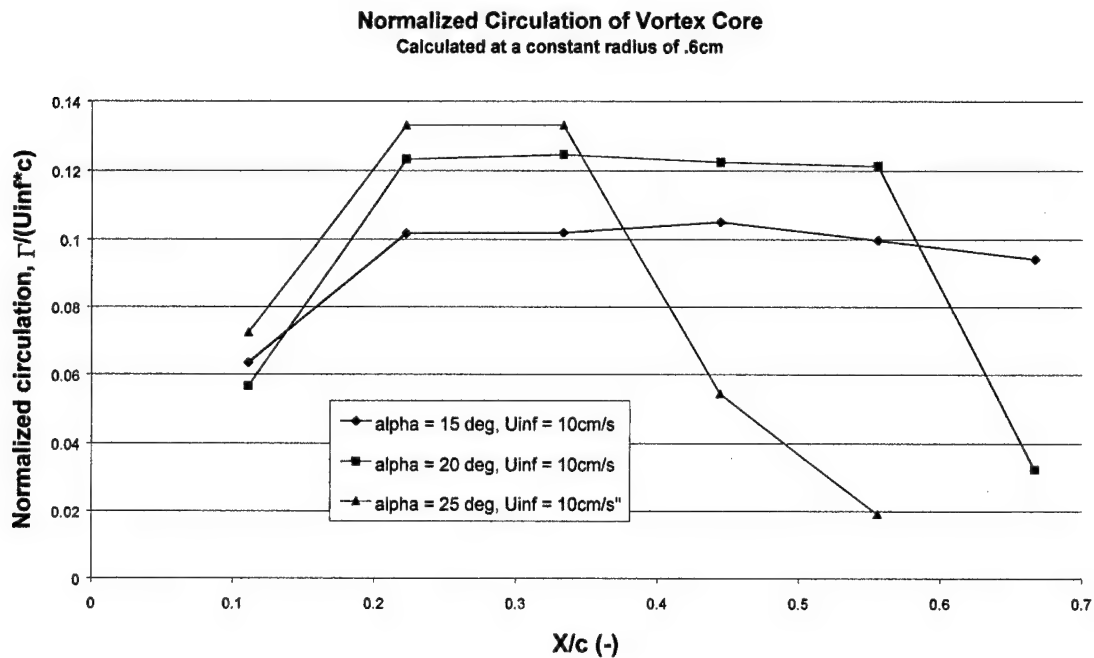


Figure 3-20: Circulation inside the LEV core

The existence of a constant velocity, solid-body rotational core from the point of formation to just prior to vortex breakdown leads to the conclusion that, at least to first order, there is no feeding of vorticity or circulation into the core of the vortex once it is formed. This finding is thought to be new and significant in that it differs greatly from the idea that delta wing flow is mostly conical. This will be expanded on in the discussion section.

### 3.4 Dye Visualization Experimental Results

After completing the DPIV investigation of the vortex core, cross-stream, and cross-core planes, it was decided that it would be beneficial to obtain dye visualization data to reinforce the idea of a constant rotational LEV core. It was also hoped that a picture of breakdown of the vortex core with relatively undisturbed flow outside of the core could be obtained. To do this, red dye was injected at the tip of the wing such that it entered the center of the LEV core. Then, blue dye was injected at different locations near the wing leading edge, but farther aft of the tip to illustrate how the fluid that is initially in the shear layer feeds into the core or the outer region of the vortex.



Figure 3-21 shows first the delta wing at a  $15^\circ$  angle of attack and a freestream speed of 5cm/s with dye just injected into the core (A). Breakdown is seen to just start to form in the near wake. Next, blue dye is added just off center so that it can be seen swirling around the core (B). Then, the blue dye probe is moved farther aft so that it enters the LEV at an even larger radius (C).

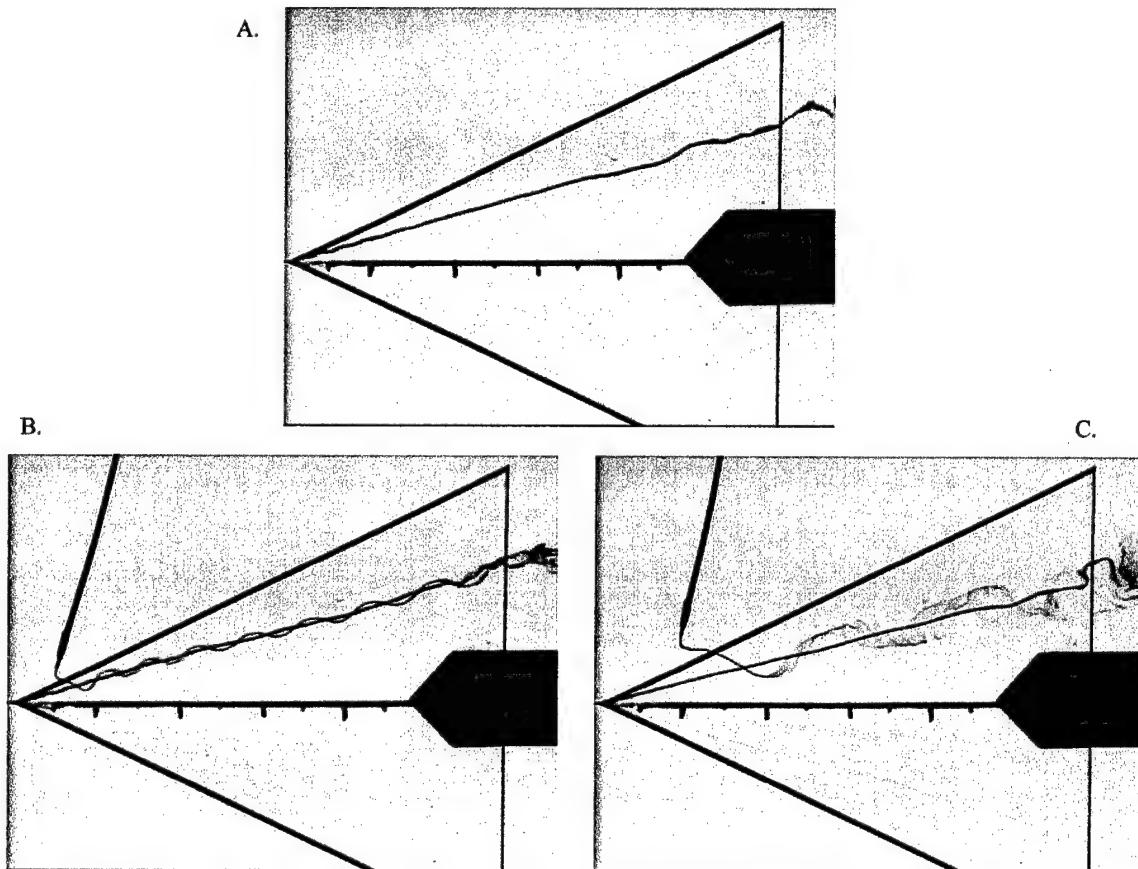


Figure 3-21: Dye visualization of  $65^\circ$  sweep delta wing at  $15^\circ$  angle of attack

As can be seen in frame B, the blue dye forms a nearly constant period sine wave shape. This shape is due to the ratio of the azimuthal velocity to the axial velocity of the vortex core,  $u_\theta / u_z$ , commonly referred to as the swirl number. Figure 3-3 showed that for a  $15^\circ$  angle of attack, the axial velocity along the core was nearly constant and unchanging along the chord. This would then suggest that the azimuthal velocity at the radius where the blue dye is injected is constant along the length of the wing. Also, frame B and C suggest that the fluid stays near the radius where it enters the vortex. If the flow were conical, it would be expected that this dye would diverge and end up at a larger radius

than where it started. This dye visualization further supports the idea that the flow is not conical, and that the LEV has a constant core.

Increasing the angle of attack to  $30^\circ$ , the breakdown location moves up the wing chord. The red dye is again injected into the core and marks the breakdown location. As the blue dye is injected farther and farther away from the core, there is less immediate interaction between the blue dye and the vortex breakdown region. Figure 3-22 shows this.

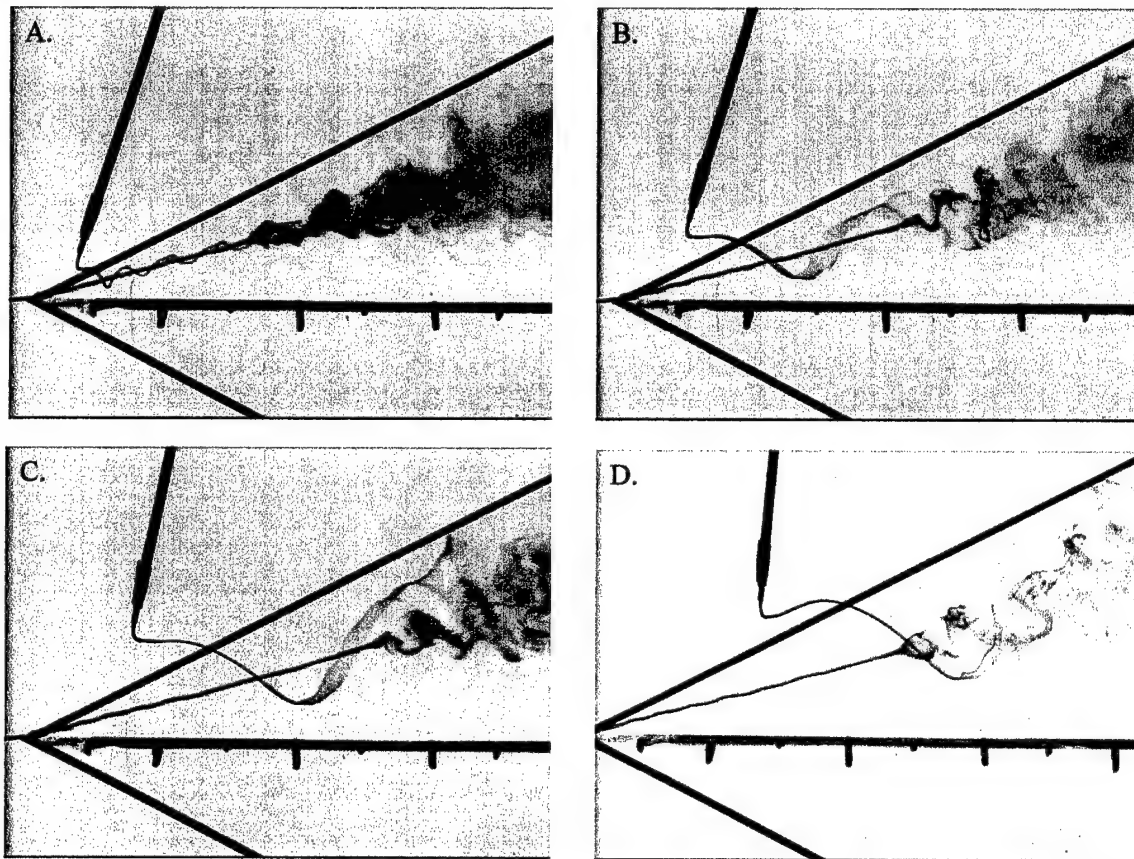


Figure 3-22: Dye visualization of  $65^\circ$  sweep delta wing at  $30^\circ$  angle of attack

Frame D shows blue dye that is injected at such a radius that it completes nearly one full revolution before it is drawn into the turbulent wake of the vortex breakdown. This provides further evidence that the flow outside of the breakdown region remains initially unaffected by breakdown of the core. The same evidence was presented by Sarpkaya (*ref. 23*) in which the flow around the core of the vortex in swirling pipe flow remained unaffected (Figure 3-23).

Frame A in Figure 3-22 shows the period of the aforementioned sine wave made by the blue dye to increase in the downstream direction. Referring back to Figure 3-3 again, the axial velocity for this angle of attack is seen to increase rapidly from the apex and then fall to zero at breakdown. The observed stretching of the sine wave suggests a decrease in the swirl number. This is due to the fact that the axial velocity is increasing, while the azimuthal velocity remains unchanged. This fact lends further support to the idea of a constant vortex core.

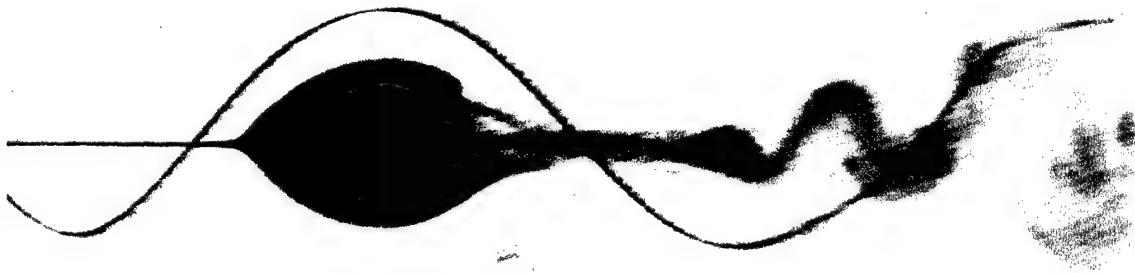


Figure 3-23: Dye visualization of breakdown in pipe flow (*ref. 23*)

## 4 Numerical simulation results

Up to this point, the self-induction theory of vortex breakdown and the vortex filament method have explained and simulated the transient formation of vortex breakdown with a high degree of success. However, a large gap remains to be filled in that none of the cases run by Cain (*ref. 2*) have reached any form of a steady state solution in which there is a stationary vortex breakdown location. This is an unsatisfactory aspect of the foregoing simulation because all vortex breakdowns attain some equilibrium stage if the upstream flow conditions are steady. Also, there has not been any proof offered that shows the numbers used in the previous simulations actually represent any type of real physical flow situation, whether it be in a pipe or above a delta wing. This section will offer proof of the simulation representing an actual possible flow condition, and will also offer one possible solution for making the simulation reach a steady state.

### 4.1 *Analysis of Simulation Used by Cain*

A quick analysis of the baseline case used by Cain will be first done to see where the simulation needs to be modified in order to further the self-induction theory.

#### 4.1.1 *Analysis of Simulation Input Parameters*

As mentioned before, the study by Cain offered no proof that the parameters used, specifically the swirl distribution and the circulation values, actually reasonably represent any flow condition where vortex breakdown is likely to exist. He recognized that his was a qualitative study, and more work was needed to quantify the results. It is yet unknown if the numbers are even the right order of magnitude for some possible flow condition. One way to prove that these numbers are reasonable is to measure the actual flow properties upstream of vortex breakdown on a delta wing, and use those numbers as input parameters to the simulation in order to see if all the elements of vortex breakdown described by Cain are still evident. This was done in one of the early DPIV investigations using data from the cross-stream plane. The 65° sweep delta wing was set at a 30° angle of attack in 8.5 cm/s flow and the velocity field at 50% chord, slightly

upstream of vortex breakdown, was measured using the techniques described in section 2.3.4. It was observed that the core diameter of the vortex for this particular wing was about 1cm. Cain uses units of length that are not any specific unit, however, the diameter of the vortex filament tube in his simulation is 1. This being the case, centimeters were chosen to be the unit of reference. This greatly simplified the problem as the total circulation of the vortex,  $C$ , could then be adjusted without having to resize or redistribute the vorticity in the core. The azimuthal velocity of the vortex in the simulation is defined based on  $C$  and  $b$  as

$$u_{\theta} = \frac{C(1 - e^{-br^2})}{2\pi r} \quad (4-1)$$

where  $C$  is the circulation of the vortex,  $r$  is the radius from the center, and  $b$  is set to 10.9 to represent unbounded swirling flow based on past experimentation (Nakamura, *ref.* 24). Using this equation, the real azimuthal velocity profile from DPIV was plotted versus the assigned profile for different values of  $C$ . It was found that for this particular case, a final  $C$  value of 20 cm<sup>2</sup>/s allowed for the real and assigned velocity profiles to closely match. Figure 4-1 shows how the two profiles relate.

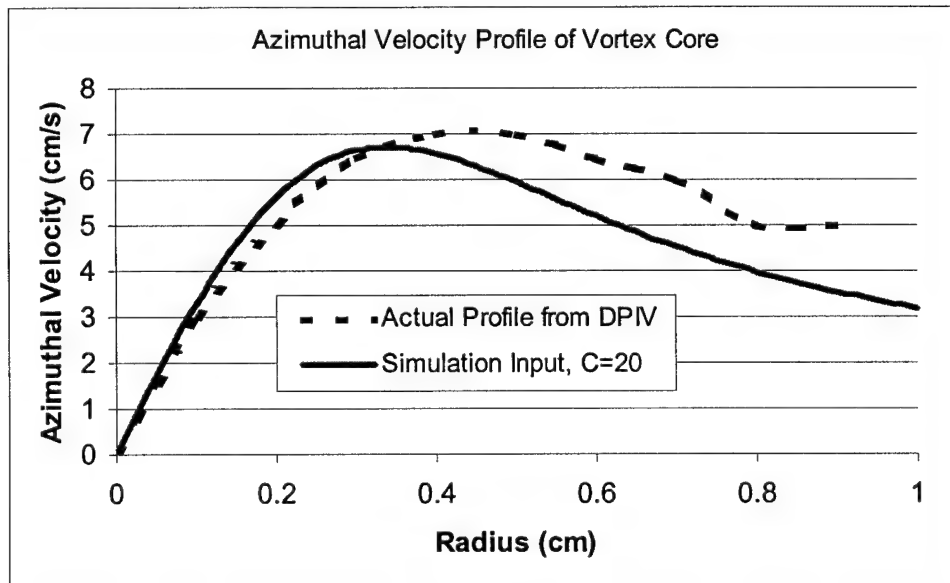


Figure 4-1: Real and simulation input azimuthal velocity profile comparison

Knowing the approximate circulation distribution and axial velocity of some real vortex, these parameters were input into the exact code used by Cain. The final  $C$  value was set

to 20, and the freestream velocity was set to 8.5. It should be noted that these values are not far off of the final numbers used by Cain when analyzing his results. The circulation of the vortex tube emanating from the vorticity source ( $z = 0$  plane) is shown in Figure 4-2 as a function of time.

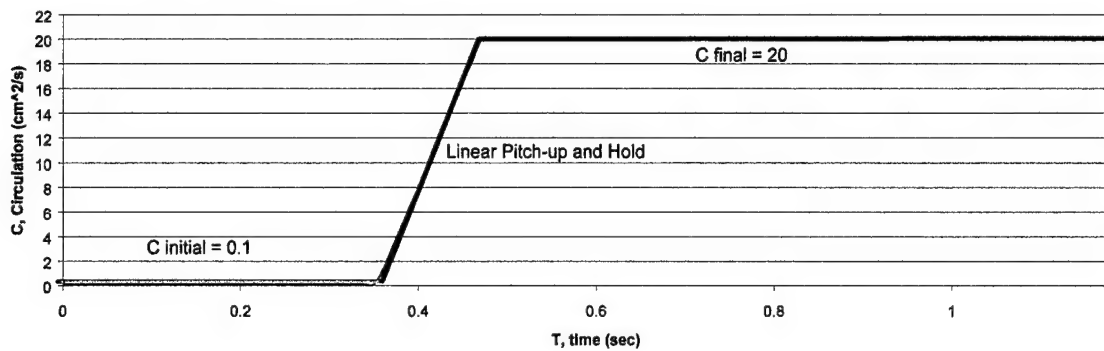


Figure 4-2: Circulation of vortex tube from the  $z = 0$  plane vs. time

A time history of the vortex tube as it convects downstream from its source is shown next in Figure 4-3. A surface plot of the filaments initially located at  $r = .12$  is used to see the motion. Just as Cain used, the blue shaded regions have low circulation, the green shaded regions have the final high value of circulation, and the red region in between is the linear ramp area where the circulation is changing due to the superposition of the vortex lines. The radial spokes are not shown here, but were included in the simulation calculation. It should be noted that the initial pile-up, radial expansion, azimuthal vorticity sign switch, and turning point are all visible in this simulation. The actual turning point happens in less time due to the higher value of circulation used (20 vs. 15 in the previous study). Since the numbers in this simulation and Cain's are very close, it is reasonable to conclude that his optimized parameters could in fact be a realistic flow situation where breakdown would occur. This leads to the conclusion that the parameters used in Cain's study which he called the optimized parameters are physically reasonable, and that the self-induction caused by the vorticity gradient of a real sample flow is enough to begin the process of transient vortex breakdown.

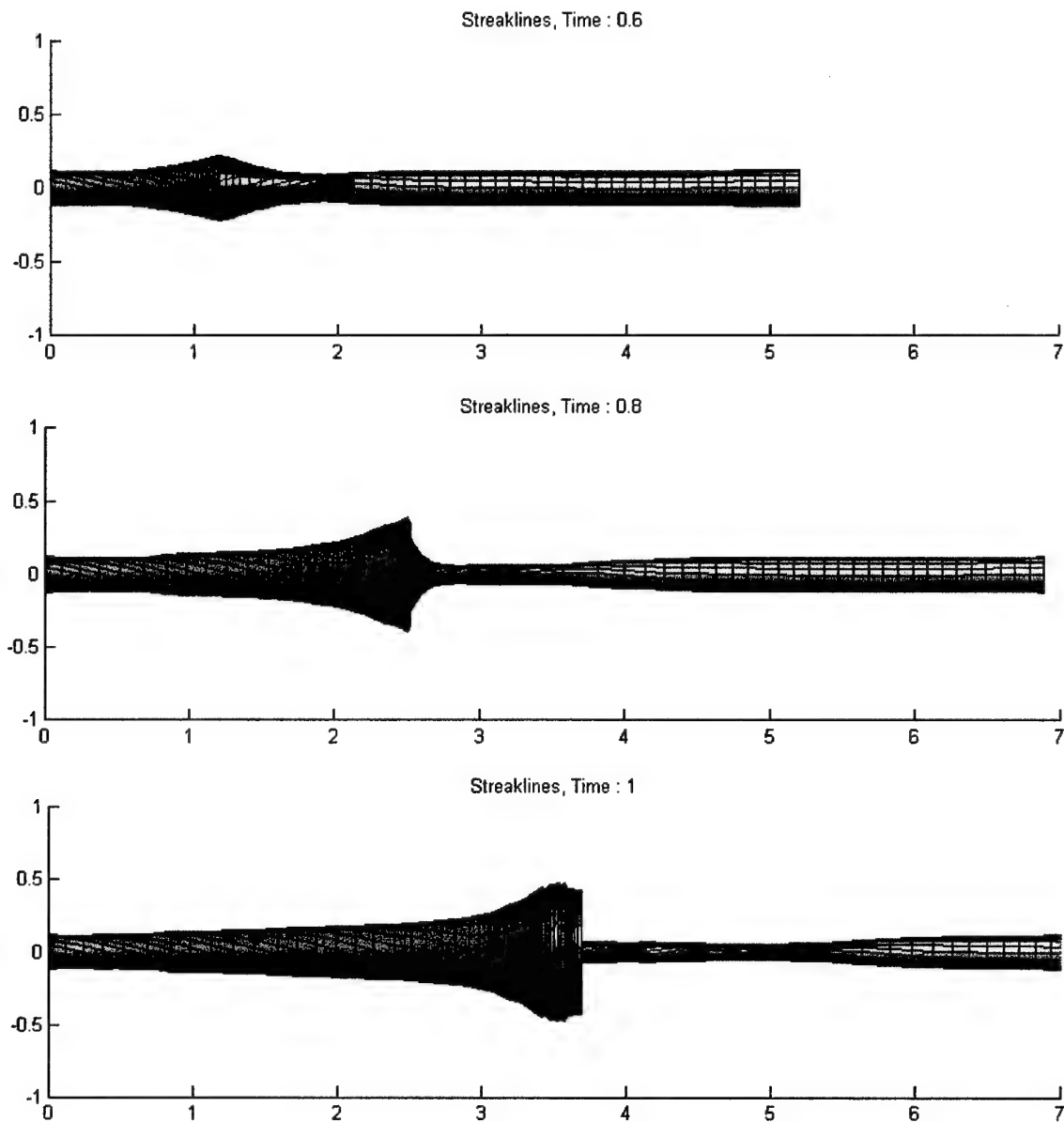


Figure 4-3: Streaklines resulting from experimental values being used as input parameters,  $C = 20$ ,  $U_{\infty} = 8.5$

#### 4.1.2 Problems Arriving at a Steady Breakdown Location

While Cain's simulation gave great insight into the transient formation of vortex breakdown, there remains the problem of making the simulation settle on a steady vortex breakdown position. In flow where breakdown occurs, such as rotating fluid in a pipe or over a delta wing, the stagnation point along the vortex axis characteristic of breakdown

does not continually travel downstream, but settles into some mean location. This will be called steady vortex breakdown. In actuality, the flow is by no means truly steady, especially in the wake of the breakdown. However, the mean position of the breakdown bubble does reach a steady state. Cain's code in its present form is unable to simulate this. This can be demonstrated by simply letting the simulation run for a longer period of time and attempting to observe some steady condition. The Figure 4-4 will show the results starting from a time of 1.8 and ending at 3.4. The inputs are exactly the same as used by Cain ( $C = 15$ ), and the freestream or convective velocity is set at 5. The formerly green filaments representing the final value of circulation are now rendered transparent so that the inside of the bubble can be seen from this head on view.

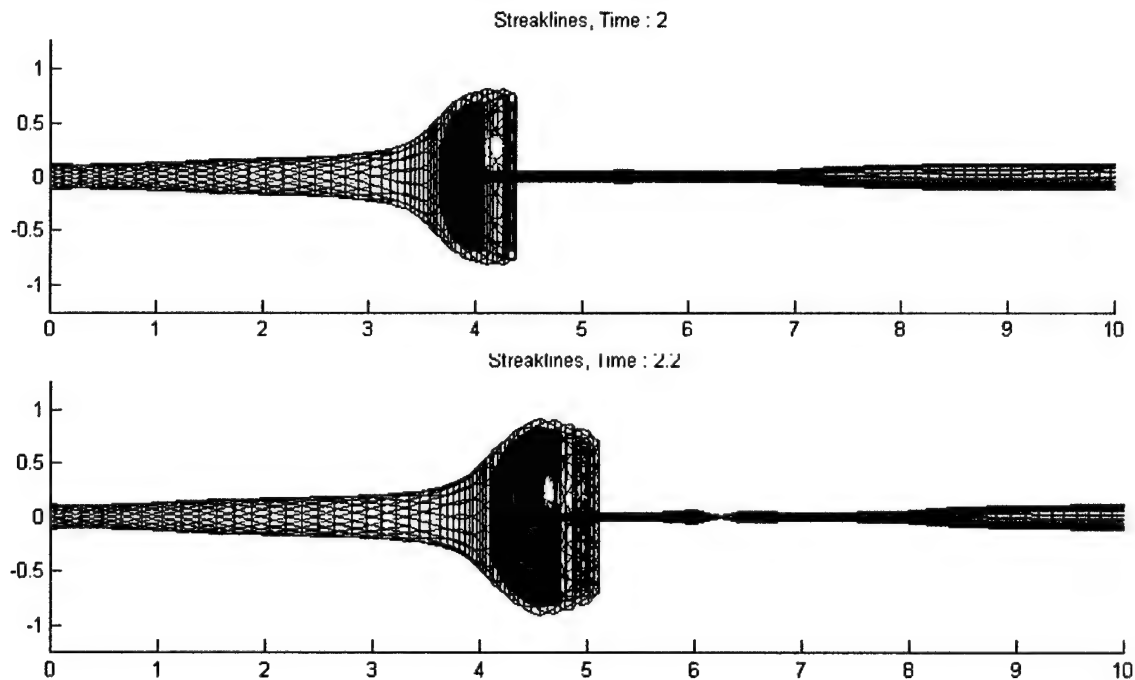


Figure 4-4: Extended time evolution of vortex filaments from Cain



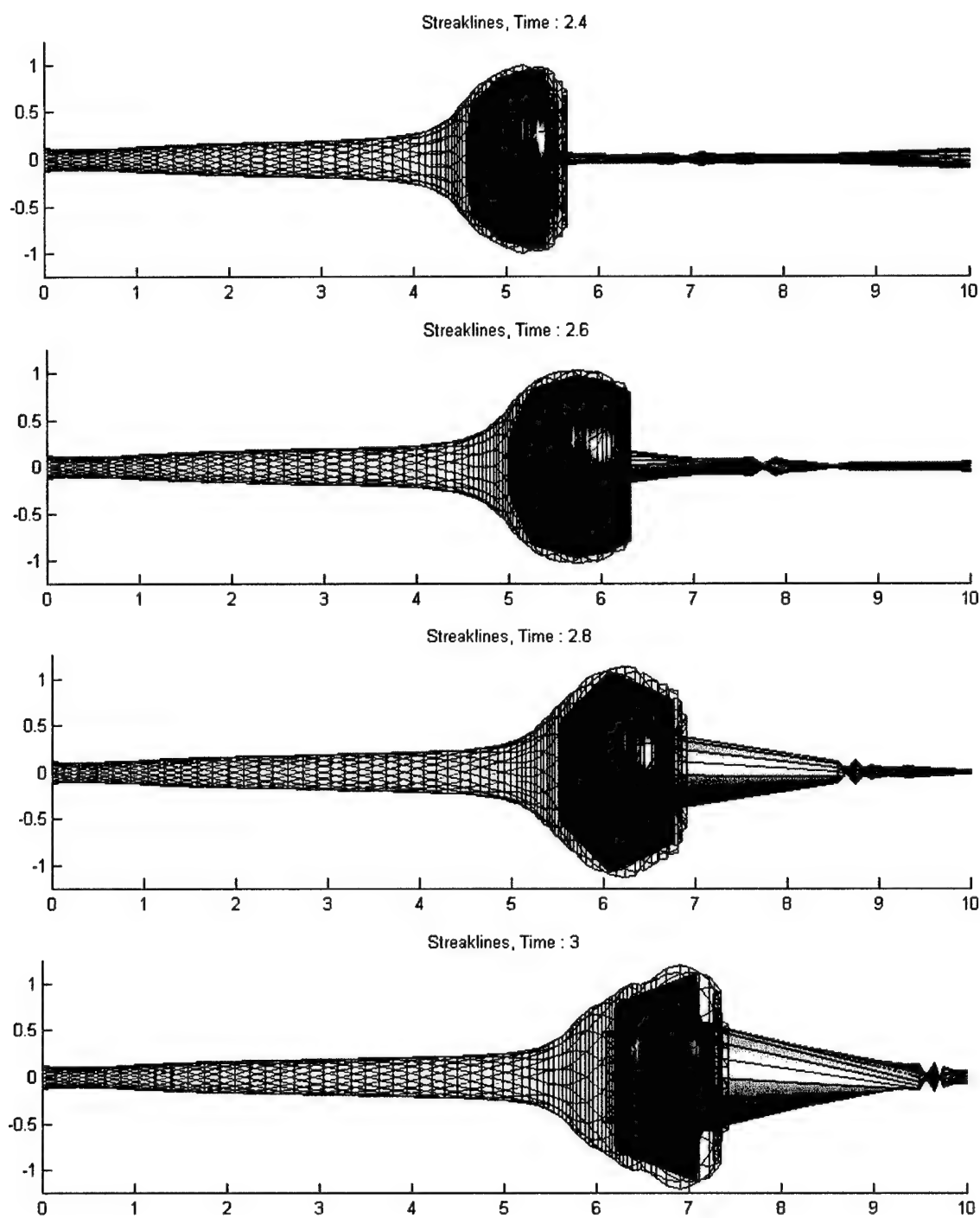


Figure 4-4 (cont.)

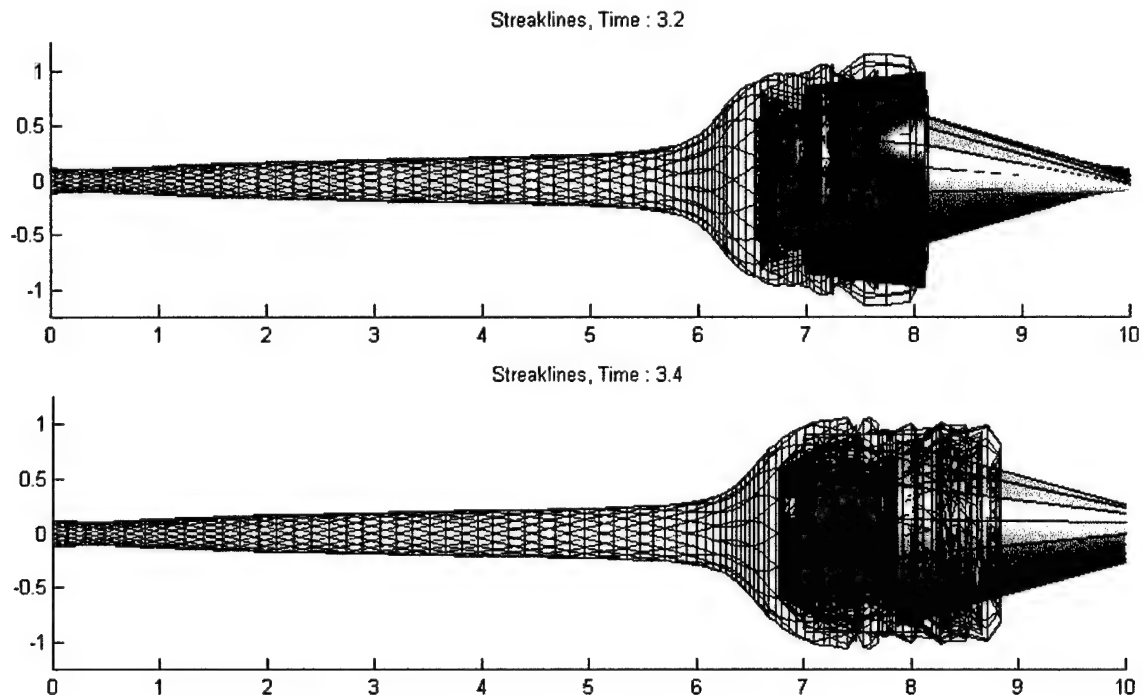


Figure 4-4 (cont.)

It should be noticed in the above figure that from the first frame to the last, the breakdown bubble continually moves downstream. There is no stationary position into which it settles. Also, inside the bubble there is a seemingly garbled accumulation of filaments making interpretation difficult. The distances between the filaments become very small, making the induced velocities on each other very large. This simulation is robust enough to handle distances between two filaments approaching zero, however the accuracy is questionable. While there does exist an instantaneous stagnation point on the vortex axis, it quickly convects downstream and the breakdown location becomes difficult to define. It should be remembered that this is an inviscid simulation, so the normal smoothing effects of viscosity are not included. This result points out the problem that this code in its current form needs modification in order to arrive at a steady vortex breakdown position.

## 4.2 *From Transient to Steady State Breakdown*

### 4.2.1 *Convective Velocity Gradient*

A first attempt at making the simulation able to represent a steady vortex breakdown was the addition of a spatially varying convective velocity. The previous study always had the axial velocity at which the filaments emerge from the vorticity source at  $z = 0$  and convect downstream set to a constant value everywhere. The change here is to make the filaments at the vorticity source convect at a high velocity, and then slow as their  $z$ -position increases. This is done by simply making the convective velocity assigned to each filament a function of the axial distance,  $z$ . In theory, this is modeling an adverse pressure gradient which is a common ingredient for vortex breakdown. The decreasing convective velocity makes it more likely that a stagnation point will form on the axis, and the breakdown bubble will remain in one position. The goal is to see the bubble structure form and stay in one position, while the fluid represented by the vortex filaments pass through it and then convect downstream. An example of this type of profile would be a diverging pipe, such as that used by Sarpkaya (*ref. 23*), where the axial velocity of the fluid is decreasing along the length of the pipe. The axial fluid velocity over a delta wing also reaches a maximum near the vorticity source or tip, and then falls rapidly towards the trailing edge as was shown in section 3.1. This measured axial velocity profile over a delta wing is a steady state condition. It is difficult to then separate out what part of that profile is due the convection of the fluid due to the pressure gradients that exist just like on a conventional wing at a high angle of attack, and what part is due to vortex induction. This then makes the task of deciding what kind of convective axial velocity profile to put into the simulation very difficult. Some experimentation was done before arriving at the presented solution. The plots here are for a prescribed convective axial velocity that starts out with a value of 5, and then drops linearly to half its value, 2.5, by a  $z$ -position of 5. The axial velocity then remains at 2.5 for every  $z$ -position greater than 5. This profile is shown in Figure 4-5, and the result is Figure 4-6. The axisymmetric property of the vortex tube was retained for simplicity.

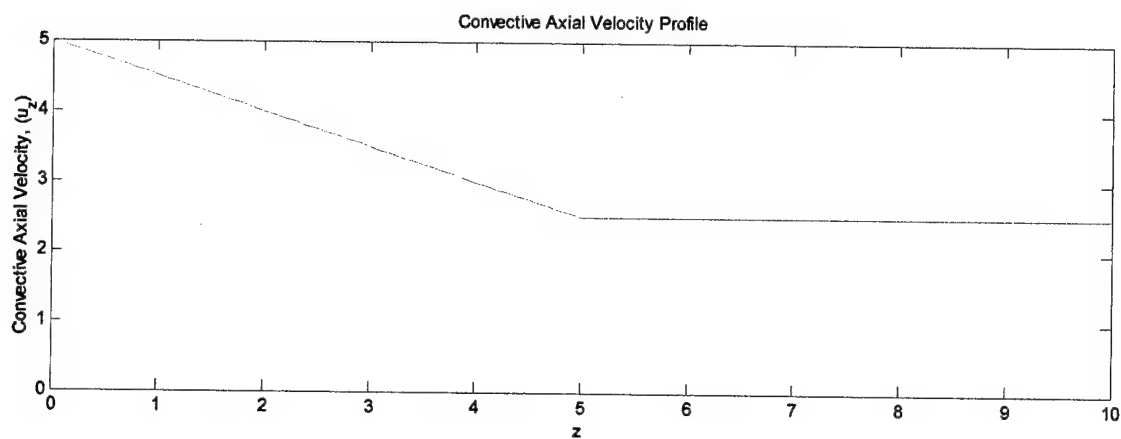


Figure 4-5: Assigned convective axial velocity profile for simulation in Figure 4-6

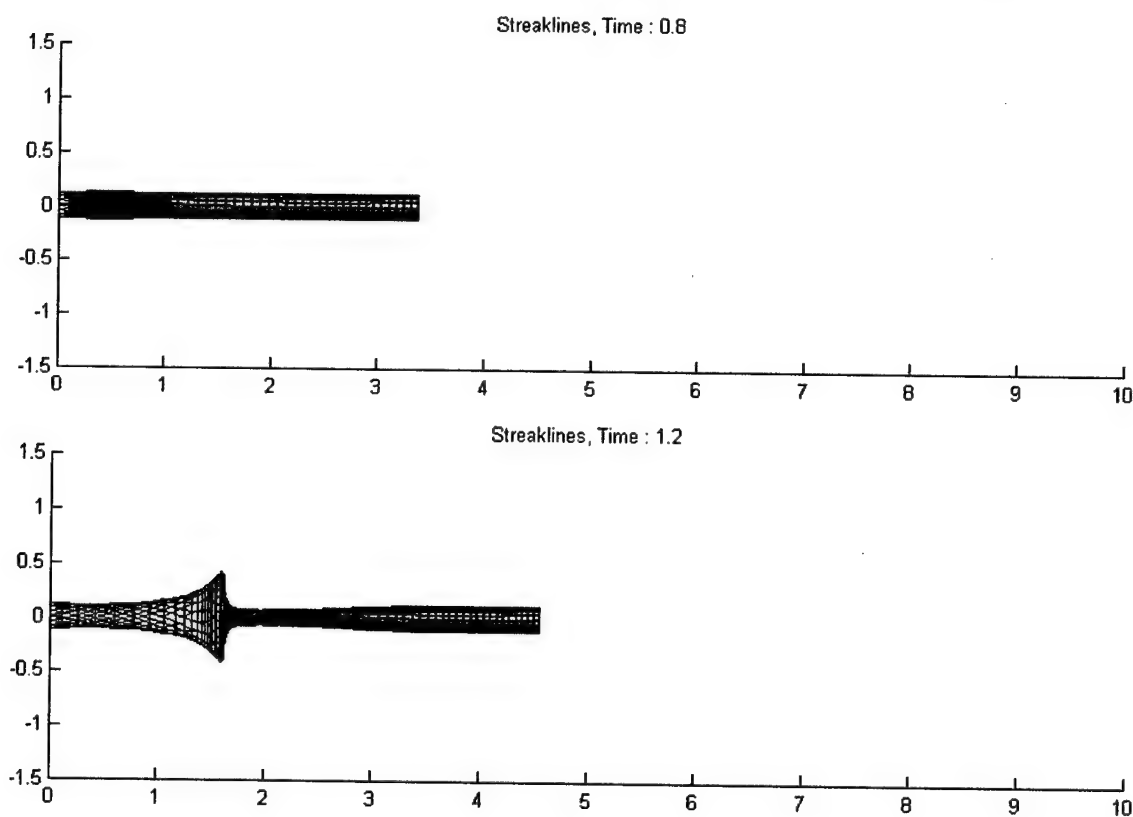


Figure 4-6: Simulation results with convective velocity gradient

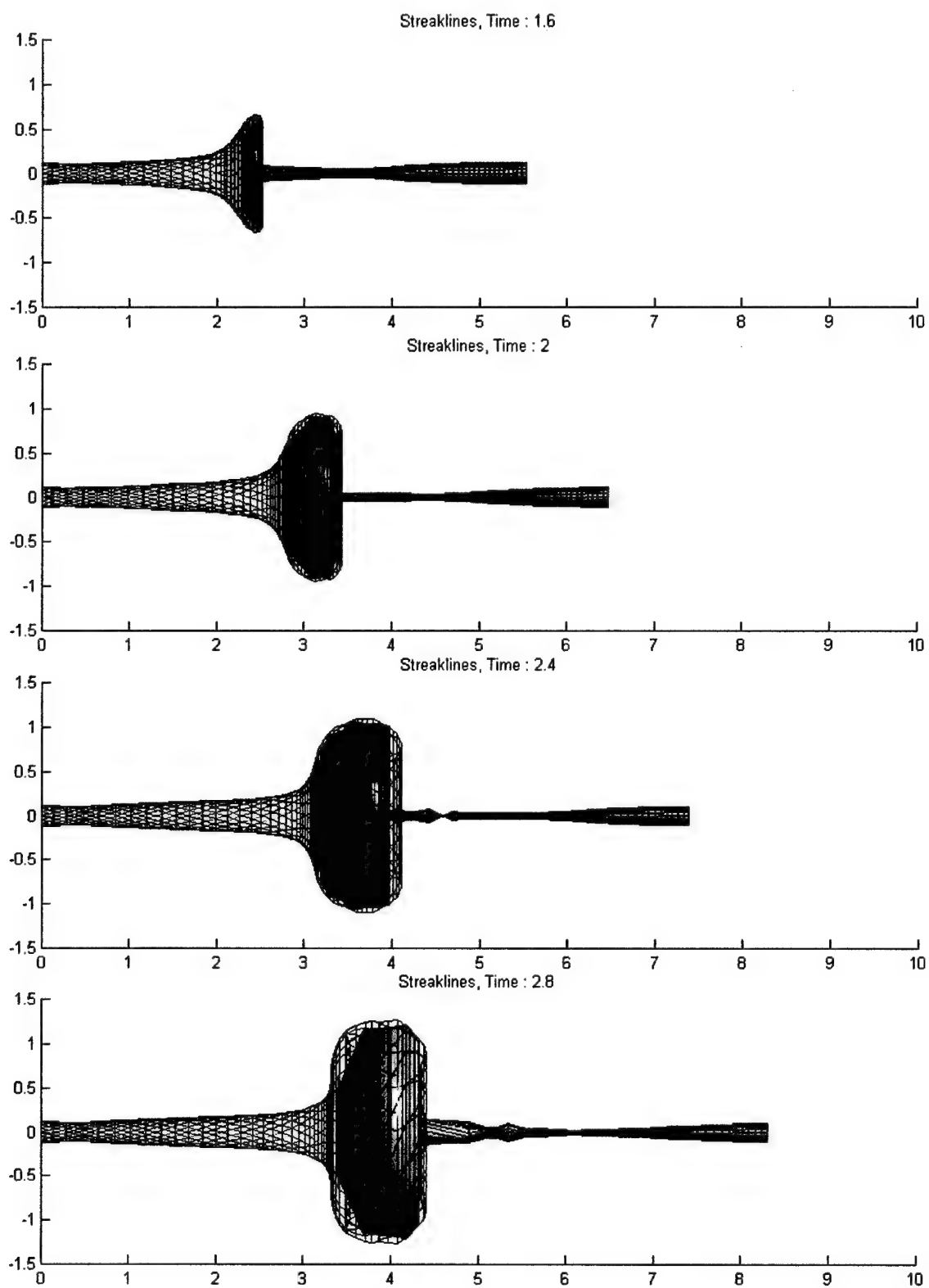


Figure 4-6 (cont.)

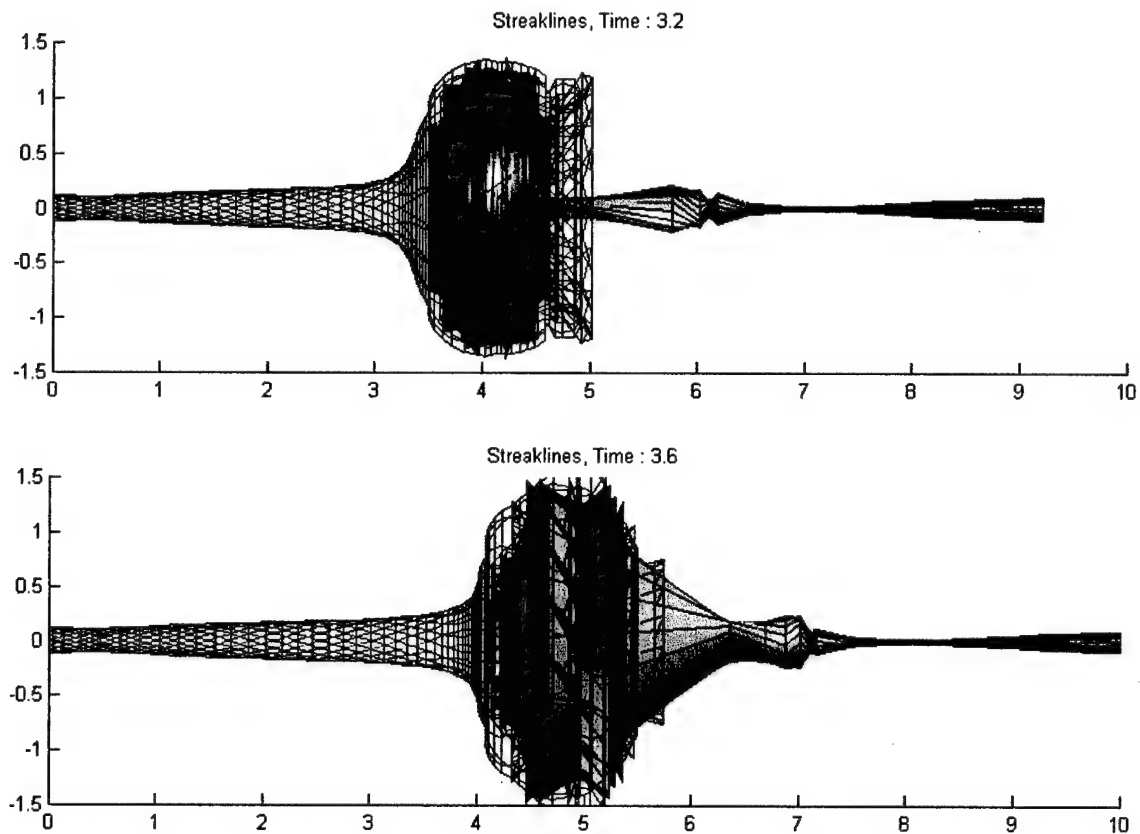


Figure 4-6 (cont.)

One puzzling feature of this simulation is the seemingly sudden change from red to blue colored filaments inside the clear bubble region between times of 2.4 and 2.8. Looking at smaller time steps of this interval, the blue region is seen to slowly overtake the red region as the outermost filaments. Since these are the only ones that show up in this solid surface rendering, this means that there is a constant recirculation of the filaments within the bubble region. The red and blue filaments soon become garbled as before indicating that their locations are very close to one another. The simulation here was also set up with fewer filaments in the low circulation region before the ramp-up than were in the baseline case. Similar runs were done with the same number of filaments as the baseline case, and the results were undistinguishable, so it was concluded that since these filaments are assigned such a low value of circulation, there really is no added value to having them included. In the interest of computational time, only three units of these

filaments were included at the front of the vortex tube for continuity purposes. In theory, these filaments extend to infinity for the satisfaction of Helmholtz's laws.

In this run it is noticed that the breakdown region forms exactly as in the baseline case, only sooner and farther upstream due to the decreasing velocity. By a time of 2.4 the red ramp-up region has been entrained into the bubble which is then followed by the blue low circulation region. This shows that there is a negative axial velocity being induced on the downstream filaments by the bubble structure. After this, the filaments remain inside this bubble and mix together making interpretation difficult. Taking a look at the axial velocity profiles of the filaments will help in interpreting when a stagnation point first forms and what happens to the filaments after the formation. The following graphs show the time evolution of the induced axial velocity at three different radii of the tube. The assigned convective axial velocity profile is also shown, as is the combination of the convective and induced velocities at  $r = .12$ . This combined velocity represents the actual fluid velocity of the filaments.

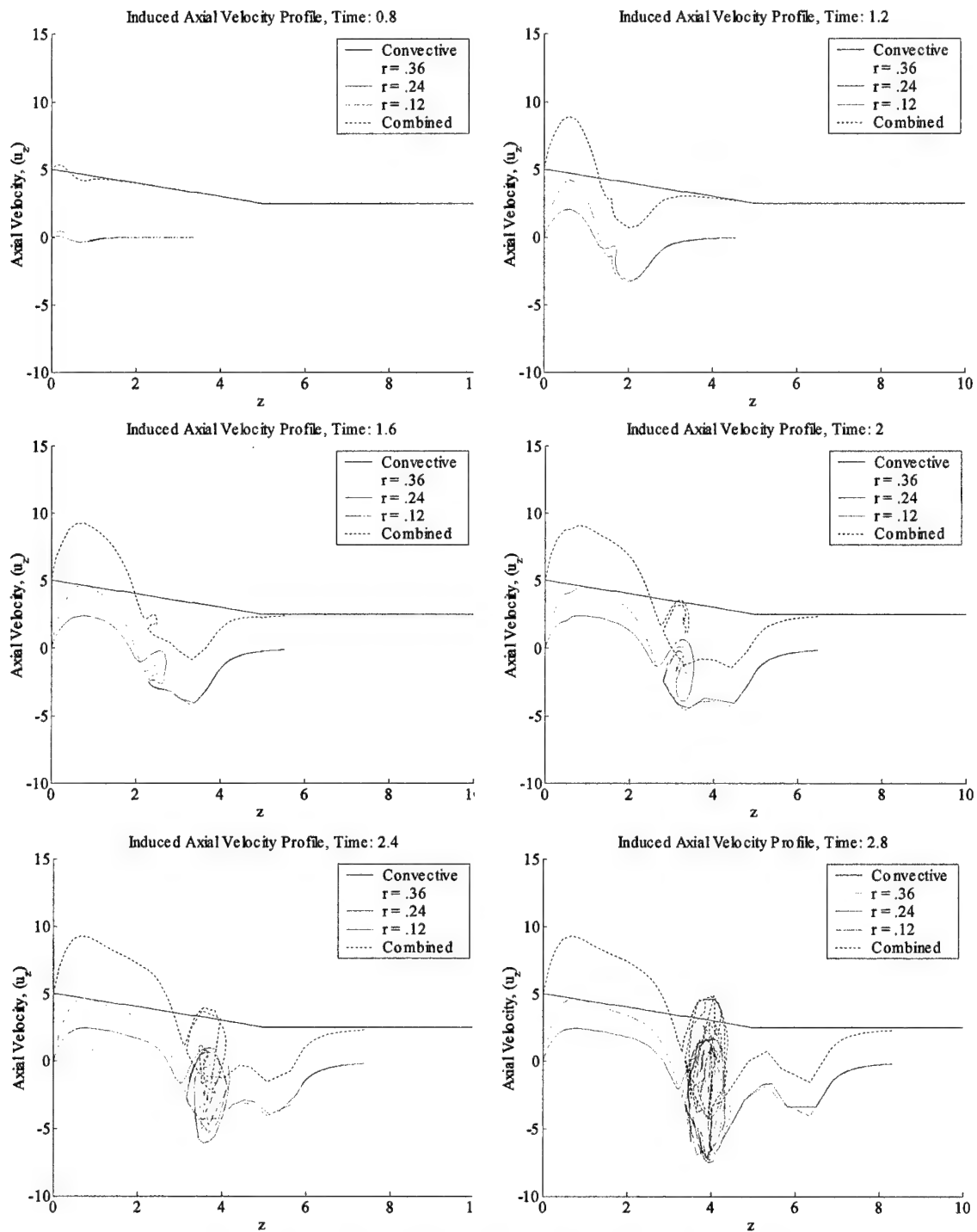


Figure 4-7: Induced velocity profile for velocity gradient run

A stagnation point is identifiable when the combined velocity first reaches zero. This is seen at a time of about 1.6. The jet like velocity profile upstream and wake like



profile downstream of the bubble is identifiable in these plots. The entrainment of the red ramp-up region is seen by a time of 2, and then the filaments become compressed together making for induced velocities that vary rapidly inside the bubble region. This region is responsible for preventing the simulation from reaching a steady state breakdown position. Even with the lower convective velocities, this bubble will still travel downstream due to some of the induced axial velocities being positive. Upstream of this region, however, the simulation is quite stable as the induced velocities there have reached a definite steady state. The main problem that has been identified with the simulation is that there is no mechanism for the vortex filaments to leave the bubble region and travel downstream. In real breakdown, a stagnation point and some recirculation of the fluid does occur, but the fluid then leaves the bubble area or spirals out and into the non-steady breakdown wake. In the simulation, there is currently nothing to prevent the filaments from continually wrapping around each other and destroying the structure of this bubble. The next step is to try to implement a mechanism into the code that will allow this bubble to empty so that the filaments may flow through it.

#### 4.2.2 *Filament Turn-off Case*

As was mentioned in the DPIV results (section 3.3), before breakdown there exists in the vortex a tight core with solid-body like rotation and thus a high value of axial vorticity. However, through the process of breakdown it was seen that the azimuthal velocity in this core is lost, and the vorticity becomes more spread out. This would suggest that at the point of breakdown there is a self-sustained negative axial vorticity gradient, meaning there is high vorticity upstream, and low vorticity downstream of breakdown. This is not evident in the current simulation as the vorticity of the filaments remains constant, but more and more filaments wrap themselves up into the bubble of the core. To put this into the simulation requires a process that may seem very artificial at first, but it will become evident that there is good physical reasoning for this method.

Up to this point, the initial vorticity gradient has been sufficient to develop a turning point and a breakdown bubble. In order to make this stationary, the filaments are then turned off after they have been through the bubble and are in the recirculation zone. This turn-off means that they no longer receive or induce velocities in any direction, but merely convect downstream with the locally prescribed convective velocity for the remainder of the simulation time. This is exactly the same as the “turn-on” plane located at  $z = 0$  where the filaments’ induction on each other is activated. The only difference is that it is not a spatially defined plane where this happens, but relative to the breakdown bubble. First, the simulation is run just as in the baseline case up to the point where a recirculation region first forms (time = 1.6). Then, the filaments at every radius in this zone and everything downstream are turned off. Next, as the simulation progresses and new filaments enter the recirculation zone, they are turned off as well and the simulation continues. Considerable trial and error went into defining which filaments to turn off and the rate at which they are turned off. The filaments themselves are left in the rendering of the vortex tube for clarity, but they have no effect on the tube itself. The convective velocity gradient similar to the previous case is left in to aid in development of a stagnation point. All filaments behind the ramp-up zone are rendered clear except for some regularly spaced filaments that are colored with different colors to serve as markers. The intent is to show how the filaments travel through the breakdown structure and into the wake, with the structure itself remaining stationary. In creating this location where the filaments are turned off, a self-sustained vorticity gradient has been created, just as happens in real vortex breakdown.

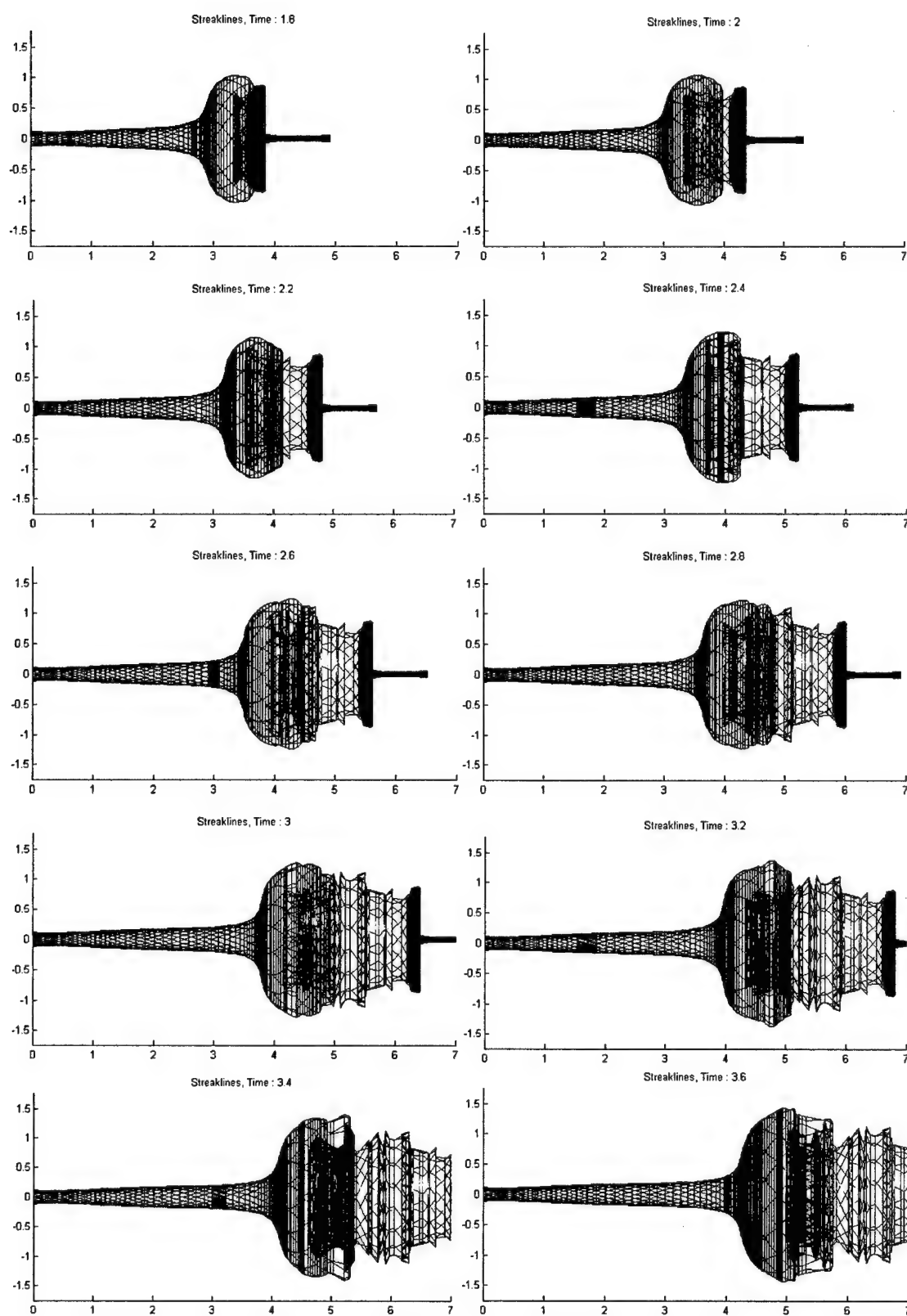


Figure 4-8: Simulation results from turn-off case

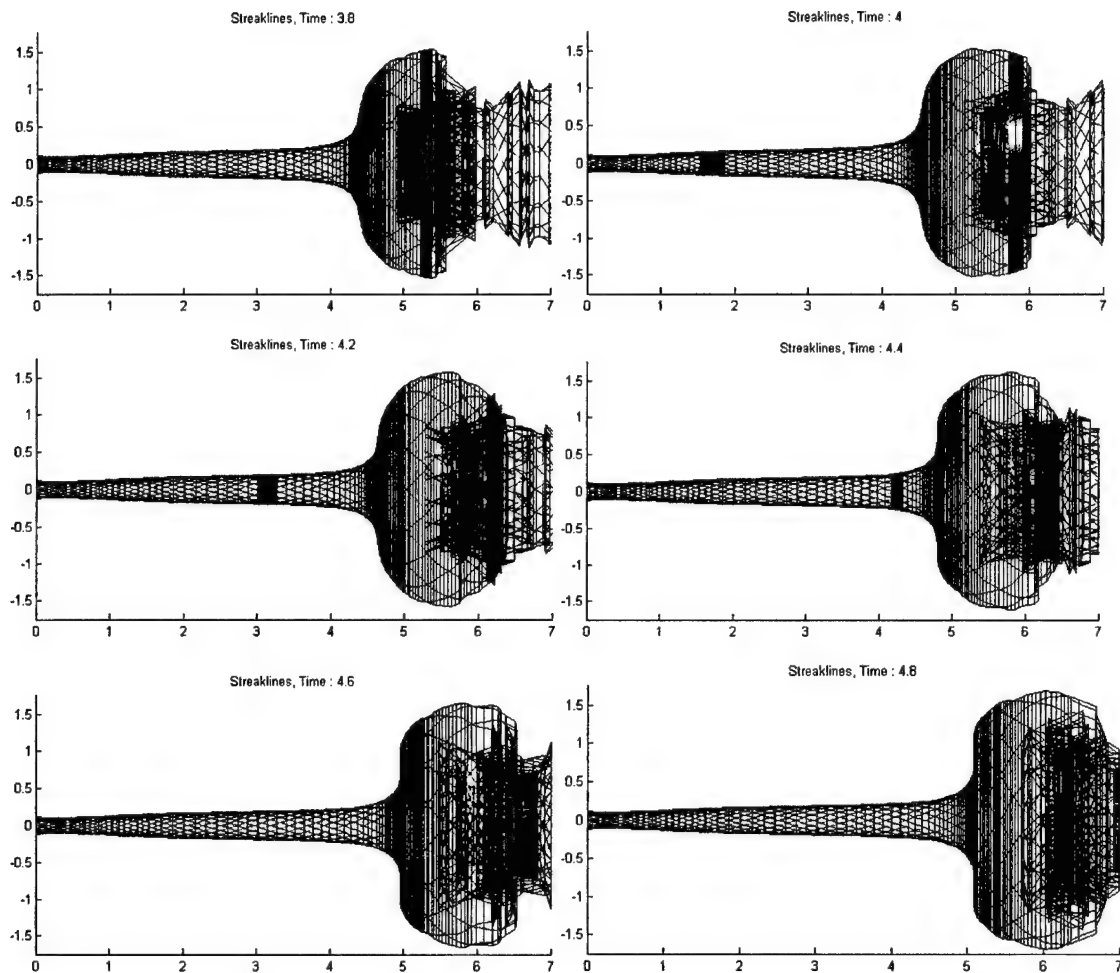


Figure 4-8 (cont.)

To see the filaments traveling through the bubble region, track for example the blue colored filament which is emitted from the source at time of 2.2. It travels through the steady part of the vortex up to the radial expansion region by a time of 2.6. It then travels through the breakdown bubble and recirculation zone, and then into the wake by a time of 4.4.

The results from this run have shown that the breakdown bubble is a stationary and steady structure if a self-sustained axial vorticity gradient exists. Vortex filaments travel through the tube into the radial expansion zone, have a turning point and enter the recirculation zone, and then are turned off to simply convect downstream. This structure remains relatively constant and in a fixed location while the filaments themselves pass through.

The process of turning off these filaments may seem artificial, but it is justified if it is assumed that when two filaments with equal vorticity vectors that point in the opposite direction come close to one another, they have a canceling effect. This is essentially what happens in the wake of breakdown. As the filaments wrap up on each other, the simulation used by Cain was unable to distinguish the fact that two opposite vectors would actually cancel themselves out. The sum of the effects from these two filaments is what makes the simulation wrap up and become garbled. In real flow, the viscosity of the fluid would have a smoothing effect and the mixing in the recirculation zone simply cancels out the effect of those vortex filaments on the rest of the flowfield.

### ***4.3 Further Variations of the Vortex Filament Method***

Several other modifications of the vortex filament method were made over the course of this study. The results thus far have been marginal, and they are presented here mostly for documentation in the hopes of providing ideas and inspiration for future work

#### ***4.3.1 Core Interaction with Outer Region***

The dye visualizations presented in section 3.4 showed that flow inside the core of the vortex or very close to the core would undergo vortex breakdown and have a recirculating region, while dye introduced at a slightly larger radius into the outer region of the vortex would simply swirl around the vortex breakdown location and retain its original path and swirl until it finally was mixed with the core flow somewhere in the wake of the breakdown. The point being that at the location which is usually referred to as vortex breakdown, it is only the small core region of the vortex that actually has a recirculation zone, while the outer region of the flow remains relatively undisturbed for a significant amount of time. It was thought that this same phenomenon could be seen with the vortex filament simulation by placing one ring of the filaments at about twice its original radius from the baseline case, and observing the interaction of this ring with the core where breakdown forms. The circulation distribution was not changed, so the azimuthal velocity profile would appear slightly different from what was presented in Cain. This was assumed to have minimal effect though since the contribution from this

one outer ring to the whole circulation of the tube is minimal. In Figure 4-9, the red filaments are just like those that have been presented in the original case run by Cain. The blue filaments are those that are placed at a radius of .84.

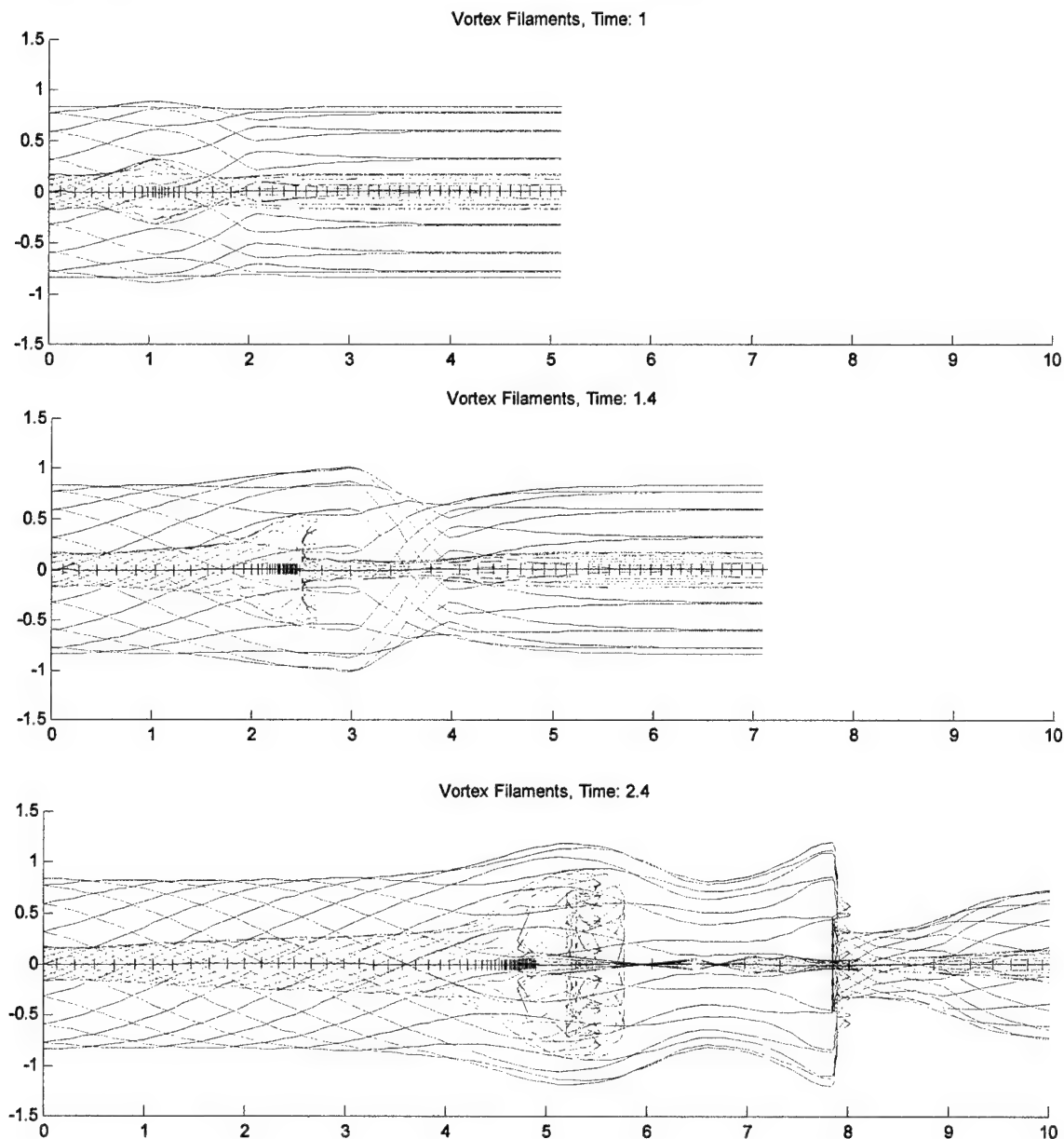


Figure 4-9: Filaments at  $r = .12$  (red) and  $r = .84$  (blue)

It is interesting to note that while the red filaments have an obvious recirculation region which is indicative of breakdown, the blue outer filaments do not have that same turning point and recirculation. There is relatively little disturbance to the blue filaments

in the region where the red ones undergo breakdown. It is not until some distance downstream that the blue filaments reach what looks like a turning point. This confirms what is seen in the dye visualization, and gives greater importance to the velocity profile in the core of the vortex in setting up and determining vortex breakdown.

#### 4.3.2 *Dual Apex Vortex Interaction*

The vortex filament method in its current form simulates a straight axisymmetric vortex tube. The best physical relation to this simulation would be that of a swirling flow in a pipe. In this study it was desired to make the vortex filament method able to simulate the flow in the two leading edge vortices of a delta wing. From dye visualizations of breakdown over delta wings, it has been observed often that the position of breakdown seems to oscillate even when upstream flow conditions remain constant. This has been observed and termed longitudinal wandering by Payne et al.(*ref. 25*). It was hoped that this simulation could provide insight into this phenomenon. The modeling of the core of these vortices by a constant value of circulation is justified by the DPIV results. Section 3.3.3 showed that no vorticity or circulation is added into the vortex's core once it is formed above the wing.

In attempting to simulate the flow over a delta wing, several things must be modified from the original code. The most significant consideration is that the vortex tubes are no longer axisymmetric. This code must now be able to calculate induced velocities at every node inside of it instead of just at one slice of the tube. Two vortex tubes are initialized upstream of the  $z = 0$  plane. Once they emerge from the plane, they induce velocities on each other as well as themselves. This quadruples the computational time. Each is given its own convective velocity which carries them over the imaginary delta wing surface with an angle between them that would be typical of a common delta wing. Also, the two vortices are assigned equal but opposite values of circulation, just as the two opposing vortices of a delta wing. For best results it was found that the tubes at the origin should be shifted slightly away from each other to prevent the filaments from initially inducing very high velocities on one another and disturbing the tube for the rest of the simulation. Also, the induction on/off plane was made normal to each vortex tube

and not simply the  $z = 0$  plane to eliminate initial non-symmetries caused by cutting the vortex tube at an angle. A diagram of the initialization setup of these two tubes is shown next in Figure 4-10.

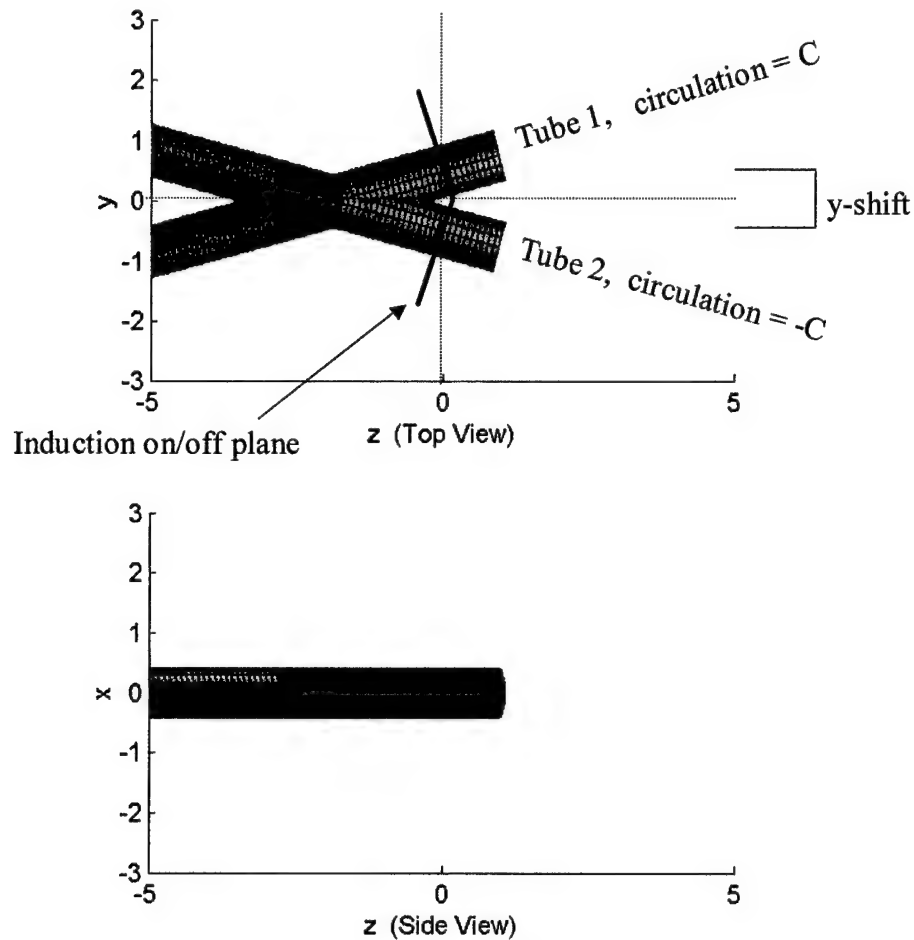


Figure 4-10: Setup of dual apex vortex interaction simulation

In the presentation of these results, a top, side, end, and angled view of the vortices will be presented because of the difficulties of seeing the non-symmetries with just one view. The surface of the filaments at  $r = 0.3$  are shown to make the vortices larger and easier to see. Also, the magnitude of circulation of each vortex was set to 25 in order to make the effects of each vortex on each other more evident. The radial spokes are left out of this run as it was determined they had a relatively small effect even in the symmetric cases above.



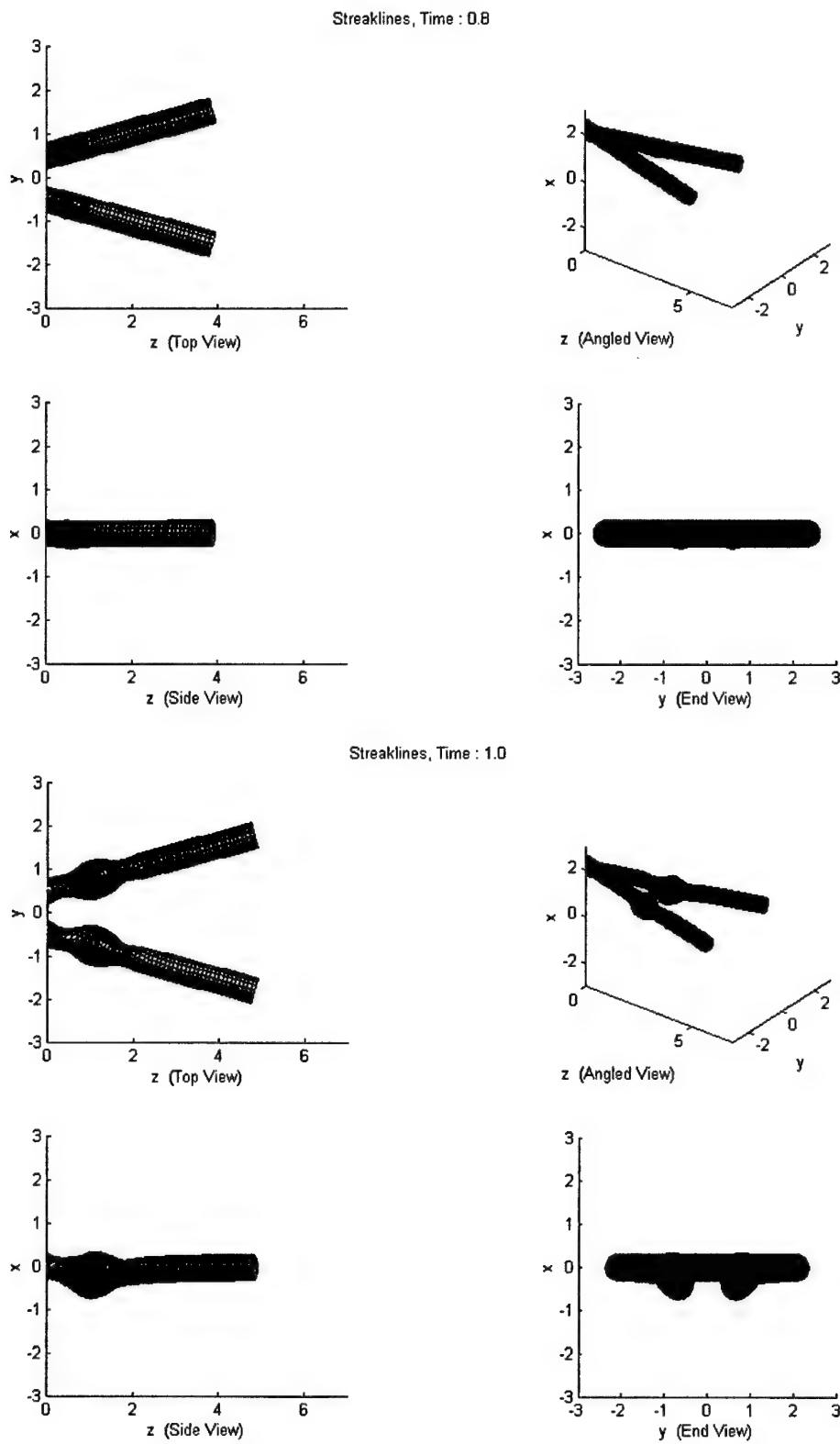
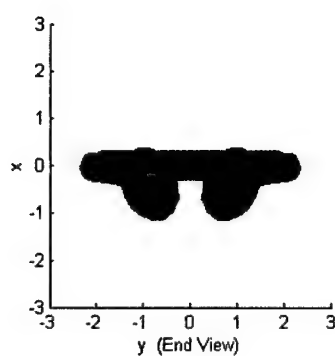
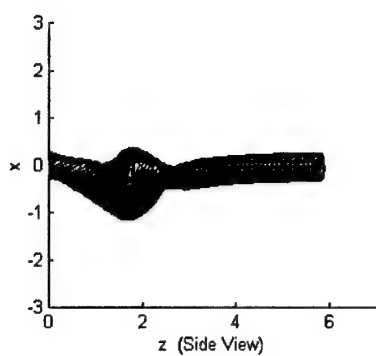
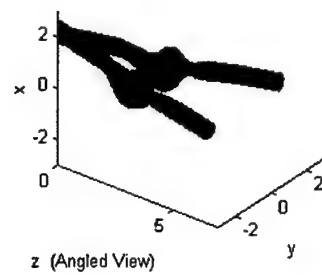
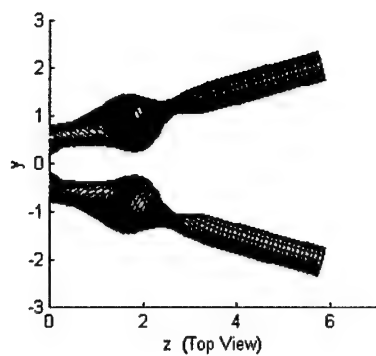


Figure 4-11: Results from dual apex vortex simulation

Streaklines, Time : 1.2



Streaklines, Time : 1.4

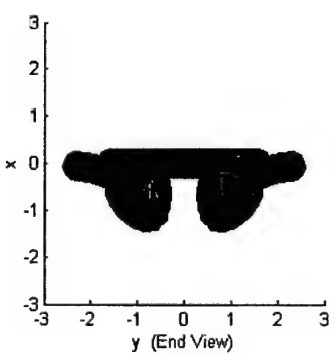
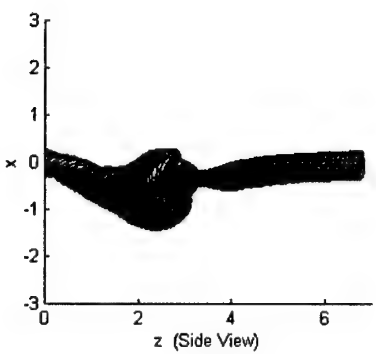
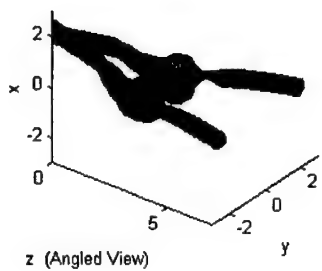
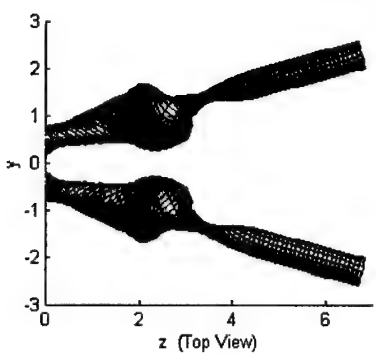


Figure 4-11 (cont.)

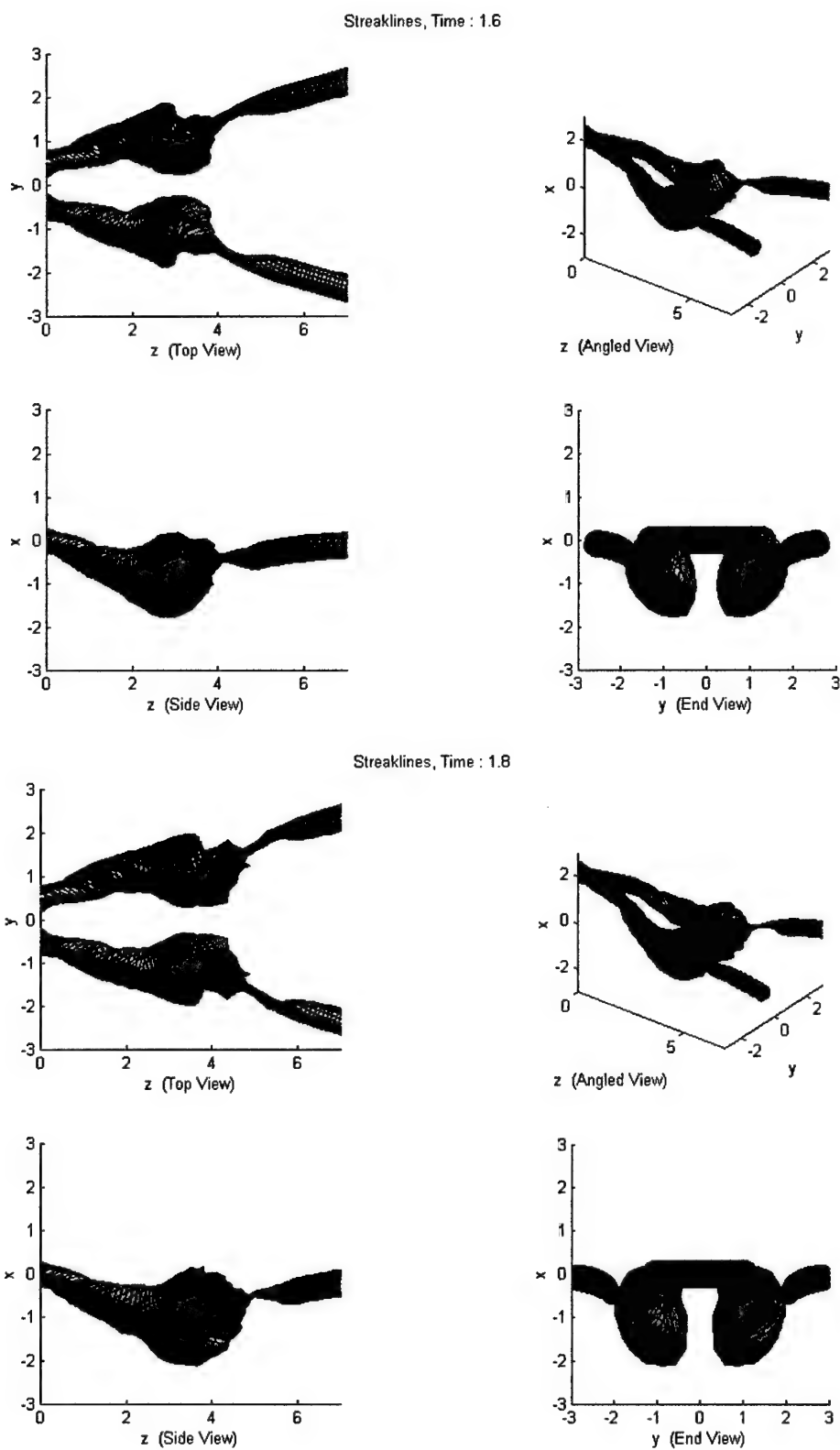


Figure 4-11 (cont.)

In this case, the longitudinal wandering that was sought did not occur. The most prominent result is that the vortex tubes induce a downward ( $-x$ -direction) velocity on one another due to their sense of rotation. This illustrates how the pair of LEVs are able to stay attached to the wing surface of a delta wing operating at a high angle of attack. Relatively little could be inferred from the vortex breakdown region of the vortices because the inherent non-symmetry made the results difficult to interpret. A radial expansion region and vorticity sign switching is, however, still evident.

The conclusion of this simulation appears to imply the following: the oscillatory wandering of the two vortex breakdowns is not so much related to the mutual interference between the two vortices, but rather due to some periodic instability of the flow near the vicinity of the apex region including the pressure surface and the beveled leading edges.

## 5 Discussion of DPIV and Simulation Results

The focus of this section will be to present the newly discovered aspects of the leading edge vortices along with ideas on how the vortices should be modeled in numerical simulations. The traditional view that the flow over a delta wing is mostly conical in nature will be challenged. A discussion of the simulation results is also presented along with how the new findings add to the self-induction theory of vortex breakdown. Finally, vortex breakdown suppression and control methods are reviewed in light of this new information.

### 5.1 *A New Model of Delta Wing Leading Edge Vortices*

This section will seek to describe some of the new aspects of delta wing flow that were found through the use of DPIV.

#### 5.1.1 *Traditional Views*

It seems to be a widely held view that the flow over the lee-side of a delta wing can be considered to be conical. That is, fluid properties are constant along rays emanating from the tip of the wing. Visbal (*ref. 26*), for example, described the core of the LEV as being circular in shape and growing “linearly in the downstream direction forming a vortical region of ‘conical’ shape”. The same conclusion was arrived at by Visser and Nelson (*ref. 20*) using a hot wire study of flow about a  $75^\circ$  sweep delta wing. They observed near conical flow for the majority of the pre-breakdown region. It should be remembered that the delta wing used in this study had significantly less sweep ( $65^\circ$ ) which could account for some of the differences in observation. Nevertheless, the difference in observation between the current study and the widely held conception of a conical flow field is undeniable. The assumption that the flow field is nearly conical is significant in that it greatly simplifies the flow field. If the flow at one chord location of the wing is known, it allows the extrapolation of the rest of the flow over the wing. In high speed flow, it would also allow the use of well-known mathematical methods such as complex variable theory to analyze the flow (*ref. 27*).

### 5.1.2 *Deviations From and Additions to Traditional View*

A major finding of this study is that the flow over a delta wing is largely non-conical, especially in the solid-body rotational core of the LEV. As was shown in section 3.3.3, once the core of the vortex is formed, it retains its same shape and azimuthal velocity profile over the length of the wing, up to the point of breakdown if it occurs. If the flow were conical, the profile in the core would change with x-location. The size of the core would increase as the point of maximum azimuthal velocity would continually occur at a larger radius. This would also cause the circulation in the core to grow proportionately. Neither of these aspects were observed in this study, however. The core size and circulation remained the same after being established at some distance from the wing apex. Another requirement of conical flow is the lack of any axial pressure gradients. The axial velocity must remain constant along rays emanating from the tip. It was seen in Figure 3-3 that this was definitely not the case as the axial velocity was seen to vary a great deal, especially for angles of attack above  $15^\circ$ . This fact alone raises questions about assuming that delta wing flow is largely conical.

One of the questions that this study set out to explain was how much vorticity and circulation was fed into the core of the vortex as it traveled downstream. The simple answer to this question is that no vorticity enters the solid-body rotational core of the vortex once it is formed slightly downstream of the wing apex. At least to first order, this fact is seen in both the plots of circulation in the core (Figure 3-20), and the plots of the azimuthal velocity profile for the whole vortex (Figure 3-18). It would seem that all of the fluid which feeds into the vortex downstream of the core formation point enters the outer regions of the vortex and causes the azimuthal velocities there to increase, but not beyond the maximum azimuthal velocity which is found at the edge of the core. A simple sketch illustrating this result is shown in Figure 5-1.

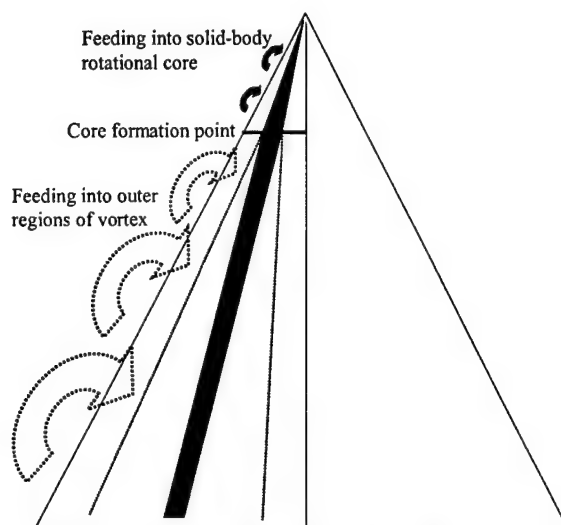


Figure 5-1: Feeding of circulation into the vortex core and outer region

The existence of a constant vortex core has been experimentally shown, and now the physical reasons for its development will be explained. A conceivable reason why the vortex core does not continue to grow downstream of a certain point is the vorticity cancellation: the secondary vortex having a sign opposite to that of the primary vortex becomes entrained deep into the primary vortex, resulting in the severance of the vortex core from the vortex sheet by cross-vorticity neutralization.

A sequence of the development of the primary and secondary vortices is sketched in Figure 5-2 on successive cross-core planes along the wing chord. In (a), the boundary layer over the suction surface is driven towards outboard by velocity induction from the primary vortex. A fluid particle,  $p$ , within the boundary layer moving with outboard velocity is subject to the adverse pressure gradient due to its position relative to the vortex core where the pressure is lowest. Thus in (b) the particle  $p$  separates from, and lifts off, the wing surface. In (c), the secondary vortex starts to be entrained into the primary vortex. As the secondary vortex is entrained deeper into the primary vortex, as shown in (d), a localized region of zero vorticity is formed near the junction between the vortex core and the vortex sheet emanating from the leading edge, due to vorticity cancellation.

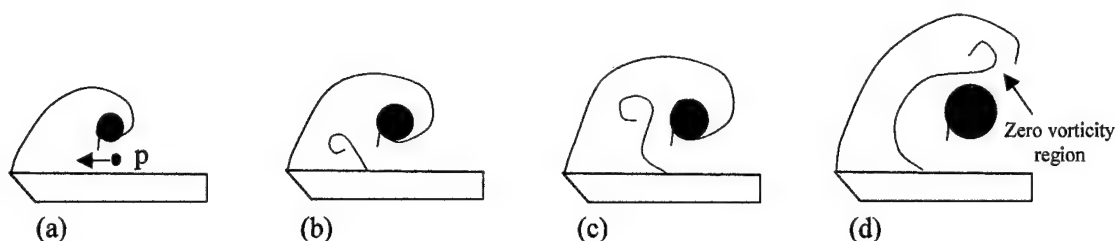


Figure 5-2: Sketch of vortex sheet and secondary vortex cancellation

In other words, the secondary vortex severs the umbilical chord of the primary vortex sheet feeding vorticity to its core. Once the vorticity feeding stops, the vortex core ceases to grow. Thereafter, the size of the vortex core and its circulation remains unchanged. The secondary vortex thus plays an active role in shielding the primary vortex core from the shear layer and vortex sheet.

Such regions of zero-vorticity near the junction between the vortex core and the vortex sheet are clearly present in Figure 3-14. Examples of secondary vortex entrainment are also observable in numerical simulations done by Gordnier and Visbal (*ref.28*). Figure 5-3 shows two examples from their study of unsteady entrainment of the secondary vortex into the vortex sheet feeding the primary vortex. The left side depicts a full chord view of the unsteadiness, while the right side focuses on one chord location. Deep in the primary vortex and vortex sheet, pockets of oppositely signed vorticity (red) are readily observed, however, the aforementioned role of the secondary vortex in limiting the growth of the vortex core appears to have gone unnoticed.



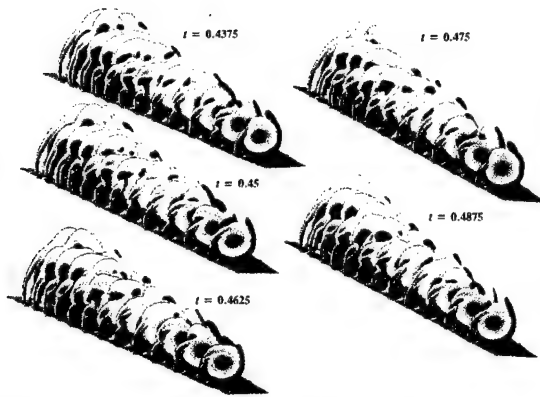


Fig. 6 Three-dimensional unsteady vortex structure  $x = 0.3-0.85$ , contours of axial component of vorticity.

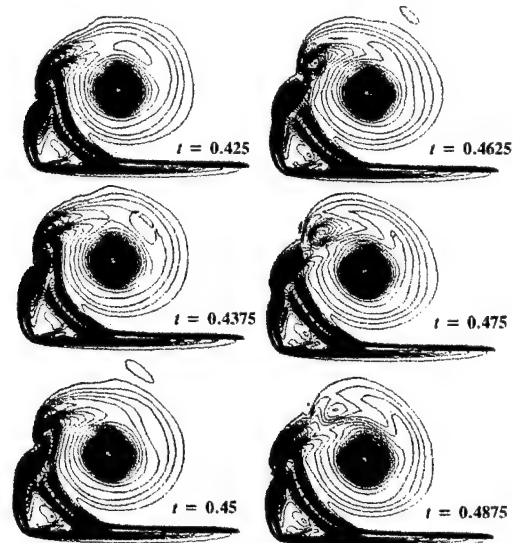


Fig. 7 Unsteady vortex structure,  $x = 0.7$ , contours of axial component of vorticity: blue  $> 0$ , red  $< 0$ .

Figure 5-3: Numerical simulation of unsteady vortex structure and secondary vortex entrainment from *ref.28*.

A question may immediately arise: once the vortex sheet is severed from its core, does the vortex sheet ending in a fluid violate Helmholtz's law? One possible scenario of how this law is upheld is shown in Figure 5-4 where a vortex filament from the secondary vortex is aligned with the open end of the vortex sheet, although other scenarios may be quite possible in this complex three-dimensional unsteady flow.

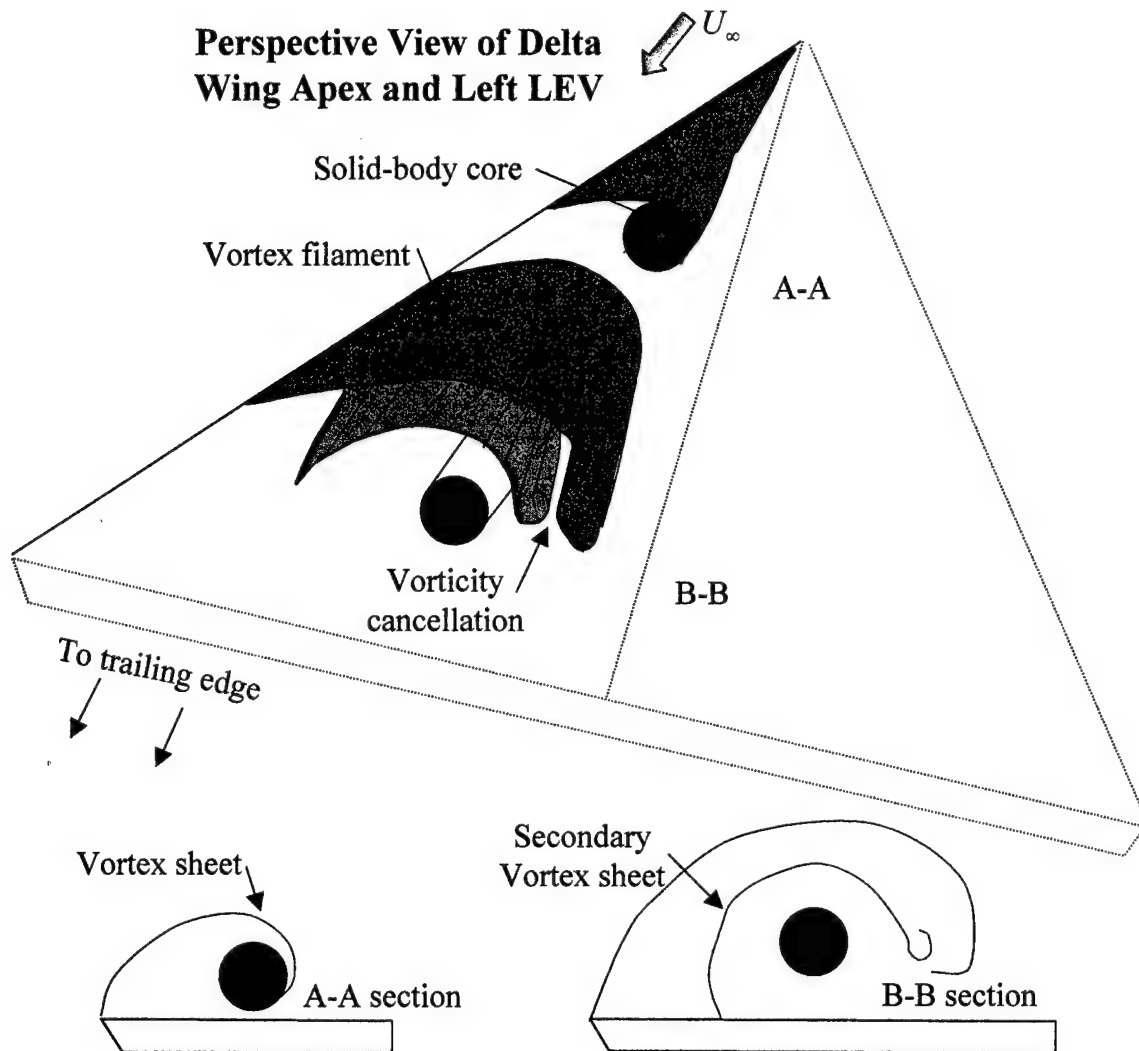


Figure 5-4: Sketch of the development of the core and eventual vorticity cancellation by secondary vortex

A second question concerns the connection of the finite core size and the downstream increase of axial velocity from the apex until breakdown that is usually associated with delta wings (Figure 3-1). Upon severance from the vortex sheet, there is no additional feeding of fluid or vorticity from the vortex sheet to its core, so there can be no net increase in velocity of the core to satisfy continuity in this incompressible flow. The current study found that for a wing with less sweep ( $65^\circ$  compared to  $75^\circ$  in Figure 3-1), the axial velocity at the center of the core increases from the apex up until the point where the core is completely formed, and then levels off in the region where the constant

core was located before dropping at the point of breakdown. The reader is referred back to Figure 3-3 for confirmation of this.

This idea of a constant circulation core has great importance. It would suggest that the entire profile of the vortex core is established near the wing tip. In the case of the 45cm chord wing used in this study, the core was established between 5 and 10cm from the apex, or by about 15% chord. How it convects downstream then is just a matter of the axial pressure gradient that is imposed on the core due to the angle of attack of the delta wing. This, then, gives a great amount of importance to the wing tip, with it being the source of all of the vorticity within the vortex core. It has already been established that the vorticity of the core, and especially the transient formation of a vorticity gradient, is a cause of vortex breakdown. This would suggest that changes to the tip of the delta wing would have far greater effects on breakdown and the flow field in general than changes anywhere else. The normalized circulation inside of this core,  $\Gamma^* = \frac{\Gamma}{c \cdot U_\infty}$ , is then solely a function of the wing tip shape and orientation to the flow ( $\alpha, \Lambda, \beta$ ).

The circulation of the vortex taken at a larger radius encompassing the outer region of the flow was observed to increase linearly with x-location. This is due to the fact that a straight edged delta wing was used, and thus the radius where the shear layer fluid enters the vortex is linearly growing with x-location also. This is because the local semi-span of the wing,  $s = \frac{x}{\tan \Lambda}$ , grows linearly with x for a constant sweep angle. The total circulation of the vortex was also noticed to grow or remain nearly constant immediately after the breakdown location. It was not until far in the wake of breakdown that a drop in the total circulation was noticed, suggesting that the effects of breakdown start initially just in the solid-body rotational core, and take some time to spread and affect the outer regions of the vortex.

It remains unclear what establishes the distance required to completely form the core of the vortex. For both the 30 and 45cm chord wings tested, the core was formed and remained constant from about 15% chord up to vortex breakdown. This was invariant with the angle of attack tested. The wings had a common sweep angle

suggesting that the required distance measured in percent chord scales with the sweep angle, or more accurately the semi-span of the wing. More testing is warranted for wings of different sweep to obtain how the formation point varies with sweep. It is expected that wings with greater sweep would require a greater distance to form the core due to the smaller distance between the center of the core and the wing leading edge where the shear layer is located. This small distance makes it easier for the shear layer to feed vorticity into the core and not just into the outer region. It is suspected that this would make the flow field for higher wing sweeps more conical in nature since the size of the core is increasing over this region.

It can be argued that the existence of a constant size and strength vortex core in an LEV explains the similarities in the structure of vortex breakdown on delta wings and in pipes. The core of a LEV and swirling pipe flow closely resemble each other, and as has been noted, breakdown first forms in this core. Also, it is speculated that the shielding of the primary vortex core from the vortex sheet by the secondary vortex helps to limit the circulation in the core, and could serve to delay breakdown due to the lower circulation and induced backflow caused by self-induction. The breakdown location in this case would then be farther downstream than if the vortex sheet continually fed into the vortex core causing the circulation there to be stronger.

### 5.1.3 *Suggestions for Modeling the LEV*

Several attempts have been made to model delta wing flow numerically (*refs.* 24, 28, 36, 37, 38, and 39), and to infer from that the causes of vortex breakdown. An excellent review is provided in Levinski (*ref.* 40). It has generally been the case that the vortices have been modeled as having increasing strength traveling along their axis. There have also been attempts to link some critical circulation value of the vortex to the onset of breakdown in order to develop a criterion for breakdown (*ref.* 22). The research here suggests a slightly different and simpler way of modeling the important regions of the vortex for obtaining breakdown information. The dye visualization and DPIV experiments here suggest that the solid-body core is the critical region where breakdown is first formed. The vorticity assigned to this area should be set to a constant value

(except for a starting portion where there is initially an axial vorticity gradient). The circulation of only this solid-body region is seen to have the greatest effect on breakdown. The greatest amount of attention should be paid to the circulation and natural axial pressure gradients in this core, with the outer region assumed to have only a secondary effect. It has been shown through simulations with the vortex filament method (section 4.2.2) that a constant value of circulation upstream of breakdown combined with a vorticity gradient in the region of breakdown is enough to reproduce all the components of breakdown.

## **5.2 *Discussion of Simulation Results***

### **5.2.1 *Results from Simulation***

The vortex filament method has already proved effective at simulating the transient formation of vortex breakdown based on an axial vorticity gradient. First, it was shown in section 4.1.1 that the numerical values of circulation and vorticity assigned to the vortex filaments were reasonable values and represented a realistic physical flow condition where breakdown was likely to occur. While this simulation is still not expected to give accurate quantitative results due to the inviscid nature of the vortex filament method, it does prove that the inviscid effects of a vorticity gradient are sufficient to induce breakdown.

This study focused on making the breakdown location of the simulation reach a steady state position. This proved difficult to do as the filaments of the existing simulation continued to roll up inside one another and gave nonsensical results. The DPIV results were examined and revealed a definite self-sustained axial vorticity gradient in the core of breakdown as evidenced by the dead core region. This is presumably due to the vorticity vector being rotated in a non-axial direction, or the cancellation of vorticity altogether. When this self-sustained vorticity gradient was entered in the simulation as in section 4.2.2, it showed that it was indeed sufficient to make the vortex filaments upstream of the gradient undergo pile-up, radial expansion, and vorticity sign switching. There was also enough negative induced axial velocity at the point of breakdown for the

breakdown bubble to remain in a stationary position, while the individual filaments themselves would flow through the bubble and into the wake. This made for a quasi-steady form of breakdown. Admittedly, the turn-off of the filaments in the wake of breakdown is somewhat artificial in that it violates the Helmholtz theorem that a vortex cannot end in a fluid. However, there is some justification for it in that two oppositely signed filaments placed next to each other would have no combined effect on the tube. By turning the filaments off in the wake, it is assumed that the vorticity contained in each filament is cancelled out by a filament in close proximity and with opposite sign. With this finding, some modification to the self-induction theory presented by Cain is warranted.

### 5.2.2 *Modified Self-Induction Theory*

None of the aspects of the transient formation of vortex breakdown contained in Cain's self-induction theory are being questioned. This study found it to be an accurate representation of the factors leading up to breakdown. However, Cain's theory basically says that once the turning point has formed, viscosity effects take over and a stationary breakdown location is reached. With the current turn-off case showing a stationary form of breakdown with still no viscosity included, this theory needs some modification. The basic modification is that once a turning point is developed and the breakdown bubble is present, all of the vorticity inside of the recirculation zone cancels itself out. This in turn makes a self-sustained negative vorticity gradient from just upstream of breakdown where there is high axial vorticity, to the wake of breakdown where there is no vorticity. This gradient feeds back into the inviscid feedback mechanism causing a continual pile-up, radial expansion, and vorticity sign switch as the filaments flow through the bubble or vorticity gradient region. It is then argued that viscosity does play a role in smoothing out the velocity gradients found in the recirculation zone in the simulation. This also aids in the cancellation of vorticity. A side-by-side comparison of the original and modified theories is presented in Figure 5-5.

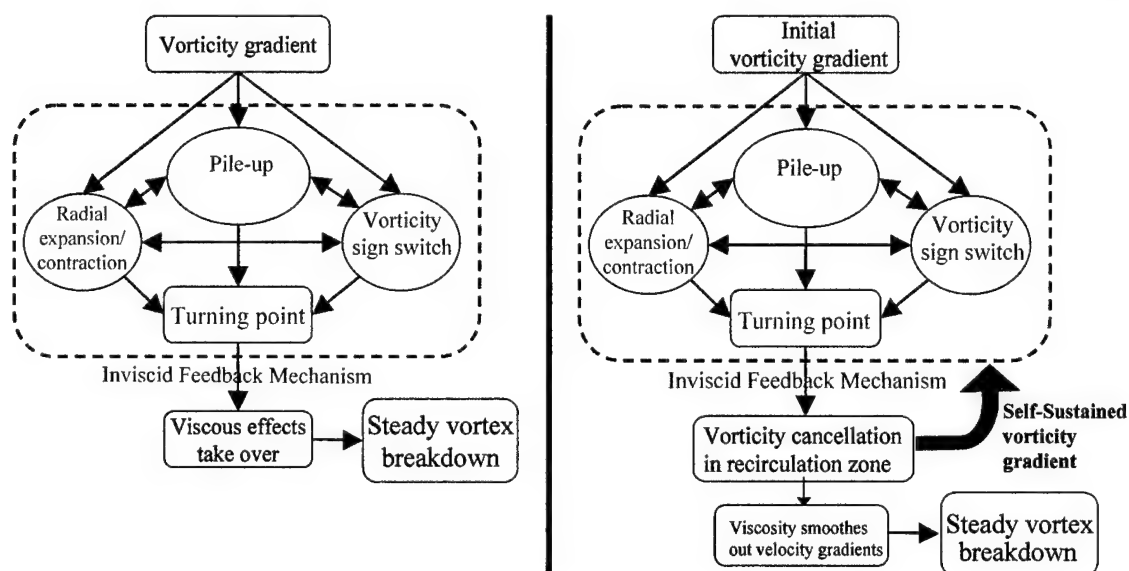


Figure 5-5: Self-induction theory of vortex breakdown. Original (left) vs. Modified (right)

### 5.3 Vortex Breakdown Suppression and Control

The motivation for this work is to ultimately be able to suppress or control vortex breakdown in some way. Many studies have focused on this as it is as fundamental to the field of aerodynamics as controlling boundary layer separation and stall on a traditional rectangular airfoil. As stated in the introduction, it is very desirable to be able to control or eliminate breakdown as it can have several negative effects on an aircraft such as a loss of lift or buffeting and high cycle fatigue leading to failure. A brief review of some control methods is presented along with analysis of these methods and recommendations in light of the results of this study.

#### 5.3.1 Review of Some Breakdown Control Methods

A wide variety of vortex breakdown control methods have been previously investigated. The investigations seek to do one of two things; delay or weaken the onset of vortex breakdown, or move the LEV in a way that breakdown cannot adversely affect other structural components. The methods used include active control such as constant blowing or suction, or periodic blowing and suction. Passive control techniques such as stationary vortex generators or wing surface shaping have also been investigated.

Shah (*ref. 29*) and Thompson (*ref. 30*) showed that a stream-wise fence mounted on the wing leading-edge extension on an F/A-18 caused the separation of the LEV into two counter-rotating vortices. This effectively moved the vortex away from the vertical tails and reduced the effects of breakdown on tail.

Sheta et al. (*ref. 31*) used a multi-disciplinary computational investigation to see the effects of tangential blowing on vortex control. Their work found that blowing directly into the LEVs was the most effective in delaying breakdown or reducing the buffeting response. The blowing tangential to the vortex core itself, and provided in such a way as to weaken the vorticity in the core, proved the most effective. This result agrees with the current study in that the solid-body core has been identified as the critical area where all of the physical aspects that set up breakdown are present. Significant modification of this core will prove to have the greatest effect on breakdown.

Moeller and Rediniotis (*ref. 32*) used pneumatic vortex control (PVC) actuators on a delta wing in a low speed wind tunnel to control the position of vortex breakdown and resulting pitching moment on the wing. The study found that by using actuators located near the trailing edge and blowing parallel to the core, the position of breakdown could be modified. By blowing opposite to the axial velocity of the LEV, the breakdown position moved upstream, and blowing with the axial velocity delayed the breakdown downstream. This method essentially just modifies the axial pressure gradient and resulting velocity profile that the LEV travels through. It was shown in section 3.1 that the axial velocity profile is largely dependent on the angle of attack, and that a stagnation point is seen at the point of breakdown. The simulation has shown that for a given vorticity gradient, a certain amount of backflow will be induced at a point on the vortex. If this backflow is greater than or equal to the convective axial velocity set up by the pressure gradient, then a stagnation point and resulting breakdown will occur. By blowing along this line, the convective velocity is being changed, and thus the position of breakdown can be modified. It should again be emphasized that blowing directly along the core of the vortex is likely to have the largest effect since that is where the largest induced axial velocities are located.



Periodic blowing and suction has also been investigated by Guy et al. (*ref.* 33). Flow excitation along the leading edge of the delta wing showed that a delay in breakdown by as much as 20% chord and a significant increase in lift were possible. It was shown that this method also altered the axial velocity profile. It is unclear whether it changed the circulation of the vortex by excitation of the shear layer which feeds into the vortex. This type of actuation is slightly different because it is zero net mass flux, meaning that no source of fluid is needed to maintain the blowing or suction. This could be beneficial as creating sources of high pressure fluid often involves added complexity and weight.

Maines et al. used leading edge suction on a  $65^\circ$  delta wing and measured the effect on breakdown position. They found that suction near the wing apex had the largest effect on breakdown over suction anywhere else along the leading edge. Upper surface suction moved the breakdown upstream, while lower surface suction moved it downstream. This result also agrees well with the current study as it has been shown the apex of the delta wing causes the formation of the core of the vortex which in turn induces breakdown. Modifications to this apex region are bound to have the most significant effect on the flow field.

Husain et al. (*ref.* 34) studied vortex breakdown in swirling flow inside a cylinder with a rotating endwall. A small rod was also placed through the axis of the cylinder and the rotation direction of the rod could be controlled. They found that rotating the rod in the same direction as the swirl of the flow suppressed any vortex breakdown bubble at the core, while rotation of the rod in the opposite direction of the swirling flow caused the formation of multiple breakdown bubbles. This can be understood in light of the vortex filament simulation. A counter-rotation of the rod would cause significant vorticity gradients due to the no-slip condition at the rod surface which has been shown to induce breakdown. However, co-rotation of the rod would tend to create positive axial vorticity everywhere along the rod and would negate any gradients.

Srigrarom and Kurosaka (*ref.* 35) also attempted to suppress breakdown by means of modifying the leading edge shape of the delta wing from a straight line to a wavy planform. This transformed the vortex core itself from a straight line to a wavy shape

which was shown to induce less backflow and resulted in a lack of a stagnation and reversed flow region. They found that the effect of the waviness of the wing was the same for one wave near the apex as for waviness along the entire leading edge of the wing. This study has shown that the effects would indeed be the same because all of the properties of the core are formed near the apex of the wing. The waviness for the rest of the chord would have only a secondary effect on the LEV core.

### 5.3.2 *Recommendation for Control in Light of Current Work*

It has been established that the geometry and orientation of the wing tip is what establishes the core circulation of the vortex and sets up the flow pattern for the rest of the wing. Also, the angle of attack of the wing establishes both the circulation in the vortex and the convective axial velocity profile which the LEV is subjected to. These two things determine the location of breakdown along the core. With this in mind, any alteration of the vortex core circulation or the axial velocity profile will modify the breakdown position. The most effective place to change the circulation of the vortex core has been shown to be the very tip of the wing as it is the location where all of the feeding into the core takes place. Any alterations further down the wing chord will only have a secondary effect on the vortex core as it has been shown that there is very little feeding of circulation into the core past the wing apex.

## 6 Conclusions and Recommendations

### 6.1 Conclusions

Vortex breakdown and delta wing flow in general remains a highly complicated topic still worthy of much research effort. The goal of this study has been to answer four questions related to delta wing flow and the simulation of vortex breakdown.

1. How is vorticity fed into the solid-body core of the LEV by the shear layer as the vortex travels downstream?
2. How can vortex breakdown be controlled?
3. Are the parameters used in the current vortex filament method similar to a realistic flow situation where vortex breakdown occurs?
4. How relative is this simulation to real LEV flow, and how should the vortex be modeled?

It is believed that this study found good answers to questions 1, 3, and 4, while question 2 remains an area where much work is still needed. Each question is addressed below.

#### 6.1.1 Vorticity Feeding into the Core

This study found that essentially no added vorticity enters the solid-body rotational core of the vortex after the core is formed near the wing apex. All the circulation and vorticity added subsequently remains at a radius larger than the radius of maximum azimuthal velocity. The core is then seen to have constant circulation and a constant radius from the point of formation to just upstream of breakdown. The physical reason for this is that the secondary vortex interacts with the shear layer severing the attachment between the feeding vortex sheet and its core. The growing size of the secondary vortex allows it to serve as a shield between the shear layer and core, forcing the fluid into the primary vortex at radii larger than the limits of the solid-body rotational core. This view of the core differs significantly from the conical theory of delta wing flow. It is thought that for high sweep angles and relatively low angles of attack that the flow could be nearly conical as the distance from the core center to the feeding shear

layer decreases with increasing sweep angle. Under these circumstances, the shear layer could feed into the core for a large portion of the wing and not just near the tip.

#### 6.1.2 *Vortex Breakdown Control*

Proposed breakdown control methods vary widely and have shown varying degrees of success. This is an area that needs much more research as the benefits of being able to control the vortex are great. This study has shown that control methods should focus on the core of the LEV as this is the key region where breakdown develops. The best area to modify in order to alter the vortex core is the apex of the delta wing as this is where the core forms and all vorticity in the core is produced. Active as well as passive control methods could have the most significant effect if applied in this area. All control methods which focus on the outer area of the core are suspected to have only a secondary effect on the vortex core itself. In summary, to get the most ‘bang for the buck’ from whatever control method is used, its effect should be focused on the vortex core and especially the apex where the core forms.

#### 6.1.3 *Vortex Filament Simulation Parameters*

The DPIV used in this study showed that the parameters used by Cain in the previous work were realistic for simulating an actual flow condition where vortex breakdown was likely to exist. The magnitude of the vorticity gradient in relation to the axial velocity of the vortex was similar to that of common delta wing flow. While the simulation did not have all of the components necessary to arrive at a stationary breakdown location, it does model the transient formation of breakdown well.

#### 6.1.4 *Simulation and Delta Wing Flow Comparison*

The vortex filament simulation, even with its simple geometry and inviscid assumption, does a reasonably good job of modeling the LEVs of actual delta wing flow. As was shown in the DPIV study, the core of the vortex remains constant and does not really change throughout the length of the wing. This is very similar to the present simulation in that once it emerges from the source, the vortex has constant circulation and

size. Also, filaments placed farther outside of the vortex core in the simulation were shown to not breakdown until far in the wake of the core breakdown location. This effect was confirmed by dye visualization over the delta wing. Future numerical simulations could be effective by just concentrating on the core of the vortex as this has been shown to be the critical area responsible for breakdown.

## **6.2 *Recommendations for Future Work***

Based on the findings in this study, several suggestions for future work are warranted:

1. Extend the DPIV investigation to a wider range of delta wing sweep angles to study how vorticity is fed into the core for these wings.
2. Initiate a three-dimensional PIV study of the vortex breakdown region and the flow near the delta wing apex.
3. Investigate in detail the effects of different apex geometries to control breakdown such as the blow-in door application.
4. Investigate ways to include viscosity effects in the numerical simulation of breakdown in order to arrive at a stationary breakdown location.

## LIST OF REFERENCES

1. Kundu, Pijush K., *Fluid Mechanics*, Chap 3, Academic Press, San Diego, 1990.
2. Cain, C.B., "The Self-Induction Theory of Vortex Breakdown", Masters Thesis, University of Washington Department of Aeronautics and Astronautics, 2001.
3. Anderson, John D., *Fundamentals of Aerodynamics*, Second Edition, Chap 5,6, McGraw-Hill, Inc., New York, 1991.
4. Sarpkaya, T., and Novak, F., "Turbulent Vortex Breakdown: Experiments in Tubes at High Reynolds Numbers", IUTAM Symposium on Dynamics of Slender Vortices, pp. 287-296, 1998.
5. Faler, J.H., and Leibovich, S., "Disrupted States of Vortex Flow and Vortex Breakdown", *Physics of Fluids*, Vol. 20, No. 9, pp. 1385-1400, 1977.
6. Spall, R.E., "Transition from Spiral- to Bubble-Type Vortex Breakdown", *Physics of Fluids*, Vol. 8, No. 5, pp. 1330-1332, 1996.
7. NASA Dryden Flight Research Center, <http://www.dfrc.nasa.gov/Gallery/Photo/F-18HARV/index.html>, 1989.
8. Erickson, Gary E., "Vortex Flow Correlation", AFWAL-TR-80-3143, ADA108725, January 1981.
9. Raffel, M., Willert, C., and Kompenhaus, J., *Particle Image Velocimetry-A Practical Guide*, Springer-Verlag, New York, 1998.
10. Merzkirch, W., *Flow Visualization*. Academic Press, 1974.
11. Chen, C.J., and Emrich, R.J., "Investigation fo the shock-tube boundary layer by a tracer method." *Physics of Fluids*, Vol. 6, 1-9, 1963.
12. Edmunds, H., "An Investigation of Leading Edge Vortex Flow Using Hydrogen Bubble PIV and Other Flow Visualisation Methods", Masters Thesis, University of Washington Department of Aeronautics and Astronautics, 2000.
13. Srigrarom, S., "On the Formation of Vortex Breakdown over Delta Wings", PhD Dissertation, University of Washington Department of Aeronautics and Astronautics, 2001.
14. PixelFlow™ 2.1, *Installation and User's Guide*, General Pixels, 2001.
15. Shih, C. and Ding, Z., "Unsteady Structure of Leading-Edge Vortex Flow Over a Delta Wing", AIAA 96-0664.
16. Werlé, H., "On Vortex Bursting", Chief of Research Group at Onera, NASA TM-77587, N85-10008, June 1984.
17. Westerweel, J., Dabiri, D., and Gharib, M., "The effect of a discrete window offset on the accuracy of cross-correlation analysis of digital PIV recordings", *Experiments in Fluids*. Vol. 23, 1997.

18. Towfighi, J., Rockwell, D., "Instantaneous Structure of Vortex Breakdown on a Delta Wing via Particle Image Velocimetry", *AIAA Journal*. Vol.31, No.6, 1992.
19. Mitchell, A. et al. "Characterization of Vortex Breakdown by Flow Field and Surface Measurements", AIAA 2000-0788.
20. Visser, K.D., and Nelson, R.C., "Measurements of Circulation and Vorticity in the Leading-Edge Vortex of a Delta Wing", *AIAA Journal*, Vol. 31, pp. 104-112, January 1993.
21. Moreira, J., and Johari, H., "Direct Measurement of Delta Wing Vortex Circulation Using Ultrasound", AIAA 97-0743.
22. Huang, X.Z. et al., "Circulation Criterion to Predict Leading-Edge Vortex Breakdown Over Delta Wings", AIAA 97-2265.
23. Sarpkaya, T., "On stationary and travelling vortex breakdowns", *Journal of Fluid Mechanics*, Vol. 45, part 3, pp. 545-559, 1971.
24. Nakamura, Y., Leonard, A., and Spalart, P.R., "Numerical Simulation of Vortex Breakdown by the Vortex-Filament Method." NASA Ames Research Center, Moffett Field, CA.
25. Payne, F.M., Ng, T.T., and Nelson, R.C., "Visualization and Wake Surveys of Vortical Flow over a Delta Wing", *AIAA Journal*. Vol. 26, No. 2, February 1998.
26. Visbal, M.R., "Computational and Physical Aspects of Vortex Breakdown on Delta Wings", AIAA 95-0585. 33<sup>rd</sup> Aerospace Sciences Meeting and Exhibit, 1995.
27. Bertin, John J., and Smith, M.L., *Aerodynamics for Engineers*, Chap 7, Prentice Hall, New Jersey, 1998.
28. Gordnier, R.E., and Visbal, M.R., "Unsteady Vortex Structure over a Delta Wing", *Journal of Aircraft*, Vol. 31, No. 1, pp. 243-248, 1994.
29. Shah, G.H., "Wind-Tunnel Investigation of Aerodynamic and Tail Buffet Characteristics of Leading-Edge Extension Modifications to the F/A-18", AIAA 91-2889, August 1991.
30. Thompson, D. H., "Water Tunnel Flow Visualisation of Vortex Breakdown over the F/A-18", ADA 236026.
31. Sheta, E. and Harrand, V., "Active Vortical Flow Control For Alleviation of Twin-Tail Buffet of Generic Fighter Aircraft", AIAA 2000-0906, January 2000.
32. Moeller E.B., Rediniotis, O.K., "Hingeless Flow Control Over a Delta Wing Planform", AIAA 2000-0117.
33. Guy, Yair, Morrow, Julie A., and McLaughlin, Thomas E., "Control of vortex breakdown on a delta wing by periodic blowing and suction", AIAA 99-0132, AIAA Aerospace Sciences Meeting and Exhibit, 37th, Reno, NV, Jan. 11-14, 1999.

34. Husain, Hyder, Shtern, V., Hussain, F., "Control of Vortex Breakdown Using Vortex Generators", AIAA 97-1879, AIAA, Shear Flow Control Conference, 4th, Snowmass Village, CO, June 29-July 2, 1997.
35. Srigrarom, S., and Kurosaka M., "Shaping of Delta-Wing Planform to Suppress Vortex Breakdown", *AIAA Journal*, Vol. 20, No. 1, January 2000.
36. Leonard, A., "Computing Three-Dimensional Incompressible Flows with Vortex Elements." *Ann. Rev Fluid Mechanics*, Vol.17, pp. 523:59, 1985.
37. Saghbini, J.C., and Ghoniem, A.F., "Numerical Simulation of the Dynamics and Mixing in a Swirling Flow", AIAA 97-0507, 35<sup>th</sup> Aerospace Sciences Meeting and Exhibit, 1997.
38. Visbal, M.R., "Computed Unsteady Structure of Spiral Vortex Breakdown on Delta Wings." AIAA 96-2074.
39. Jumper, E.J., Nelson, R.C., and Cheung, K., "A Simple Criterion for Vortex Breakdown", AIAA 93-0866.
40. Levinski, Oleg., "Review of Vortex Methods for Simulation of Vortex Breakdown", Defence Science and Technology Organisation, September 2001.
41. Gessner, Fred. *Private communication*. Professor, Department of Mechanical Engineering, Univ. of Washington, June 2002.



## Appendix A – University of Washington Water Tunnel

### A.1 Water Tunnel Description

A horizontal recirculating water tunnel with a 3.0m x 0.7m x 0.7m glass test section located at the University of Washington Fluid Dynamics Laboratory was used for the experiments in this thesis. A 30 horsepower electric motor, controlled through a variable frequency drive, drives a centrifugal pump for variable freestream flow speeds of 0 to 50cm/s. Several modifications to the tunnel were made over the course of this study. These include a new power supply unit so that the tunnel speed can be digitally controlled, an out-of-line filtration system for dye and particle removal, and top covers to protect the water from light and prevent algae growth. The main diffuser pipe was also redesigned to allow for better diffusion of the water and a better top seal to prevent water from splashing over the sides of the tunnel during high-speed operation. A layout of the tunnel is seen in Figure A-1.

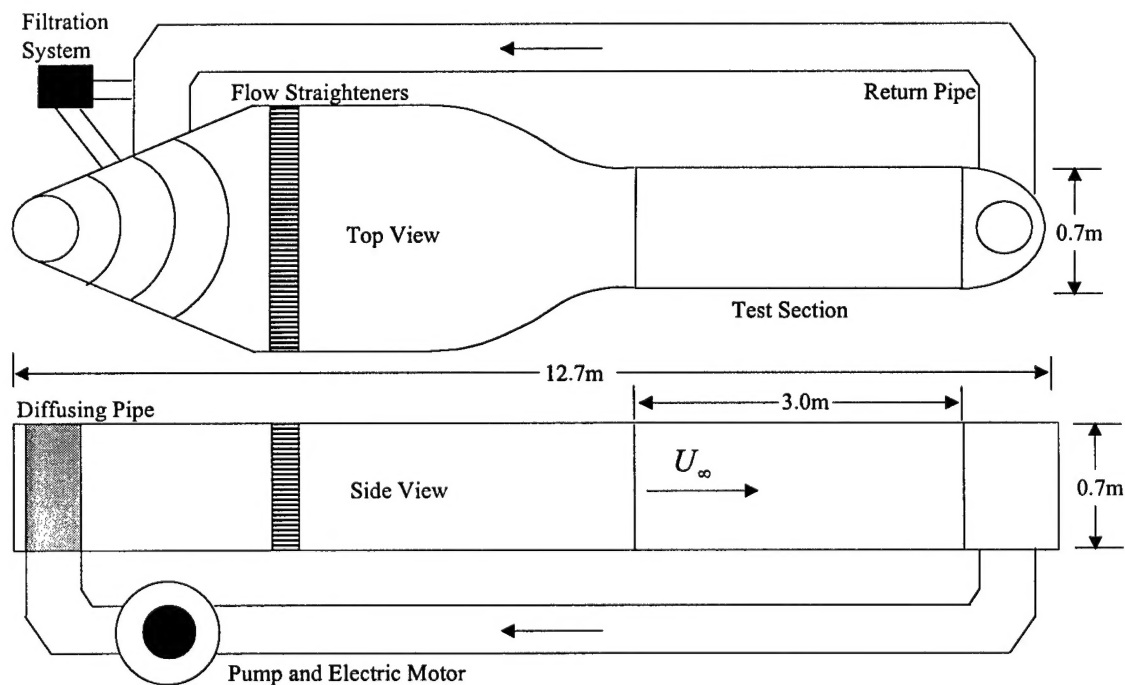


Figure A-1: Water Tunnel Layout

## A.2 Turbulence Level Determination

Hot film tests to determine the turbulence level of the water tunnel were performed in August of 2002. A Dantec constant temperature anemometer (CTA) bridge was used in conjunction with a TSI 1210-20W water probe. The probe was placed in the center of the test section and aligned perpendicular to the flow. Freestream flow speed was varied from 2 to 17 cm/s and the turbulence level was measured at each speed. Although the water tunnel is capable of approximately 50cm/s, tests were not conducted at higher speeds for fear of breaking the film. According to the Dantec manual, the output voltage from the bridge,  $E$ , will vary with  $U$ , the local velocity as is given by King's law:

$$E^2 = (A + BU^n)a \quad (\text{A-1})$$

where  $a$  is the overheat ratio, and  $A$ ,  $B$  and  $n$  are experimentally arrived at and are found when calibrating the probe. The Dantec manual recommends  $n = .45$  for their bridge and setup. If the aim is only to quantify the turbulence level of the tunnel, it is not required to find  $A$  and  $B$ , and the turbulence level may be found as follows (*ref. 41*). For  $U = 0$ ,

$$E^2 = Aa = E_0^2. \quad (\text{A-2})$$

Substituting into Eqn. (A-1) gives:

$$E^2 - E_0^2 = aBU^n. \quad (\text{A-3})$$

Differentiating both sides gives:

$$2EdE = naBU \frac{dU}{U} \Rightarrow \frac{dU}{U} = \frac{2EdE}{n(E^2 - E_0^2)}. \quad (\text{A-4})$$

Assuming  $E = \langle E \rangle + e'$  and  $U = \langle U \rangle + u'$ , let  $dE = e'$  and  $dU = u'$  and take the root mean square of both sides of the equation to give an expression for the turbulence level

$$T = \frac{\sqrt{u'}}{\langle U \rangle} = \frac{2E\sqrt{e'}}{n(E^2 - E_0^2)} \quad (\text{A-5})$$

where  $\sqrt{e'}$  is the root mean square (rms) value of the bridge voltage signal when the test is conducted at one freestream velocity. The mean output voltage was measured on a Fluke 8842A multimeter set on the DC setting, while the rms value of the signal was obtained by switching to the AC setting. The overheat ratio,  $a$ , was set following the procedure in the manual. It is important to set the overheat ratio to achieve the

recommended operating temperature of the probe (67°C for the above mentioned probe). If the probe is run too hot, air bubbles will form around the film and make voltage readings meaningless. Before taking measurements, the probe was inspected to make sure it was free of any bubbles. In order to get a better approximation for  $E_0^2$ , Professor Gessner of the UW Dept of Mechanical Engineering suggests to use the intercept of the best fit line at  $U = 0$  when  $E^2$  is plotted versus  $U^n$  in order to negate effects of heat transfer due to free convection into the water. Figure A-2 shows the data and best fit line from the test run.

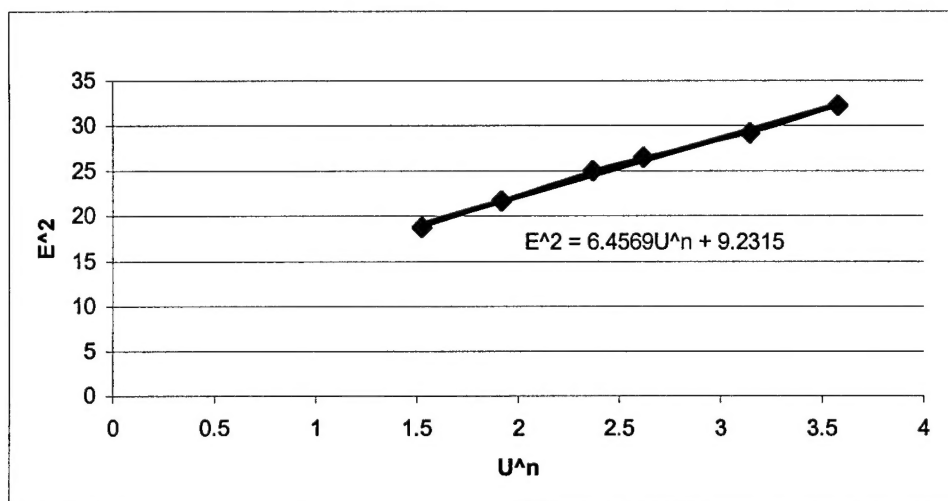


Figure A-2: Best fit line to determine  $E_0$

The value of 9.23 was used for  $E_0^2$  and the rms outputs for each speed were put into Eqn. (A-5) to obtain a graph of the freestream turbulence level of the tunnel.

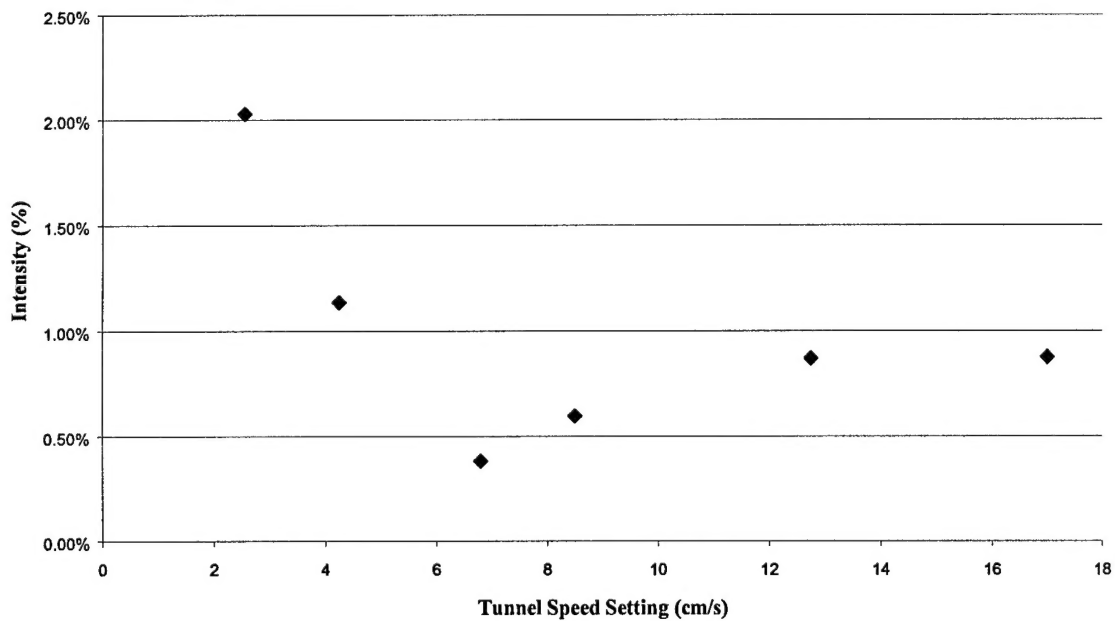


Figure A-3: Turbulence intensity measurements of UW water tunnel

The turbulence level of the tunnel is significantly higher for speeds slower than about 5cm/s. This is probably due to instabilities and vibrations associated with the pump. However, for speeds above 5cm/s, the freestream turbulence level is always below 1%, which is very desirable. This suggests that if a low turbulence level is desired, tunnel speeds should be kept above 5cm/s, as was done in the DPIV measurements and dye visualizations in this thesis.